A coupled hydrodynamic and discrete element method for modelling flash flood debris

Samantha Helen Mahaffey
School of Engineering
Newcastle University

A thesis presented for the degree of
Doctor of Philosophy
May 2018

Abstract

Floating debris transported during flash flooding damages structures, blocks bridges and alters channel hydraulics. In recent years, a number of high profile flash flood events have exhibited these processes. Recreating flood events through hydrodynamic modelling is an essential means by which engineers understand flood risk. However, there exists relatively little research focused on floating debris as a flash flood process and until now there have been limited attempts to incorporate floating debris processes into hydrodynamic flood modelling.

In this work, a new coupled floating debris modelling tool is developed for 1D and 2D applications. The new tool combines a finite volume Godunov-type hydrodynamic scheme that solves the governing shallow water equations with the discrete element method for solving object contact and motion. A balanced force coupling procedure is used to calculate the hydraulic forces acting on floating objects and the corresponding shear stress imparted to fluid cells. Hydrodynamic and hydrostatic force components are derived from the fluid momentum principle and overcome problems associated with an empirically derived drag force used elsewhere. Balanced force coupling enables the new tool to predict both the transport dynamics of floating objects and their resulting backwater effects. Debris dimensions are approximated using the multi-sphere method for shape representation. This ensures collisions are realistically modelled and application is not restricted by debris shape and size. The new modelling tool is extensively validated for dam break experimental test cases performed in a hydraulic flume. Predicted values for water depth and floating object position compare well with their observed counterparts for both 1D and 2D validation cases.

Additionally, the coupled numerical modelling approach is applied to investigate flash flooding, including floating debris impacts in Boscastle, 2004. The Boscastle event was significant as 116 vehicles were washed downstream, some of which blocked bridges, altering flood hydraulics. Model predictions of water depth, depth averaged velocity and Froude number demonstrate the localised effects of two debris blockages during the flood. Predicted water levels compare well to evidence of maximum depths collected after the event. Application of the new debris modelling tool to investigate the transport of flooded vehicles predicts vehicle transport pathways consistently with eye witness and post event observations. Application of the floating debris modelling tool to the Boscastle event demonstrates that the new tool can perform well for real world applications. However,

high computational costs require further model development to accelerate the long simulation process.

This work demonstrates that a combined finite volume, discrete element approach to hydrodynamic modelling provides a greater understanding of flood hazard than pure-water hydrodynamic modelling alone. Model outputs are valuable for quantifying flood risk, assessing flood damage and planning remediation measures. Furthermore, the new tool will enable a multitude of future applications and improve understanding of floating debris processes. Though the coupled approach has here been applied to flash flooding, the modelling methodology is applicable to a number of other natural hazards. Object transport by tsunami inundation, storm surge and river ice may all be simulated using the modelling methodology presented in this work.

Acknowledgements

I would like to thank my main supervisor, Professor Qiuhua Liang, for his advice and guidance throughout this project, and for lending his extensive expertise in computational hydraulics. I am also extremely grateful to Dr Elizabeth Lewis, for providing informal supervision and for proofreading my thesis with only a moment's notice.

I would like to thank my secondary supervisors: Dr Andy Large, Dr Geoff Parkin and Dr Mo Rouainia for their continued enthusiasm, and for sharing their knowledge of floating debris processes and the discrete element method during the initial stages of this research.

I would like to thank and acknowledge Dr Xilin Xia, who has provided and advised on the 2D hydrodynamic scheme used in Chapter 5. I would also like to thank Professor Roger Falconer and Dr Davor Kvocka at Cardiff University for kindly sharing the Boscastle data sets used in Chapter 6.

I am grateful to Dr Luke Smith for sharing his superior understanding of C++ programming and particularly for explaining pointers. In addition, to Kate Mahaffey whose mathematical expertise has been of ceaseless value and is evident throughout this thesis. Furthermore to Dr Jingchun Wang and Dr Reza Amouzgar for their support and advice on hydrodynamic modelling.

Experimental studies, presented in Chapter 4 and 5 were performed at the hydraulic research facility at Hohai Universtiy, China. Thanks are due to colleagues at Hohai University, particularly Dr Gang Wang, Yan Xiong and Kaicui Chen for assisting with these flume experiments.

This project has been funded by the Natural Environment Research Council (NERC) and falls within the Susceptibility of Catchments to Intense Rainfall and Flooding (SINATRA) consortium project. I would also like to thank Professor Hayley Fowler for providing an additional 6 months of funding through the SINATRA project budget.

To my friends and colleagues who always provide a much-needed distraction from research, especially Mhari Barnes and Elizabeth Lewis, I am extremely grateful. Finally, to Mum and Chris.

Contents

List of Figures

List of Tables

Chapter 1

Introduction and research approach

1.1 Introduction and rationale

Flooding is one of the most significant natural hazards facing the UK. According to the UK government committee on climate change, flooding poses the greatest of all climate related risks to communities, infrastructure and businesses, both now and into the future (CCC, 2017). Though slow-rate-of-rise flooding is costly and often devastating when property and businesses are damaged, in Europe these events are rarely associated with fatalities (Gaume et al., 2009). Flash flooding, however, often results in loss of life (Gaume et al., 2009). Most notably in the UK, the 1952 flash flooding of Lynmouth resulted in 34 fatalities (Dobbie and Wolf, 1953; Gaume et al., 2009) and more recently in 2017, flash flooding around Athens, Greece caused 21 deaths and dozens more injuries.

Flash floods are caused by specific meteorological, topographical and hydrological conditions that, when combined, lead to rapid runoff production processes (Marchi et al., 2010). Unlike winter flooding that results from prolonged rainfall, flash flooding arises from localised high intensity rainfall and is generally observed during summer downpours. Catchment hydrology and antecedent conditions, such as already saturated soil, contribute to high rainfall-runoff conversion. Where events occur in steep-sided basins the resulting hydrograph propagates rapidly downstream with little attenuation. As a result, short warning times make early warning systems difficult to establish and afford those at risk little time to prepare.

The resulting flash floods are characterised by high velocity 'walls of water' that rapidly cascade downstream causing costly damages directly to buildings, infrastructure and property (Dutta et al., 2003). Preservation of the hydrograph peak leads to transcritical features and supercritical flow regimes that are hydraulically complex and notoriously destructive in nature (Kvočka et al., 2015). When rapid flow regimes interact with down-

stream urbanised conurbations, flows around structures produce standing waves and foundation scour that undermines structural integrity. Furthermore high velocity out of bank flow has the capacity to transport a cargo of floating debris including tree trunks, vehicles and household waste. While vehicles, up-rooted trees and other inanimate objects are innocuous during low flows, when transported during extreme flood events these debris have potentially hazardous consequences. Where transported objects become trapped at bridges and other hydraulic obstacles, temporary dams form that alter flow paths and damage structures. The subsequent collapse of these temporary dams cause sudden shock-waves to propagate downstream.

The effects of flash flooding and associated debris transport were clearly demonstrated during 2004 flooding of Boscastle on the north Cornish coast. Over 200mm of rainfall fell within 5 hours onto an already saturated, steep sided catchment. The resulting flood, estimated as a 1 in 400 year probability event, decimated the small town. The high velocity stream power up-rooted trees and bushes (Figure 1.1a), which became trapped downstream during the initial stages of the event and caused the river to divert out of bank and through the town (Fenn et al., 2005). Flow diversion through a local car park added a total of 116 vehicles to the river's debris load, which either became lodged at downstream bridges (Figure 1.1b) or washed out to sea. Two road bridges were almost entirely blocked by vehicles and debris and a number of additional debris jams were reported to have formed further upstream. Blockages resulted in substantial hydraulic and morphological changes. These included channel avulsions and localised subcritical and supercritical flow regimes that produced sediment deposition and caused scour. Post-event investigations indicate that the rapid blockage of the main road bridge caused a sudden increase in upstream water level and significant redistribution of flow into the nearby streets (Environment Agency, 2004; HR Wallingford, 2005). The Boscastle event has since gained notoriety in fluvial hydraulics for characterising flash flood processes, particularly debris transport.

More recent flash flooding in Alyth, Scotland on 17th July 2015 saw the mobilisation of a large quantity of floating debris that exacerbated flood severity. Peak flows estimated at $40m^3/s$ occured rapidly within the small, steep catchment (Perth and Kinross Council et al., 2015) and transported of a wide range of floating objects (Figure 1.2) that became trapped at bridges crossing Alyth burn. A total of four footbridges collapsed. Post event studies concluded that local debris blockages and subsequent blockage failures were the likely cause of changes to localised flow patterns, including by generating two reported 'flood waves' (Perth and Kinross Council et al., 2015). The topography and hydrology that typified both the Boscastle and Alyth events are characteristic of numerous UK

(a) Debris accumulation at bridge site

(b) Vehicles transported by flooding

Figure 1.1: Flooding in Boscastle 2004

(a) Debris accumulation

(b) Vehicles transported by flooding

Figure 1.2: Flooding in Alyth, Scotland 2015

catchments that share vulnerability to flash flooding (Archer and Fowler, 2015).

Despite its prevalence within flash flood related hazard, the processes surrounding debris transport remain largely unstudied. This is in part due to difficulty in capturing event data; as events generally occur in small, un-gauged catchments, with very short lag times, usually $< 6hrs$ (Marchi et al., 2010). An event will likely be over by the time interested parties have reached the catchment and set up equipment. Likewise, predicting the impacts of flash flooding through numerical modelling is difficult and requires advanced shock-capturing capabilities to predict the complex flow regimes that arise. The application of shock capturing hydrodynamic modelling has thus far been limited by its high computational cost. Trade-offs between computational accuracy and simulation time often result in practitioners favouring modelling schemes that achieve shorter run-time by simplifying physical properties (Kvočka et al., 2015). However, recent advances in computational capability have enabled a new generation of hydrodynamic modelling tools that

accelerates computation through parallel processing across multiple graphics processing units (GPUs) (Amouzgar et al., 2014; Liang et al., 2016). Such tools retain the accuracy of high domain resolution, small time intervals and shock capturing capabilities but with vastly accelerated run-times (Smith et al., 2014).

Despite these advances, attempts to numerically model the hydraulic effects of debris blockages remain hampered by a lack of software capability. Conventional numerical modelling schemes rarely account for the presence of debris blockage within the domain topography and no commercially available, physically based modelling software exists that intrinsically incorporates debris transport into its calculation cycle. Difficulties in developing such a tool are amplified by a lack of suitable physical data for software validation.

Research in this area is, however, emerging. Of the debris modelling approaches that have been trialed, those that employ the discrete element method are growing in popularity. First proposed by Cundall and Strack (1979), the discrete element method was initially developed for geotechnical applications and is a physically based approach to predicting the motion of objects in collision. Recent efforts to couple the discrete element method with computational hydraulics have shown promising results despite their infancy (Ren et al., 2014; Stockstill et al., 2009). With further research and development, this coupled modelling approach could provide a commonplace tool within computational flash-flood hydraulics.

1.2 Research problem

As far back as the infamous flooding of Lynmouth, 1952, debris has been recorded as having influenced and exacerbated flash flood impacts, yet research into the mechanisms by which debris interacts with flash flooding is limited (Rigby et al., 2002; Xia et al., 2011). Furthermore, attempts to numerically model floating debris transport have only recently gained momentum. There are a number of factors that may pose barriers to this area of research:

- **Data acquisition in difficult.** 'Flashy' catchments are often un-gauged requiring data to be captured in real time or through post event surveys. Due to the remote and disparate locations of at-risk catchments, events will likely occur far away from research centres. Rapid occurrence and short warning times rarely afford responders the necessary time to reach effected areas.

- **Debris is diverse and difficult to quantify.** Objects transported by floodwaters

range from small twigs, to whole vehicles, quantifying how much debris has been transported is therefore difficult.

- **Flash flooding is difficult to predict through numerical modelling.** High velocity, trans-critical flows require complex shock capturing schemes to adequately predict flow transitions and conserve momentum. These, conventionally require high computational time and resource availability (Kvočka et al., 2015).

- **Software does not account for floating debris.** Conventional modelling approaches do not automatically consider floating debris and no specialised floating debris modelling tool is currently commercially available.

1.3 Aims and objectives

1.3.1 Aim

The aims of this research is to develop a coupled floating debris modelling tool to investigate the transport dynamics of floating debris during UK flash flooding. The tool should build upon an existing finite-volume hydrodynamic modelling structure developed at Newcastle University (Liang, 2010) by introducing a debris transport module based on the discrete element method. The tool should predict the motion, interaction and impact of a variety of floating objects and also reproduce the hydraulic consequences of a debris blockage. The new modelling tool should achieve accurate and practical results that are valuable to civil engineering applications. This research aim is accomplished by achieving the following objectives:

1.3.2 Objectives

- Perform dam break flume experiments that feature scaled woody debris to improve understanding of the physics governing debris transport and also to provide experimental test cases for numerical model validation.

- Develop a floating debris code module in C++ that is based on the discrete element method and is suitable for coupling with existing hydrodynamic modelling platforms.

- Validate the floating debris code module against analytical solutions to simple theoretical test cases.

- Couple the floating debris code module with a 1D hydrodynamic modelling tool through a physically based force coupling procedure.
- Validate the new coupled 1D debris modelling tool using analytical and experimental test cases
- Couple the floating debris code module with a 2D hydrodynamic modelling scheme and improve functionality for 2D applications
- Validate the new 2D debris modelling tool using experimental test cases.
- Apply the new 2D debris modelling tool to investigate the transport dynamics of flooded vehicles during flash flooding of Boscastle in 2004.

1.4 Research approach

The aims and objectives of this research will be achieved though a combination of numerical, analytical and experimental modelling. The research approach is outlined here.

1.4.1 Model development

A new numerical modelling tool is developed in this work to predict the transport and interaction of a range of floating debris entrained in flood water. The modelling software is developed using two distinct numerical methods. A 2D hydrodynamic scheme is applied to solve the governing hydraulic equations and the discrete element method solves the motion equations of floating objects.

Hydrodynamic modelling tools that solve the 2D shallow water equations have been successfully applied to predict water depth and detailed velocity fields of flooding from a variety of sources (Liang et al., 2008; Liang and Smith, 2015; Simons et al., 2014; Wu et al., 2013). Of these schemes, those that employ shock-capturing capabilities are able to predict complex, transcritical flow regimes associated with flash flooding (Liang et al., 2016). This work builds upon a finite volume shock-capturing hydrodynamic scheme developed at Newcastle University (Liang, 2010). The numerical scheme has already been extensively validated for flash flood-like applications (Liang et al., 2016), and therefore provides an ideal platform with which to couple a floating debris transport module. Details of the hydrodynamic scheme are provided in Chapter 3.

The discrete element method (DEM) solves the contact forces and motion of objects in collision. Some preliminary studies (Piche et al., 2014; Robb et al., 2016; Stockstill et al.,

2009), which have coupled the discrete element method with hydrodynamic schemes, indicate that DEM is suitable for simulating the dynamics and transport of floating objects. In this work a discrete element scheme is developed specifically for coupling with the hydrodynamic scheme discussed previously. The DEM replicates objects of a range of shapes and sizes and predicts the realistic force-displacements arising from their collision. The DEM developed here is also computationally compatible with the hydrodynamic scheme presented by Liang (2010). Details of the discrete element scheme are provided in Chapter 3. The DEM is then coupled with 1D and 2D hydrodynamic solvers using a force coupling procedure that maintains consistency with Newtonian laws of motion and hydrodynamic assumptions. The 1D and 2D force coupling procedures are explained in detail in Chapters 4 and 5.

1.4.2 Physical modelling

The physics governing floating debris transport are investigated through physical modelling in a hydraulic flume. Experiments are performed at the Chinese Government hydraulic research facility based at Hohai University, China. Dam break conditions, which can be considered hydraulically similar to flash flood inundations (Albano et al., 2016) are recreated using a lifting gate system. A range of wet bed and dry bed initial conditions are tested and water levels are measured at four gauge points. An assortment of short wooden dowels are introduced to the flume downstream of the lifting gate and their position is visually tracked throughout experimentation.

Initially, singular dowels are transported approximately unidirectionally by the dam break wave. These test cases can be considered as approximately 1D as minimal reflective flows occur and the transported object remains roughly longitudinal in orientation. These test cases enable validation of the 1D coupled debris modelling tool developed in this work.

Further experiments are performed where a scaled bridge pier is introduced to the downstream region of the flume. The fixed bridge obstacle generates reflective and diffractive waves, therefore flow conditions are considered 2D. Multiple wooden dowels are introduced to the flume and transported by the dam break wave. These experimental results provide validation data for the new 2D debris modelling tool developed in this work.

1.4.3 Analytical modelling

The numerical methods employed in the work are verified through analytical modelling. Exact, analytical solutions to the governing equations are derived for idealised test cases and their results compared to numerical predictions.

1.4.4 Numerical modelling

Numerical modelling of analytical and experimental test cases is performed to enable validation of the new floating debris modelling tool developed in this work. Analytical validation demonstrates that the applied numerical methods are able to solve the governing equations to an acceptable level of accuracy. Experimental validation demonstrates that the floating debris modelling tool can accurately simulate physical processes for controlled experimental applications. Once validated, the new 2D debris modelling tool is applied to simulate debris transport during flash flooding of Boscastle, 2004. Results are compared to eye witness and post event data. Application to flooding in Boscastle demonstrates that the new 2D debris modelling tool is suitable for real world flash flood applications.

1.5 Scope

Floating debris is here defined as any object mobilised and transported at the water's surface. This work does not include bed load transport and subsequent morphological changes as this has already been covered in detail elsewhere (Guan and Liang, 2017). Although floating debris ranges is shape, size and composition, this work focuses on large floating objects observed as having significant hydraulic impact during historic flood events such as Boscastle (HR Wallingford, 2005) and Lynmouth (Dobbie and Wolf, 1953). In this work, these are confined to large woody debris (LWD) and mobilised vehicles. However, the modelling tool is developed so that it can be applied to objects of any size and shape in the future.

This work does not cover debris flows (also referred to as debris slides, debris torrents and debris floods), where transported objects are suspended throughout the vertical water profile and form a 'carpet' over the water's surface. Debris flows are not a significant risk in the UK and are also covered in detail elsewhere (Bocchiola et al., 2002; Iverson, 1997).

The new floating debris modelling tool developed in this work is intended to demonstrate the potential of a DEM-coupled hydrodynamic modelling approach for floating debris applications. This work is not intended to provide a fully developed software tool with corresponding graphical interface for commercial uptake. Such a software tool would require extensive further development and analysis and is reccomended as future work outside of this study scope.

1.6 Structure of thesis

Chapter 1. Introduction

This chapter introduces the research project.

Chapter 2: Literature review

This chapter provides an overview of up-to-date knowledge of floating debris as a flash flood process. This includes a summary of debris characteristics, transport processes during flooding, its implications on hydraulic structures and the consequences for hydraulic modelling. A review of previous physical and numerical modelling studies is provided and the methods applied by these studies are critiqued. The implications of previous research to this work are discussed in detail. Finally a set of modelling criteria are formulated, based on the literature findings, that the floating debris modelling tool developed here aims to achieve.

Chapter 3: Numerical methods

This chapter presents the numerical methods employed by the hydrodynamic and a discrete element modelling approaches used in this work. First the governing theory and numerical schemes used by the hydrodynamic method are described along with justification for its application to flash flood hydraulics. The discrete element scheme developed in this work is presented along with background theory and governing equations. The numerical method and calculation cycle are explained in detail. The numerical modelling scheme is then validated against analytical solutions for three idealised test cases, demonstrating that the tool developed here successfully solves the governing equations to an acceptable degree of accuracy.

Chapter 4: Modelling floating debris transport in 1D

This chapter presents a 1D floating debris modelling tool that couples the discrete element method with a 1D hydrodynamic scheme. A theoretical overview to the coupling procedure is presented followed by a description of the numerical coupling method. An analytical solution to the equations governing object transport is derived, and results are compared against numerical predictions. The 1D tool is further validated against experimental results. The experimental set-up and procedure is presented for five test cases where a single object is transported in approximately unidirectional flow. Results for

water depth at four gauge points, and object horizontal position with respect to time are compared to numerical predictions. The results are visually and statistically validated.

Chapter 5: 2D Modelling of floating debris at obstacles

This chapter presents a 2D floating debris modelling tool that couples the discrete element method with a 2D GPU-accelerated hydrodynamic scheme. The numerical method and calculation cycle is presented for the force coupling procedure. Experimental results generated through hydraulic flume experiments are presented where a variety of wooden dowels are transported by a dam break wave in the presence of a single, fixed obstacle. A comparison between observed and numerically predicted values for water depth at four gauge points are presented and statistically validated. The location of floating wooden dowels at different time intervals are compared against photographic evidence. Both wet and dry bed initial conditions are tested. Further model validation is presented as the 2D coupled tool is applied to simulate an experimental study performed by Albano et al. (2016). Here three mobile objects are transported by a dam break wave in the presence of two fixed domain obstacles. Model predictions of water depth at two gauge points and horizontal object positions are compared against observed values and statistically validated. Visual validation is performed by comparing model outputs against photographic evidence.

Chapter 6: Investigating debris processes during flooding in Boscastle, 2004

An investigation into flash flooding and floating debris transport during the Boscastle, 2004 event is presented in this chapter. Simulated results for flash flood extent and water depth are presented and compared against evidence collected through post event investigations. Vehicles transported from a riverside car park are modelled using the new floating debris modelling tool. Numerical predictions for vehicle transport are compared against observational information.

Chapter 7: Conclusions and recommendations

Conclusions from the current research are established and discussed in a wider engineering context. Suggestions are made for possible future work.

1.7 Planned publications

In light of the research presented in this work, three papers are currently under preparation. The papers are listed below and will be submitted for publication in spring 2018.

- **Numerical modelling of floating debris transport in 1D** - Presents the results of 1D numerical and experimental studies included in Chapter 4 of this work.
- **Numerical modelling of floating debris transport processes in 2D** - Presents the results of 2D numerical and experimental studies included in Chapter 5 of this work.
- **Modelling floating debris during flooding in Boscastle 2004** - Presents the results of hydrodynamic and floating debris modelling of flash flooding in Boscastle 2004. These results are included in Chapter 6 of this work.

Chapter 2

Literature review

In light of high profile flood events, such as Boscastle in 2004, it is evident that floating debris can be influential to flash flood hydraulics. Furthermore, as debris blockages have become more prevalent in recent years (Rigby et al., 2002; Xia et al., 2016, 2011) there is growing incentive to better understand its behaviour and flood consequences. For modellers, floating debris poses a significant challenge; models that do not incorporate debris blockages negate a major process affecting channel hydraulics and are therefore likely to generate misleading results. The existing approaches to researching floating debris may be divided broadly into three categories: laboratory experiments, field studies and numerical modelling. This chapter examines the existing research by first summarising these three approaches. A characteristic overview of the types of flood borne debris found in UK rivers is provided. The physical processes associated with debris transport during flash flooding are discussed. The impacts of debris blockage on channel hydraulics and river structures are described, with reference to current UK design guidelines. Following on from this, approaches to accounting for the effects of debris within existing modelling packages are described and an alternative, emerging approach is presented for further investigation in this study. Based on the findings of this chapter, a set of modelling criteria are suggested that a practical floating debris modelling tool for flash flood application should reasonably satisfy.

2.1 An overview of floating debris research

Debris is ubiquitous in UK rivers. As an example, Figure (2.1) demonstrates the variety and abundance of objects deposited in a short stretch of the River Ouseburn, Newcastle upon Tyne within a single afternoon. Although the exact origins of these objects are unknown, it is likely that many of them entered the channel upstream, through flooding

or fly-tipping and were transported to their current location under high flow conditions. In their current state, the objects depicted in Figure (2.1) are innocuous. However when objects such as these become trapped at hydraulic structures, the resulting flood conditions can cause significant damage to property, infrastructure and human-life (Xia et al., 2016).

However, there is limited research into the processes that surround floating debris during flash flooding (Comiti et al., 2016). Of the existing research, investigations tend to be based on inspection of field records from previous floods (Diehl, 1997; Rigby et al., 2002), laboratory investigations (Bocchiola et al., 2008, 2006; Braudrick and Grant, 2000, 2001; Xia et al., 2016) or a combination of the two (Lyn et al., 2003). There exists a very small body of work that employ numerical modelling as their research approach (Albano et al., 2016; Ruiz-Villanueva and al., 2014*c*). Furthermore, studies into floating debris dynamics tend to focus specifically on large woody debris in rivers (Abbe and Montgomery, 1996; Braudrick et al., 1997; Comiti et al., 2016) or focus on washed away vehicles in urban areas (Shu et al., 2011; Xia et al., 2011) and therefore rarely consider all classifications of object within a single study.

Experimental investigations

There have been many experimental studies into the transport dynamics of floating objects within a hydraulic flume. Braudrick and Grant (2000, 2001) performed a series of flume experiments to examine the incipient motion and entrainment of large woody debris transported by flow over a rough bed. Shu et al. (2011) obtained water depth and velocity thresholds for vehicle instability in flood waters through flume experiments using die cast model vehicles. Xia et al. (2011) derived a flow variable-dependent formula for the incipient velocity of vehicles in flood waters based on experimental findings. Bocchiola et al. (2006) and Bocchiola et al. (2008) investigated log jam formation through flume experiments where the transport of floating wooden dowels was obstructed by vertical wooden rods. Similarly Albano et al. (2016) investigated the transport of solid parrallelipeds in the presence of fixed obstacles under a dam break flume configuration. Goseberg et al. (2016) performed experiments in a tsunami wave basin, investigating the displacement of floating rectangular debris. Xia et al. (2016) investigated the hydraulic impacts of vehicle blockage at bridges using scale models within a hydraulic flume. Lyn et al. (2003) tested the impact of wooden dowel accumulation on a number of obstacles including a bridge pier, sand bar and channel groynes acting as debris accumulation counter measure.

Experimental studies such as these provide a controlled environment from which to derive generalised conclusions regarding debris transport. For example incipient motion

thresholds, transport dynamics and blockage probability. However, such studies are less convenient for investigating actual flood events in a specific catchment with corresponding topographical and hydrological characteristics. Though such studies are possible, they require the construction of bespoke physical models usually at state of the art research facilities, thus demanding high financial and time related costs. Numerical modelling tools that can be applied to investgate flooding at a range of scales overcome many of these experimental limitations. However without improved model capability, this is not yet an available choice for floating debris applications.

Field data investigations

Since a pioneering study by MacVicar et al. (2009), who conducted in-situ field investigations into wood transport, further on-site field investigations have focused on monitoring debris transport in rivers through GPS and other tracking techniques (Ravazzolo et al., 2015). Nevertheless, in the UK most available information on floating debris transport and particularly blockage has been sought through field records of previous flood events (Rigby et al., 2002). Wallerstein et al. (2013) performed a comprehensive study by quantifying and characterising debris caught at trash screens across Belfast. The inspection records of 140 trash screens were assessed over a period between 2002 and 2008. Though record-based studies of this scale are feasible for densely populated urban areas like as Belfast, such detailed records are much less likely to exist for the type of small, secluded catchments that are vulnerable to flash flooding. Field monitoring at these sites is possible, however within academic studies is inconvenient as an extreme rainfall event may not occur within the funded monitoring period. Community based monitoring schemes provide a possible solution as funding and continued monitoring are secured for substantial timescales. For example the Haltwhistle burn community monitoring scheme, led by Tyne Rivers Trust (2015) has demonstrated the value and validity of community captured data sets during local flash flood events (Starkey et al., 2017). Similar schemes are increasing in popularity however cannot be expected to provide detailed information throughout a catchment, particularly during high flows.

Numerical flood modelling tools are able to predict detailed depth and velocity field data at any point within an effected catchment. This information is valuable to engineers assessing flood hazard, risk and damage after an event. Such information would be not only difficult, but extremely dangerous to collect through field investigation. A numerical modelling tool that is able to predict detailed debris transport processes would, therefore, provide safe and practical means of generating data.

Numerical modelling investigations

There are very few investigations into floating debris that apply numerical modelling techniques. This is largely due to a lack of software capability within flood modelling packages. A number of probabilistic risk-based assessments of blockage have been carried out previously (Faulkner and Copp, 2001; Gschnitzer et al., 2017; Martínez-Martínez et al., 2017) though these do not enable prediction of the physical effects of blockage such as altered channel hydraulics or damage to structures. Recently, however new modelling techniques have begun to emerge. Ruiz-Villanueva and al. (2014*c*) developed a new module, within a 2D hydraulic scheme, for modelling floating debris, and applied this to analyse the impact of wood on flood magnitude. Ruiz-Villanueva and al. (2014*a*) applied the same method to investigate the influence of inlet boundary conditions on bridge clogging by wood. Likewise Stockstill et al. (2009) applied a coupled modelling scheme, previously developed for floating ice applications, to investigate the transport of floating objects at a hydraulic structure. Albano et al. (2016) developed a modelling scheme using smooth particle hydrodynamics (SPH) to investigate the effectiveness of debris counter measures known as groynes for capturing objects transported by flash floods.

The advantages of numerical modelling studies are twofold. Firstly numerical modelling is a cost and time effective means of investigating a flood event, without the need for monitoring equipment, experimental facilities or the need to travel great distances to attend a flood event. Furthermore, numerical modelling is a flexible means of investigation, where a range of scenarios can be tested with relative ease. The modelling studies discussed here represent an emerging body of work and provide the stimulus for the research presented in this study. The methodologies employed by Albano et al. (2016); Ruiz-Villanueva and al. (2014*c*); Stockstill et al. (2009) are discussed critically later in this chapter.

2.2 Characterising floating debris

Classification, quantification and size

Floating debris arises from both natural and anthropogenic sources (Rigby et al., 2002). It can be classified as: large vegetation (tree trunks, large branches, bushes), small vegetation (small branches, shrubs, grasses) and urban debris (fence posts, pallets, vehicles) (CIRIA, 2017; Rigby et al., 2002). Urban debris is diverse in nature (Rigby et al., 2002). Whereas floating trees and logs, sometimes referred to as drift, are the most frequently recorded (Transportation Association of Canada, 2004). During any individual flood

Figure 2.1: Assorted debris photographed within a 200m stretch of the River Ouseburn in Newcastle upon Tyne, at low tide (taken on 1st August 2017)

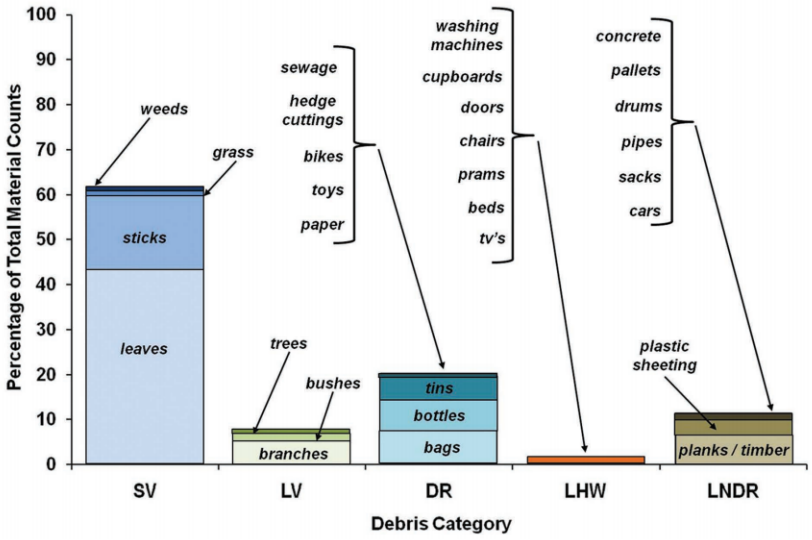

Figure 2.2: Breakdown of material types recorded by Wallerstein et al. (2013) - SV: small vegetation, LV: large vegetation, DR: domestic refuse, LHW: large household waste, LNDR: large non-domestic refuse

event, entrained debris may consist of any combination of debris classification. For example during flooding in Alyth 2015, eyewitnesses reported uprooted trees and branches, sawn and cut timber, telegraph poles and a skip (Perth and Kinross Council et al., 2015). During flooding in Boscastle, out of bank flow transported 116 vehicles downstream, along with further natural and urban debris.

Figure 2.2 shows the breakdown by type of debris caught at UK trash screens, as recorded by Wallerstein et al. (2013). The majority of debris trapped were small vegetation (60%) and domestic refuse (20%) while larger waste material was less frequently observed. Rigby et al. (2002) collected data on culvert and bridge blockages after a storm in Wollongong, 1998. They recorded that vegetation was present at 85% of blockages and that most blockages (70%) contained a mixture of vegetation and urban debris. Rigby et al. (2002) also reported the significant contribution of sediment in blockage buildup, whereas floating debris became trapped at the water's surface, sediment built up from the bed, causing partial blockage of the lower part of a structure.

Lyn et al. (2003) recorded woody debris accumulations at two field sites in Indianapolis, USA. Their study was focussed towards larger trees caught at bridge crossings and they recorded sizes ranging from $5m$ to $20m$ in length. Large woody debris (LWD) is frequently defined as having diameter greater than $0.1m$ (Bocchiola et al., 2008; Braudrick et al., 1997) and length greater that $1m$ (Comiti et al., 2016).

Spatial and temporal characteristics

There is significant catchment variability in the recruitment of debris in rivers (Comiti et al., 2016). For debris blockage at culvert trash screens, Wallerstein et al. (2013) found that urban catchments contribute the largest quantity of debris. Whereas for large wood blockage at bridges, catchments with forested channels are clearly the most at risk (Abbe and Montgomery, 1996). Where recruitment occurs downstream, woody debris tends to enter the channel through bank erosion, hillside recruitment is more likely to occur due to landslide (Comiti et al., 2016). Out of bank flow in urban areas is likely to recruit assorted urban debris including vehicles (Shu et al., 2011). Wallerstein et al. (2013) recorded seasonal variations in the occurrence of debris blockages and found that autumn and winter events were associated with the greatest likelihood of blockage, closely tailed by rainfall events following unusually dry periods. Flash flooding, usually caused by intense summer rainfall, is known for its capacity to recruit a heavy load of debris (Archer and Fowler, 2015).

2.3 Floating debris as a flash flood process

The presence of wood in rivers and streams has multiple, well-documented benefits for aquatic habitat formation (Abbe and Montgomery, 1996; Harmon et al., 2004; Murphy and Koski, 1989), sediment trapping (Montgomery et al., 2003) and local channel hydraulics (Gippel, 1995). However, rapid stage rise and high velocities, which occur during flash flooding, have the potential to mobilise otherwise stationary channel features. Out of bank flow through urban areas adds urban debris such as flooded vehicles to this cargo (Albano et al., 2016). These processes can be categorised as follows.

2.3.1 Incipient motion and entrainment

Wood is more likely to be transported on the rising limb of the flood hydrograph (MacVicar et al., 2009). For vehicles transported during flash floods, Arrighi et al. (2015) found through 3D modelling that at high Froude numbers (Fr) the fluid drag force (F_D) was most influential to motion, whereas as Fr reduced, the mechanism of incipient motion became the lift force (F_L). Recent floods in UK and France indicate that incipient conditions for swept away vehicles are shallow water depth and high velocity, which occur at high Fr numbers (Shu et al., 2011). This suggests that the force due to fluid velocity is the most significant mechanism of incipient vehicle motion. A numerical floating debris modelling tool should, therefore, consider object transport due to fluid velocity. High

water depths and fluid buoyancy also affect the incipient conditions of flooded vehicles. Chang and Shen (1979) observed that, in the USA, the greatest quantity of debris enters a river during the first major flood of the season. Through field observations, Lyn et al. (2003) clarified that a first seasonal flood may have a return period of less than 1 year and still be sufficient to mobilise this debris. Lyn et al. (2003) further found that debris transport is greatly reduced after the hydrograph peak. Through their field observations, Lyn et al. (2003) observed that logs tend to travel singularly in a channel rather than in larger clumps, whereas others (Abbe and Montgomery, 1996; Bocchiola et al., 2008; Braudrick et al., 1997) recorded that transport was often congested with multiple debris travelling down the channel as one large clump. As Braudrick et al. (1997)'s observations were made experimentally this may be due to the rate at which debris was manually introduced to the channel. For expample if a large quantity of debris was introduced at once it may continue to travel as a large mass. Abbe and Montgomery (1996) also recorded unstable debris jams that were then re-mobilized during high flows, whereas recordings by Lyn et al. (2003) were made prior to any jamming taking place. Lyn et al. (2003) observed that the delivery of debris downstream during a flood event is far from constant, rather debris arrives in bursts as different contributing areas or channels are affected by flooding. Bocchiola et al. (2006) found debris size and density, water depth, velocity and channel bed roughness as having large influence over the total distance traveled. Braudrick and Grant (2001) concluded through their theoretical and experimental results that the two most important factors in woody debris entrainment are log orientation and the presence or absence of a rootwad. This resulted in two types of debris motion; when wood moves in contact with the bed and motion due to floating (Braudrick and Grant, 2001; Braudrick et al., 1997). In marine hydraulics the rotational freedoms of a floating object are often referred to as pitch (rotation about the lateral y-axis), roll (about the longitudinal x-axis) and yaw (about the vertical z axis) (Biran, 2003). Of the available studies into floating debris entrainment, rotation about the z-axis appears to be the dominant freedom. Lyn et al. (2003) only referred to 'yaw' in their findings, where it was observed that larger logs take a stream-wise orientation and smaller woody debris took a wider range or orientations. Braudrick and Grant (2001); Braudrick et al. (1997), however observed that when logs were in contact with the channel bed they exhibited rolling, whereas when floating at the water's surface, rotation about the z-axis was dominant. In this work, floating debris travelling at the water surface is of primary concern, therefore object rotation about the vertical z-axis is investigated. There are evidently contradictory results regarding the nature of debris transport, further experimental and numerical modelling investigation is necessary to clarify the mechanisms of debris incipient transport and entrainment during

flooding.

2.3.2 Entrapment and blockage

During flooding, debris may become trapped as a singular object or as part of a large debris mass. Objects may become stationary at channel structures such as bridges and weirs and when transported to areas of elevated ground or low water depth (Bocchiola et al., 2006). Investigations into debris blockage at structures tend to be concerned with the size and deposition of the blockage, and therefore record all manner of objects including LWD and urban debris alike. Through data collection of blockages during a 1998 storm in Wollongong, Rigby et al. (2002) reported on the modes of blockage at bridges and culverts. They observed the following relationship between debris type and blockage mode;

1. **Gradual buildup of natural vegetation** - Vegetation tended to become blocked at structures after initial entrapment of a large object such as a tree trunk. This initial blockage provided support for smaller vegetation, which progressively increased the blockage size.

2. **Rapid buildup of urban materials** - Large urban materials such as refuse, fence posts, buildings waste etc. tended to rapidly block a large portion of the structure's opening. Vegetation then continued to buildup further reducing flow capacity through the opening.

3. **Instant blockage by large objects** - Less frequently, larger objects including vehicles and shipping containers instantly and totally blocked a structure's opening.

Bocchiola et al. (2006) and Lyn et al. (2003) link channel hydraulics to the blockage of LWD. Bocchiola et al. (2006) found that logs tended to become stationary in the channel when water depth was less than half the log diameter. Likewise Lyn et al. (2003) found that small depths and velocity are more conducive to debris entrapment and where one or more model log was able to rest on the flume bed, the debris pile was more stable. Diehl (1997) links entrapment to log geometry, citing log length as the parameter that most significantly affects blockage. Others also implicate structure and channel geometry. For example Bocchiola et al. (2008) cite log length relative to a bridge's opening size. For trash screens at culverts, Wallerstein et al. (2013) concluded that the ratio of the bar spacing S to the length L of cylindrical wooden dowels had the most influence on debris blockage; as $L : S$ increased, more pieces of debris became blocked. Lyn et al. (2003) suggest the ratio of log length to local water depth as an important factor and Lyn et al. (2007) observed that small spans between bridge piers led to more debris accumulations.

In UK rivers, small, single-span bridges tend to be more easily blocked than large, multi-span structures (DMRB, 1994) and culvert and bridge openings wider than about $6m$ are less likely to block (Rigby et al., 2002). Gschnitzer et al. (2017) present a summary of possible parameters affecting wood trapping probability that is provided in Figure 2.3.

2.3.3 Altered channel hydraulics

Debris jams and blockages are well-known for altering local channel hydraulics. Engineered woody debris dams are used as a feature of river restoration design to achieve desired hydraulic goals such as attenuation, bank protection and sediment trapping (Manners et al., 2007; SEPA, 2015). However unpredictable debris blockages that occur during flash flood events often cause undesirable, possibly dangerous changes to local channel hydraulics. The hydraulic effects of debris jams depend on the magnitude of flow. Although there have been many studies at base flow conditions, little data has been collected at flood discharges (Manners et al., 2007). The presence of single logs, multiple debris and entire debris jams alter the spatial distribution of shear stress (Daniels and Rhoads, 2004), which in turn has geomorphic effects on sediment size and trapping. Both Manners et al. (2007) and Hartlieb (2017) found that the density and resulting porosity of a debris blockage are a key factor in determining the hydraulic effects of such a blockage. Hartlieb (2017) conclude that the Fr number of the approaching flow also increases backwater effects of a debris jam or blockage. For blockages at hydraulic structures a debris blockage may alter the structure's hydraulic afflux. The hydraulic afflux of a bridge or culvert is defined as the maximum increase in water surface elevation above that which would exist without the structure's presence, as illustrated by Figure 2.4 (Environment Agency, 2010). During flooding this is an especially important hydraulic impact as it describes the backwater effects of a structure. Afflux is a hydraulic feature that is significantly effected by debris blockage (Roso et al., 2004). Full or partial blockage of a bridge aperture by entrapped debris causes a rise in water surface elevation immediately upstream. During the Boscastle event, a sudden stage rise of between 1m and 1.5m in the River Valency has been attributed to the rapid blockage of a bridge by floating debris (HR Wallingford, 2005).

Temporary dam failure

According to the post-event report (Dobbie and Wolf, 1953), during flooding in Lynmouth 1952, the formation and subsequent failure of temporary dams caused rapid stage rises and surge-type waves to propagate downstream. Initially, it was reported that temporary

Parameters that increase entrapment probability:

- Larger log length and log/rootstock diameter
- LWD in bulk instead of single logs or rootstocks (congested rather than uncongested transport)
- Higher stiffness values of woody debris
- More and longer branches attached on the logs
- Presence of logs from previous blockages
- Small channel and bridge geometry
- Lower freeboard
- Higher Froude numbers (supercritical flow states) if the bridge is initially dammed (no pier)
- Lower Froude number (supercritical flow states) if the bridge is initially not dammed (no pier)
- Truss bridges and bridges with open and gracefully built structures instead of smooth bridge characteristics
- Presence of a bridge pier
- Bridge piers with a triangular-shaped nose (compared with a rounded, streamlined-shaped nose)
- Bridge abutments, constricting the active discharge zone

Figure 2.3: A summary of parameters that influence trapping probability as presented by Gschnitzer et al. (2017), who cited the findings of Comiti et al. (2008); De Cicco et al. (2015); Diehl (1997); Schmocker and Hager (2011)

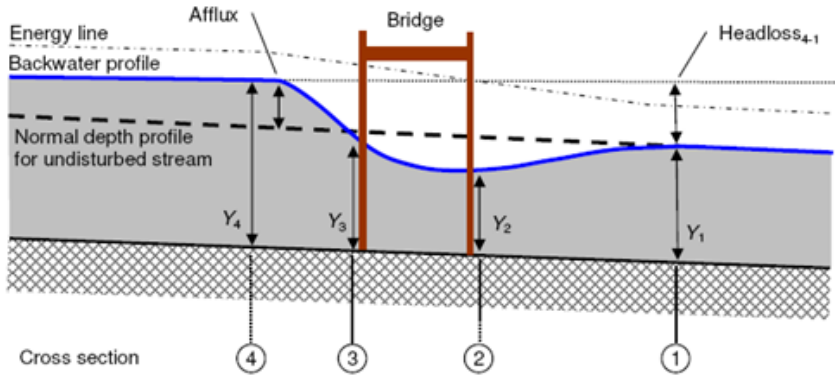

Figure 2.4: Hydraulic afflux at a flooded bridge. Bridge afflux is defined as the height of backwater above the normal depth profile for an undisturbed stream (Environment Agency, 2010).

dam failure caused surge waves during Boscastle flooding (Fenn et al., 2005). However this theory was later discredited and sudden stage rise attributed to sudden blockage at a downstream bridge (HR Wallingford, 2005). There are clearly uncertainties regarding the significance of temporary dam failure during flash flooding. A numerical modelling tool that simulates this process would enable further investigations to be performed.

2.4 Implications for hydraulic structures

Debris blockage is one of the primary causes of bridge failure in the UK (Ebrahimi et al., 2016). Benn (2013) assessed the failure of railway bridges due to flooding since the 1840s and recorded that 20 of 69 incidents were associated with floating debris. While undermining of abutments and piers by scour was the most common failure mode, debris action increasing local scour and the location of bridges in rapid-response catchments made up the second most common sequence (Benn, 2013). Masonry bridges, in particular, are vulnerable to blockage by debris because of their short spans and low clearance (Ebrahimi et al., 2016). Masonry arch bridges make up a large proportion of UK bridge infrastructure and in particular are often situated over low order streams in small steep sided catchments, so are also vulnerable to flash flooding. Debris blockages do not act in isolation, instead a single bridge failure may generate a cascading sequence of failures down a watercourse, as the initial debris blockages are released and trapped at subsequent structures (DMRB, 1994). It is, therefore, not sufficient to consider a single bridge blockage during an event. Instead, the processes of structural blockage should be treated as a dynamic system.

2.4.1 Flood actions on bridges

Structural damage and failure of bridges is frequently associated with flooding. Scour at bridge piers and abutments is most commonly cited as the dominant hydraulic action, however a range of other processes may also combine to increase the likelihood of failure. By effectively increasing the dimensions of piers and abutments, floating debris contribute to increased scour depth in excess of those observed without debris accumulation (Abbe and Montgomery, 1996; Melville and Dongol, 1992). Hydrostatic action due to elevated afflux contributes to the horizontal load and is increased further still under the gradual build up of debris (Kelman and Spence, 2004). Increased hydrodynamic forces due to flow velocity contribute to horizontal loads at submerged faces (Martínez-Martínez et al., 2017; Parola et al., 2000). Additional dynamic actions are generated by the direct impact of floating debris against a structure (DMRB, 1994; Kelman and Spence, 2004). Haehnel and Daly (2002) suggest that the magnitude of this force can be enough to cause substantial, even catastrophic damage to structures. Whereas, according to Diehl (1997), direct impact alone is rarely the cause of structural failure, rather, increased backwater, flow velocity and deeper foundation scour all act in unison with impact load. The maximum debris impact forces are found to occur due to end-on impact, followed by a 90° rotation and are minimised with eccentricity and obliqueness (Haehnel and Daly, 2002). For submerged structures, a buoyant force acts vertically to reduce the effective unit weights of submerged components. Where unit weight is beneficial to the strength of a bridge, eg. masonry arch bridges, buoyant forces can reduce the vertical load carrying capacity by up to 50% (Hulet et al., 2006). Where buoyant lift acts in unison with increased horizontal loads bridge stability may also be reduced by increasing the overall effects of horizontal forces.

2.4.2 Current guidance

Bridge design guidelines relevant to UK infrastructure make consideration for debris actions on bridges in varying levels of detail. The Design Manual for Roads and Bridges (DMRB) is adopted by Highways England, Transport Scotland, Welsh Government and DRD Northern Ireland for road bridge design. DMRB includes guidance on bridge design under flood debris collision forces and additional hydrodynamic loads due to debris obstruction (DMRB, 1994). UK rail infrastructure falls under Network Rail Design Guidance, which makes reference to debris load in response to extreme weather conditions.

When assessing the robustness of a structure under flood conditions, DMRB requires assessment of the potential for debris to block flow. Consideration of direct impact from

debris is suggested where the flood energy line reaches a threshold of 0.6m below the structure's soffit. Scour due to debris blockage can be predicted for hydraulic design by assuming a larger effective cross section for the bridge pier. However, accurate predictions of the size of such jams are hampered by a lack of evidence documenting blockage sizes (Melville and Dongol, 1992).

Frequently, hydraulic modelling is considered by other civil engineering disciplines, especially the design and assessment of structures spanning rivers. Hydraulic models are able to predict complex pressure fields around structures which enable accurate load considerations. However, there is evidently a disparity between structural design requirements for bridges at risk of debris contact and the capability of hydrodynamic modelling tools used to influence design. UK design guidelines make clear consideration of floating debris induced scour and impact force. However the majority of hydraulic modelling negates debris as a process entirely.

2.5 Implications for modelling floating debris

The processes surrounding floating debris transport have significant implications for flood modelling. The hydraulic effects of debris entrapment on bridge afflux and out of bank rerouting may vastly alter actual flood extent. However, there are currently no commercially available flood modelling tools that intrinsically predict the transport and entrapment of floating debris.

2.5.1 Current modelling approaches

The effect of a blockage can be accounted for in virtually any hydraulic modelling package, by manually altering the dimensions of structural openings (Benn et al., 2004). For example, numerous studies have applied hydrodynamic modelling to the 2004 Boscastle event, where debris entrapment at two bridge openings significantly altered flow paths. Kvočka et al. (2015) assumed 100% blockage of both bridges throughout computation, and recreated this within their model by raising the bed elevation to road level at the two bridges, thus preventing flow from passing under. Lhomme et al. (2010) represent both bridge openings as orifices, and based on video footage, reduce the bridge openings by a factor of two, so as to allow a proportion of flow through the partial blockages. Roca and Davison (2010) apply the most dynamic approach of the three by treating the upstream road bridge as an empirical sluice gate, whose size is modified during the simulation to replicate progressive blockage. While all of the approaches produce reasonable results for

total inundation extent and water depth, they first require existing knowledge of where and when blockages occurred. This information is not usually known prior to the event so is only possible for post event reconstructions. Nor does this method enable investigation into the cascading nature of debris blockages during the flood. For example in Boscastle, whether blockage at the first bridge contributed to the successive blockage at the second. Furthermore each approach taken by Kvočka et al. (2015), Lhomme et al. (2010) and Roca and Davison (2010) assumes an entirely different value for the proportion of the bridge blocked by debris. This further demonstrates the requirement for tool which can predict the quantity of debris blocking a structure.

Of the available commercial modelling packages, few intrinsically incorporate the effects of floating debris (Samuels, 2004). Benn et al. (2004) summarise the built-in functionality of commercial modelling packages HEC-RAS, ISIS and MIKE11 for modelling debris blockage. The MIKE11 package does not incorporate in-built blockage facilities, but as with any scheme, channel dimensions can be altered manually. The ISIS and HEC-RAS packages allow the user to represent transient blockage as a sluice gate, as demonstrated by (Roca and Davison, 2010). While the HEC-RAS package can account for debris accumulation around bridge piers and openings by altering structure dimensions (Brunner, 2016). A cylinder is applied around bridge piers to increase its effective diameter; while the rectangular dimensions of a debris blockage at bridge openings and culverts is specified by adjusting area and wetted perimeter. Though the HEC-RAS package contains more advanced blockage functionality, all three methods still require knowledge of the total blockage size prior to computation.

The outputs of such tools may provide valuable information for assessment of the effected hydraulic structures, such as providing depth and velocity profiles around the blocked structure. However, none of the approaches discussed provide any indication of the quantity of debris impacting blocked structures and are therefore are of little use for assessing bridge stability under debris impact loading.

Debris blockage is a dynamic process (Roso et al., 2004), where entrapment occurs progressively and successively, possibly at many different sites across a catchment. Cascading failure due to temporary dam or structural failure further complicates a catchment's response to flooding when debris is involved. This presents a clear challenge for modelling as it is not directly obvious at what time blockages will occur and what combination will generate the highest flood level. Static modelling techniques, where blockage characteristics are predefined (Benn et al., 2004; Brunner, 2016; Roca and Davison, 2010), may produce valuable information when applied to a single blocked structure. However for events where multiple blockages occur in succession, or if structural assessment requires

prediction of debris impact; a more detailed and dynamic modelling approach is required.

2.5.2 Discrete element modelling of floating objects

Within the research environment there is a growing body of work aimed directly at modelling the dynamic transport and entrapment of floating objects. Such modelling tools have been developed to investigate object transport by dam break waves (Amicarelli et al., 2015; Jian et al., 2016), tsunami (Piche et al., 2014); river flow (Daly and Hopkins, 1998, 1999, 2001, Hopkins and Daly, 1999, Hopkins et al., 1996, Hopkins and Tuhkuri, 1999, Hopkins and Tuthill, 2002); and most recently by flash flooding (Stockstill et al., 2009, Albano et al., 2016, Ruiz-Villanueva and al., 2014*b*,*c*). The majority of these studies (eg. Piche et al., 2014; Robb et al., 2016; Stockstill et al., 2009) include floating objects within their numerical scheme by coupling a hydrodynamic model with the discrete element method. This combined approach was first proposed for simulating the behaviour of floating river ice (Hopkins et al., 1996) but has since been developed for more general application to floating object transport (Stockstill et al., 2009).

The discrete element method (DEM) is a numerical modelling technique that describes the mechanical behavior of assemblies of objects (Cundall and Strack, 1979). Since it was first proposed by Cundall and Strack (1979) for modelling the behavior of geotechnical granular assemblies, DEM has been used to simulate many other physical problems across research areas (eg. Fleissner et al., 2007; Gifford et al., 2006; Ma et al., 2015). Applying DEM to model floating objects is now a growing area of research; DEM has so far been used to investigate the transport of river ice (Hopkins et al., 2002), impact forces due to ice collision with structures (Daly and Hopkins, 2001), ice jam formation (Hopkins and Daly, 1999), and floating object entrapment at river structures (Stockstill et al., 2009). Simulating the mechanical behavior of discrete objects is achieved by first resolving its contact and body forces, then performing numerical integration to solve the equations of motion (Cundall and Strack, 1979). To simulate the mechanics of objects in flotation the DEM is coupled with a hydrodynamic scheme through application of additional hydraulic forces. These hydraulic forces are generally a combination of vertical buoyancy and horizontal fluid drag (Stockstill et al., 2009).

2.5.3 Hydrodynamic modelling of floating objects

In physics the Navier-Stokes equations are a system of non-linear partial differential equations (PDEs) that describe the momentum conservation of a moving fluid. This system of equations requires numerical methods to solve. By making reasonable assumptions,

including negligible vertical acceleration, the Navier Stokes equations may be simplified to derive a set of 2D PDEs (shallow water equations) and 1D PDEs (St. Venant equations). Numerical schemes that solve these systems of equations are frequently applied to environmental shallow flow problems (eg. rivers, lakes and coastal lagoons) and have been applied to simulate flow fields governing debris transport (Ruiz-Villanueva and al., 2014*b*,*c*; Stockstill et al., 2009).

Daly and Hopkins (1998, 2001) couple DEM with a 1D flow model to simulate river ice transport. Daly and Hopkins (1998) simulate transport within a uniform rectangular channel, whereas Daly and Hopkins (2001) simulate a rectangular channel with variable cross-sectional geometry. These methods are limited in their applications to unidirectional flow where object transport can also be considered as being 1D. The main advantage of 1D approximations is their low computational cost. However, 1D hydrodynamic modelling is not suitable for simulating complex flow patterns where flooding occurs in urban areas or where out of bank flow connects the floodplain. Alternatively Ruiz-Villanueva and al. (2014*b*,*c*); Stockstill et al. (2009) apply a 2D depth averaged flow model to simulate depth and velocity fields within their coupled models. Simulating depth and velocity profiles in 2D widens the possible model applications to more complex domains including urban settings, however gains in accuracy inevitably incur computational cost. Nonetheless, 2D schemes achieve accelerated computation time over 3D approaches by assuming hydrostatic vertical pressure and are regularly applied to simulate environmental shallow flows.

Within the existing studies, a number of mesh or grid based numerical methods for solving the hydraulic equations have been coupled with DEM for simulating floating objects. Stockstill et al. (2009) apply the finite element method (Stockstill et al., 2005) where the PDEs are discretized by a structured mesh and flow variables are calculated for each node. Whereas Ruiz-Villanueva and al. (2014*b*,*c*) apply the finite volume method where the PDEs are partitioned into a set of fluid volumes with flow variables usually stored at the centre. The finite volume method is well-suited to computational hydraulics due to its robust handling of conservation laws and speed of computation. Recent advances in computing power have enabled the development of numerical schemes that further accelerate computing through parallel processing across multiple GPUs. Parallel processing has been successfully applied to a number of hydrodynamic schemes including those that employ the finite volume method (Amouzgar et al., 2014; Liang and Smith, 2015; Liang et al., 2016; Smith et al., 2014). However grid-based numerical methods are often not a good choice for modelling discrete systems (Liu and Liu, 2010), therefore coupling with DEM is not straightforward.

Smoothed particle hydrodynamics (SPH) is a mesh-free Lagrangian method for solving the governing hydrodynamic equations. In SPH, a continuum fluid is represented by a set of particles that store fluid properties and flow variables. The motion of the fluid is represented by the motion of the particles, thereby overcoming cell interface problems encountered through mesh/grid based methods (Liu and Liu, 2010). Furthermore, SPH lends itself to solving the full 3D Navier Stokes equations, thereby simulating both horizontal and vertical velocity profiles. SPH is effective for modelling discrete systems (Liu and Liu, 2010) and therefore appears well-suited for coupling with DEM. Ren et al. (2014); Robb et al. (2016) couple SPH with DEM to simulate object-wave interaction for experimental validation cases. And Piche et al. (2014), Jian et al. (2016), Amicarelli et al. (2015) and Albano et al. (2016) simulate fluid-object interaction through alternative SPH methods. Piche et al. (2014) apply SPH to calculate debris and hydrodynamic impact loads. Amicarelli et al. (2015) simulate solid body transport. Albano et al. (2016) simulate object transport around fixed obstacles. However, these simulations require relatively high computation time compared to other methods and as such SPH has historically had few applications outside of academia (Jian et al., 2016). Furthermore, the studies presented by Piche et al. (2014), Jian et al. (2016), Amicarelli et al. (2015), Ren et al. (2014) and Albano et al. (2016), simulate only small-scale experimental test cases. There, therefore, remains a requirement for a coupled hydrodynamic-DEM floating debris modelling tool that is suitable for modelling real-world flash flood applications.

Though coupling is less intuitive than with discrete meshless systems such as SPH, the finite volume method is applied in this work for coupling with DEM. A GPU accelerated finite volume scheme developed at Newcastle University (Liang, 2010) has been demonstrated as capable and efficient at simulating real world applications and shock-like hydraulics. As the aim of this work is to model floating debris transport during real-world flash flood events, computational efficiency is favoured over numerical practicality. As coupling between finite volume and DEM schemes has been attempted by relatively few, the coupling approach presented in this work is entirely new.

2.5.4 Coupling procedures

Previous coupling between hydrodynamic schemes and DEM has been achieved through hydraulic force application. Where hydraulic forces are passed to the DEM, partial coupling is achieved (Stockstill et al., 2009). Where a reciprocating force is applied to fluid cells, Newton's third law is satisfied and full coupling is achieved (Ruiz-Villanueva and al., 2014*b*,*c*). Partially coupled models cannot simulate backwater effects and are therefore only applicable where backwater is considered insignificant. For example, Stockstill

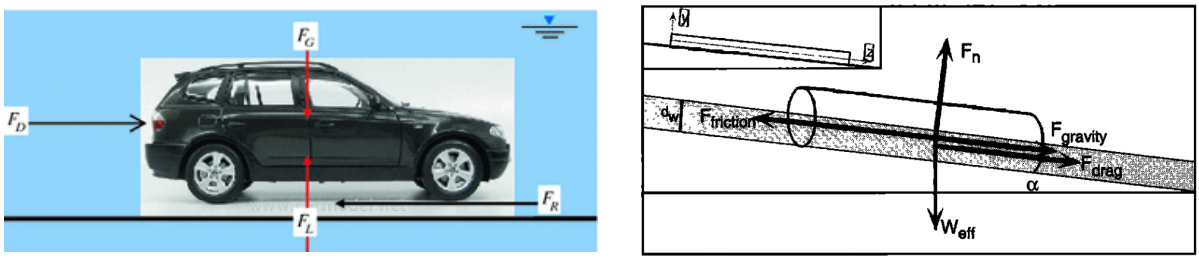

(a) Forces on a flooded vehicle (Xia et al., 2011) (b) Forces on a log (Braudrick and Grant, 2000)

Figure 2.5: Possible forces combinations that act on a fully or partially submerged object.

et al. (2009) present a partially coupled modelling tool and simulate the transport of floating debris passage through the Harlem Diversion Tunnel. Stockstill et al. (2009) justify only partial coupling for this application as debris concentrations are low within the domain and have minimal effect on the observed flow dynamics. Alternatively Ruiz-Villanueva and al. (2014*c*); Ruiz-Villanueva and al. (2014*b*); and Daly and Hopkins (2001) demonstrate full force coupling by also applying a counter force to the fluid cells where objects are present. When estimating the forces on an ice control structure, Daly and Hopkins (2001) justify full coupling as ice build-up generates backwater effects. Likewise, Ruiz-Villanueva and al. (2014*c*) apply the counter force as an additional shear stress to simulate the backwater effects of debris entrapment at a bridge. The additional shear stress causes water depth to rise and velocity to decrease, thereby simulating the effects of increased hydraulic afflux. In this study, full force coupling is deemed necessary as floating objects transported during flash flooding have the capacity to significantly alter channel hydraulics, particularly afflux at bridges.

Hydraulic and object force formulae

Xia et al. (2011) summarise the forces acting on a submerged vehicle, Figure (2.5a), as submerged weight (F_G) resulting from gravitational and boyant forces; a lift force (F_L); a fluid drag force (F_D); and a frictional force (F_R) resisting vehicle sliding on the road's surface. Braudrick and Grant (2000) record the same force combination as acting on a partially submerged log (Figure 2.5b).

In their coupled modelling scheme, Stockstill et al. (2009) apply a force combination consisting of horizontal fluid drag and vertical buoyancy to modelled objects.

$$F_f = -\rho A_i C_d (w_i - V_f)|w_i - V_f| + F_B \tag{2.1}$$

where ρ is the fluid density; A_i is object area; w_i is object velocity; V_f is fluid velocity; and F_B is the buoyant force acting perpendicular to the water surface. The drag coefficient

(C_d) is an empirically derived, dimensionless value that varies with Reynold's number (Malavasi and Guadagnini, 2007). Daly and Hopkins (2001); Hopkins and Daly (1999) apply fixed values of $C_d = 1.17$ and $C_d = 0.1$ for flow in the normal and tangential directions, assuming turbulent conditions throughout the simulation. Brooks et al. (2006) propose a drag coefficient equal to 1.2 for wood transport in real streams, this value is applied by Ruiz-Villanueva and al. (2014*c*) to investigate wood transport within a short stream reach. Whereas Bocchiola et al. (2006) found a value of 1.4 for wooden dowels in a flume experiment. The force combination consisting of buoyancy and drag (Equation 2.1), including use of the drag coefficient, is adopted across other floating object transport studies (Daly and Hopkins, 1998, 1999; Hopkins and Daly, 1999; Hopkins et al., 1996; Hopkins and Tuhkuri, 1999; Hopkins and Tuthill, 2002).

To achieve full model coupling Ruiz-Villanueva and al. (2014*c*) calculate an additional force resulting from the presence of woody debris that is applied to fluid cells. The resulting object shear stress (τ_{wood}) calculated by Ruiz-Villanueva and al. (2014*c*) is given by Equation 2.2 and results from the fluid drag force F_d acting over the area of the fluid cell A_f.

$$\tau_{wood} = \frac{\sum F_d}{A_f} \tag{2.2}$$

Use of the drag coefficient

Fluid drag force depends on the dimensionless fluid drag coefficient C_d according to Equation 2.3.

$$C_d = \frac{F_d}{\frac{1}{2}\rho A U^2} \tag{2.3}$$

The drag coefficient is used to encapsulate the effects of two distinct force patterns (Chadwick et al., 2013). These are:

1. Frictional shearing due to viscous forces at the boundary layer. This is also refered to as viscous drag.

2. Flow separation around 'bluff' object shapes that creates a localised pressure difference upstream and downstream of the object. This is also referred to as form drag .

The value of C_d is dependent on object shape, object material, and importantly, fluid viscosity. Use of the drag coefficient to determine forces on a floating object during flash flooding presents a number of problems. Firstly, C_d should be derived empirically for each different object transported by flooding. Its value depends upon Reynold's number

(Malavasi and Guadagnini, 2007) and C_d should therefore be treated as a dynamic variable that varies throughout computation. Furthermore use of C_d is in direct conflict with the inviscid assumptions made in the SWEs and St. Venant governing equations. Despite this, Stockstill et al. 2009; Ruiz-Villanueva and al. 2014*c*; Ruiz-Villanueva and al. 2014*b*; and Daly and Hopkins 2001 routinely apply fixed values of C_d when calculating horizontal fluid drag. There is therefore still a requirement for a coupled floating debris modelling tool where force calculation is based on theoretical principles that are consistent with the governing hydraulics. This work will aim to address the research gap by proposing an alternative force calculation method.

Alternative force calculation

Objects that become entrapped at hydraulic structures will experience an additional force caused by hydraulic afflux. Where entrapment occurs, reduced upstream velocity will decrease the drag force. However, as water depth behind the blockage increases, a hydrostatic pressure will be exerted on the blocked objects. Previous studies do not account for this hydrostatic force, and as coupled debris modelling tools remain a relatively emerging body of work, few alternative force combinations are offered. However, a large body of research exists into quantifying the forces acting on a submerged structure and their findings can also be applied here. When summarising flood related actions on buildings, Kelman and Spence (2004) describe a hydrostatic lateral pressure, imparted by water depth; and hydrodynamic lateral pressure, imparted by fluid velocity. Similarly Aureli et al. (2015) calculate the total normal force acting on a vertical, flow facing wall subject to impact from a dam break wave, as the sum of the hydrostatic force and momentum flux term (hydrodynamic force) at each cell adjacent and normal to the wall. Liang et al. (2016) derive the total hydraulic force as the sum of the force due to static pressure and fluid momentum (Equation 2.4). Liang et al. (2016) further validate the hydrodynamic and hydrostatic pressures combination experimentally for a vertical structure impacted by a dam break wave.

$$F = P + \rho Q U \tag{2.4}$$

Equation 2.4 calculates the total hydraulic force as presented by Liang et al. (2016), where F is the total force across a fluid cross section; P is the total force due to fluid pressure; Q is the total discharge through a cross section; and U is fluid velocity.

2.6 Conclusion

Though there have been a number of efforts to include floating debris into hydrodynamic schemes, techniques are varied and inconsistent. There remains a need for a fully coupled debris modelling tool that that has the necessary capabilites for modelling debris transported by flash flooding in the UK. In light of the reviewed literature in this chapter, a set of criteria are developed that represent the minimum requirements of a floating debris modelling tool developed for flash flood application. These are presented below.

Criteria for modelling floating debris

1. **Represent a range of object shapes and scales** - It is necessary that a modelling tool is able to represent the diverse range of objects commonly observed during flash flooding.

2. **Consider a range of material properties** - A range of object materials have been reported as contributing to floating debris. These different materials interact differently with flow. It is, therefore, necessary that a modelling tool considers material properties as part of its transport calculations.

3. **Predict translational and rotational motion** - Translational and rotational motion are critical factors contributing to debris blockage. The research suggests that horizontal translation at the water's surface and rotation about the vertical axis are the most influential to debris dynamics.

4. **Capture hydraulic shocks** - Complex hydraulic phenomena must be captured, especially the shock-like flows observed after blockage or levee failure.

5. **Enable object 'clumping'** - The 'clumping' together of objects has been shown to be a key property of debris transport and a critical factor in blockage generation at structures. A modelling scheme should consider frictional object properties that prevent sliding.

6. **Generate backwater effects** - The position and blockage of debris should also influence flow patterns. A floating debris modelling tool should also simulate the backwater effects of debris blockages.

7. **Employ a physically based numerical scheme** - So as to reduce the requirement for model calibration, the modelling scheme should be physically based.

8. **Maintain consistency across modelling techniques** - Numerical assumptions should be maintained across coupling to ensure numerical consistency.

9. **Use explicit variables where possible** - To further reduce the need for model calibration, variables should be explicit and fixed where possible.

Chapter 3

Numerical methods

Two distinct numerical methods are employed in this work. The hydrodynamic method solves a set of governing hydraulic equations and predicts flow variables. The discrete element method solves the equations of motion for a system of objects and is used to predict object transport variables. This chapter presents the two numerical methods, giving justification, calculation procedure and any associated assumptions and limitations. The discrete element scheme presented in this chapter has been developed specifically for this work. Analytical verification is presented for three idealised test cases, demonstrating that the scheme solves equations of motion to an acceptable level of accuracy. The hydrodynamic scheme has been extensively validated previously, therefore no model validation is presented here.

3.1 Hydrodynamic method

3.1.1 Governing equtations

The 3D Navier-Stokes equations are derived from conservation of mass and linear momentum principles and describe the flow of Newtonian fluids. These 3D equations are computationally costly to solve but practical assumptions and simplifications can be made for certain applications. By assuming an inviscid fluid and hydrostatic conditions in the vertical plane, the Navier-Stokes equations can be depth integrated to produce a 2D approximation. The resulting set of PDEs are known as the shallow water equations (SWEs) and are applicable to shallow flow phenomena. In computational hydraulics, many natural water bodies that extend over large areas can be considered as environmental shallow flows. For example wide rivers, flood plains, shallow lakes and large coastal lagoons all have horizontal dimensions that far exceed vertical depth and so can be described by the

SWEs. Numerical solutions to the SWEs have been applied successfully to simulate flash flooding (Liang et al., 2016), coastal surge (Qiang et al., 2016), tsunami (Amouzgar et al., 2014) and dam break applications (Wang et al., 2011).

In their conservative from the SWEs can be written as a system of hyperbolic PDEs:

$$\frac{\partial \boldsymbol{q}}{\partial t} + \frac{\partial \boldsymbol{f}}{\partial x} + \frac{\partial \boldsymbol{g}}{\partial y} = \boldsymbol{s} \tag{3.1}$$

were $\boldsymbol{q}$ is a vector containing flow variables, $\boldsymbol{f}$ and $\boldsymbol{g}$ are flux vectors in the x and y directions and $\boldsymbol{s}$ is a vector containing source terms. These vectors are given by:

$$\begin{gathered} \mathbf{q} = \begin{bmatrix} \eta \\ q_x \\ q_y \end{bmatrix} \mathbf{f} = \begin{bmatrix} q_x \\ uq_x + \frac{g}{2}(\eta^2 - 2\eta Z_b) \\ uq_y \end{bmatrix}, \\ \mathbf{g} = \begin{bmatrix} q_y \\ vq_x \\ uq_y + \frac{g}{2}(\eta^2 - 2\eta Z_b) \end{bmatrix}, \mathbf{s} = \begin{bmatrix} 0 \\ -\frac{\tau_{bx}}{\boldsymbol{\rho}} - g\eta\frac{\partial z_b}{\partial x} \\ -\frac{\tau_{by}}{\boldsymbol{\rho}} - g\eta\frac{\partial z_b}{\partial y} \end{bmatrix} \end{gathered} \tag{3.2}$$

where Z_b is bed elevation, η denotes water surface elevation and q_x and q_y are the unit width discharges in the x and y directions. Water depth is defined as $h = \eta - Z_b$ and the x and y depth averaged velocities are given by $u = q_x/h$ and $v = q_y/h$. Acceleration due to gravity is g. Bed friction shear stresses in the x and y directions are given by:

$$\tau_{bx} = \rho C_f u\sqrt{u^2 + v^2} \tag{3.3}$$

$$\tau_{by} = \rho C_f v\sqrt{u^2 + v^2} \tag{3.4}$$

where water density is ρ, the bed roughness coefficient is defined as $C_f = gn^2/h^{1/3}$ and n is the Manning coefficient.

The SWEs can be approximated further still for unidirectional flow to derive the 1D St. Venant equations. These are a 1D system of governing equations given in their conservative matrix form by Equation 3.5 and 3.6. The St. Venant equations are applicable to flow propagation in river systems and channels where velocity profile is approximately uniform in the horizontal as well as vertical direction.

$$\partial_f \mathbf{u} + \partial_x \mathbf{f} = \mathbf{s} \tag{3.5}$$

$$\mathbf{u} = \begin{bmatrix} \eta \\ q \end{bmatrix}, \mathbf{f} = \begin{bmatrix} \mathrm{q} \\ \frac{q^2}{\eta - Z_b} + \frac{g}{2}(\eta^2 - 2\eta Z_b) \end{bmatrix}, \quad \mathbf{s} = \begin{bmatrix} -\frac{\partial_x b(x)}{b(x)} q \\ -\frac{\partial_x b(x)}{b(x)} \frac{q^2}{\eta - Z_b} - g\eta \partial_x Z_b - C_f u|u| \end{bmatrix} \tag{3.6}$$

where q is the unidirectional flow and $b(x)$ is the bed width for a rectangular cross section.

For most applications, there is no analytical solution to the governing SWEs and St. Venant equations (Chadwick et al., 2013) and numerical methods provide a practical means of solving many shallow water problems. Here a finite volume scheme is applied to update flow variables with respect to time.

3.1.2 Finite volume Godunov-type scheme

The finite volume method is a widely used numerical approach to solving hydraulic equations and Godunov-type schemes, in particular, are often favoured for their robustness and accuracy in capturing discontinuities. In this work, a well-balanced Godunov-type scheme is applied to predict flow variables in both 1D or 2D. The numerical schemes use a second order framework and in both cases, shock capturing is achieved by solving local Riemann problems to capture discontinuities at the cell interface.

A 1D scheme

A 1D scheme proposed by Alias et al. (2011) is used in this work. The scheme solves the governing St. Venant equations (Equations 3.5 and 3.6) using a two-step Runge-Kutta time integration. At each time instance n the flow variables contained within a cell i are advanced to the next time interval $(n+1)$ by:

$$\boldsymbol{u}_i^{n+1} = \boldsymbol{u}_i^n + 0.5\Delta t[\mathbf{K}_i(\boldsymbol{u}^n) + \boldsymbol{K}_i(\boldsymbol{u}^*)] \tag{3.7}$$

where $\boldsymbol{K}_i = -(\boldsymbol{f}_{i+1/2} - \boldsymbol{f}_{i-1/2})/\Delta x + \boldsymbol{s}_i$ is the space discretisation operator and $\boldsymbol{u}_i^* = \boldsymbol{u}_i^n + \Delta t \boldsymbol{K}_i(\boldsymbol{u}^n)$ is the intermediate stage flow vector. The size of cell, i is given by Δx . Within each time interval, fluxes across cell interfaces, $\boldsymbol{f}_{i+1/2}$ and $\boldsymbol{f}_{i-1/2}$ are found by evaluating local Riemann problems at the cell interfaces.

In this 1D scheme a MUSCL linear interpolation is used to reconstruct face values from flow data at the cell centres. a Min/Mod slope limiter is applied to wet cells away from wet and dry fronts. While at dry cells or wet-dry fronts, face values take on the values at the cell centre. This enables positive depth preservation. These Riemann states

are then employed by a Harten, Lax and van Leer (HLL) approximate Riemann solver to compute the interface fluxes. For full details of the non-negative reconstruction of Riemann states see Alias et al. (2011).

The source terms for the momentum equation, which can be split into bed slope and bed friction terms are evaluated directly using a central differencing scheme. This is in accordance with the depth-positivity-preserving Riemann states of water surface and single value for bed topography. For full details of the source term discretisation see Liang and Marche (2009).

In this work the 1D scheme is implemented in the programming language C++. By using C and its derivatives across all numerical methods, model coupling is made simpler as information can be passed between numerical schemes without the need for language translation.

A 2D scheme

The 2D scheme used in this work was developed by Liang (2010). The scheme is similar to the 1D scheme proposed by Alias et al. (2011); it employs a Runge-Kutta time integration and central difference approach to source term discretisation; but also makes some improvements. The scheme uses a Harten, Lax and van Leer approximate Riemann solver with the contact wave restored (HLLC) (Liang, 2010; Liang and Borthwick, 2009; Toro et al., 1994). The HLLC method, introduced by Toro et al. (1994) is a three-wave model that achieves improved accuracy over the HLL solver (Toro, 2009).

The scheme is accelerated through parallel processing across multiple GPUs implemented in compute unified device architecture (CUDA) (Amouzgar et al., 2014). The CUDA platform is designed to work with C and C++ programming languages and therefore maintains compatibility when coupled with schemes across these languages. The accelerated scheme is able to achieve significant improvements in computation time when compared to the same numerical method running on a single central processing unit (CPU) core.

Time step stability

An adaptive timestep is employed to enable numerical stability while ensuring computational efficiency (small time step is only used when necessary). The time step is controlled by the Courant-Friedrichs-Lewy (CFL) criterion (Liang, 2010; Toro, 2001) and may be

expressed as

$$\Delta t = Cmin\left(min_{i,j}\frac{\Delta x}{|u_{i,j}| + \sqrt{gh_{i,j}}}, min_{i,j}\frac{\Delta y}{|v_{i,j}| + \sqrt{gh_{i,j}}}\right) \tag{3.8}$$

where $0 < C \leq 1$ and in this work $C = 0.5$.

Assumptions and limitations

The hydrodynamic modelling scheme assumes hydrostatic conditions in the vertical profile and therefore predicts velocity values that are averaged by depth. Actual values for velocity differ through vertical depth and velocities at the waters surface tend to be larger than the averaged values. Because of this assumption, the modelling scheme slightly underestimates the surface velocity; a variable that is likely to have the greatest influence over floating debris.

The hydrodynamic scheme assumes an in-viscid liquid and therefore negates boundary shear due to viscous forces. For flow in a rectangular channel, for example, the horizontal velocity profile is effected by viscous drag at the channel sides but this will not be captured within numerical predictions.

3.2 Discrete element method

There are a number of widely available commercial and open-source discrete element modelling systems. The most well known include: Yet Another Dynamic Engine, (YADE) (Šmilauer and al., 2015); Large-scale Atomic/Molecular Massively Parallel Simulator (LAMMPS/ LIGGGHTS) (Plimpton, 1995); and commerical software packages such as PFC 2D/3D (Itasca, 1998). Applications of these packages vary significantly. For example, published applications of the YADE software include powder compaction (Chareyre et al., 2012; Harthong et al., 2012; Jerier et al., 2011)); soil mechanics (Aboul Hosn et al., 2017; Duriez and Wan, 2017; Tran et al., 2013); and granular flows (Albaba et al., 2015; Favier et al., 2013; Maurin et al., 2016). However, most applications share the common characteristics of simulating a large number of particles (> 10000) with small particle sizes ($< 10mm$). It is for this reason that programmes, such as YADE, feature material properties and contact parameters relevant to microscale particles; contact detection algorithms for simulating a large number of particles; and numerous subroutines that replacate micro-scale particle behavior.

Application of DEM to floating debris transport is limited to a few academic studies

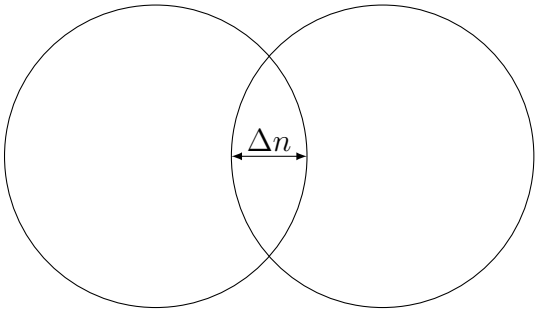

Figure 3.1: Two contacting spheres are allowed to overlap within the DEM. The magnitude of the overlap is defined by Δn.

(Stockstill et al., 2009). Such applications differ from conventional DEM studies in both scale and number of objects. Although floating debris varies in size and shape, comparatively object diameters are large ($> 10mm$). Likewise, when compared to conventional DEM, floating debris applications require much fewer objects to be computed (< 200). Therefore, many of the more advanced software capabilities, such as modelling cohesive materials, plastic deformation and non-linear damping, are surplus to the requirements of a floating debris modelling tool.

For this reason, a new discrete element modelling scheme is here developed that is specifically suited to modelling the material characteristics and contact behavior of commonly found flash flood debris. Only the required model capabilities are included so as to minimise computation time and maintain source code simplicity. Additional subroutines are derived and presented in Chapters 4 and 5 to enable hydrodynamic coupling.

3.2.1 Theory

The Discrete Element Method (DEM), initially introduced by Cundall and Strack (1979) predicts the motions of objects in collision. In its simplest form, the method treats objects as discrete circles in 2D, or spheres in 3D (here spherical terminology refers to both 2D and 3D). Simulation time is discretised into small intervals and at each time interval sphere motion is predicted. Objects are rigid; however, contacts between objects are detected by permitting spheres to overlap, illustrated in Figure 3.1. Inter-object contact forces are calculated according to an idealised contact model, where accuracy of contact forces depends on the sophistication of the contact model (Zhang and Whiten, 1996). Object acceleration is calculated according to Newton's second law (Equation 3.9) and subsequent object motion is predicted through time integration of the equations of motion.

$$\sum F = ma \tag{3.9}$$

where F is the force applied to an object, m is object mass and a is object acceleration.

Contact mechanics

The contact model employed by DEM predicts the forces acting at the point of contact between two colliding spheres. Cundall and Strack (1979) proposed a contact model consisting of an elastic spring, viscous damper and friction slider that has been adopted by many researchers. Many improvements have also been made on the contact model for simulation of more realistic forces.

The simplest contact model is a linear spring-dashpot type where the magnitude of the contact elastic force is directly proportional to the magnitude of the overlap Δn and the viscous force is directly proportional to sphere velocity. However, Zhang and Whiten (1996) reported a number of errors associated with a linear spring damping model, such as: initially predicting negative attractive contact forces between overlapping spheres; and calculating unrealistically large forces between objects that are then transmitted to other objects within the simulation.

As an alternative, Tsuji et al. (1992) present a discrete element scheme based on Hertzian contact theory that employs a non-linear visco-elastic contact model. Here the system stiffness is proportional to displacement and the viscous damping term is proportional to both displacement and velocity. When comparing linear and non-linear contact models applied to powder simulations, Zhang and Whiten (1996) found that both approaches resulted in erroneous forces. This was especially apparent when calculating force direction during initial contact. However, the non-linear contact approach was found to predict more acceptable inter-object forces overall. For application to modelling large floating debris, however, there exists no comparative study into the effects of contact model. Stockstill et al. (2009) and others apply a linear contact model and achieve acceptable results for object motion.

For simplicity, a linear visco-elastic contact model is proposed in this work. As far fewer objects are simulated within the domain (< 200), any unrealistically large contact forces are unlikely to propagate far beyond the immediately contacting objects. Furthermore, as floating debris motion is primarily governed by hydraulic forces, these further prevent unrealistic contact forces from propagating.

Cundall and Strack (1979) include a Coulomb friction limiter in the tangential direction to account for energy loss due to sliding friction. For modelling floating debris, the inclusion of friction is necessary so as to model the 'clumping' effect when multiple objects travel as a large mass. In the approach presented by Cundall and Strack (1979), sliding occurs once the tangential force exceeds the static friction force. Cundall and

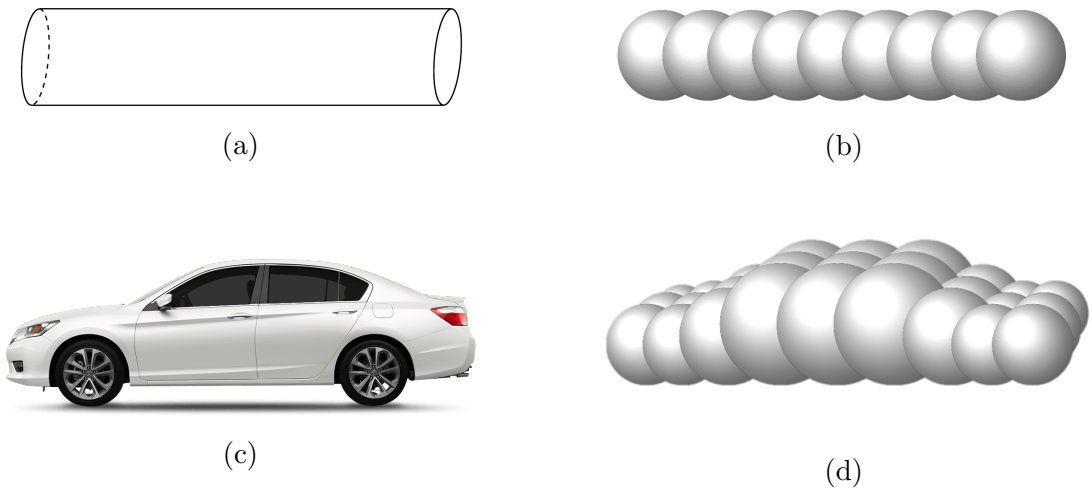

Figure 3.2: Examples of objects modelled using the multi-sphere method for shape representation

Strack (1979) treat sliding friction as a function of only the spring force, whereas others (Li et al., 2001; Ting et al., 1993) treat friction as a function of the total force including damping. For granular applications, a friction force proportional to spring and damping force components has been found to produce more realistic results under impact. In this work friction is calculated as a proportion of elastic and viscous contact forces.

In addition to local viscous damping, Cundall and Strack (1979) introduce a global damping term to the equations of motion. The term can be envisioned as a dash-pot connecting each sphere to the ground. Global damping acts on both translational and rotational velocity of an object and artificially simulates global energy loss. For example, an object accelerating through air will lose energy through drag. DEM featuring global damping simulates this energy loss, whereas without it an object will continue to accelerate until interrupted. Global damping is applicable where object displacement is large; and for objects travelling at high velocities within a viscous medium (Abbaspour-Fard, 2000). In this work global damping is negated for two reasons. First, to maintain consistency with the hydrodynamic scheme which assumes an inviscid liquid. Secondly because hydraulic forces limit the maximum velocity objects may reach. This process is explained in more detail through the model coupling procedures presented in Chapters 4 and 5.

Shape representation

Since its conception (Cundall and Strack, 1979) the discrete element method has seen numerous applications where element shape significantly affects object behaviour. Efforts to model more complex elements within DEM have improved simulation capability (Lin and Ng, 1997; Lu and McDowell, 2006) and extended application far beyond granular

materials.

There are two approaches for describing complex object shapes used within DEM: those where objects are considered as a single irregular element; and those where objects are built from multiple spherical elements (Markauskas et al., 2010). Previous coupled debris models (Stockstill et al., 2009) favour the first method. Treating objects as simplified regular polygons and polyhedra is computationally faster, as contact detection is performed for fewer elements overall. However, contact force calculation becomes more complex when non-spherical elements are considered as force direction, particularly at corners, is difficult to define (Feng and Owen 2004, Hopkins 2004).

The alternative approach is synonymously known as the multi-sphere method (Abbaspour-Fard, 2004), particle clumping (Šmilauer and al., 2015) and glued spheres (Hancock et al., 2009). Objects of any arbitrary shape can be approximated by affixing spheres to their interior, as illustrated in Figure 3.2. A similar approach is used widely in computer graphics design (Weller and Zachmann, 2009).

By representing objects as multiple spheres, force directions are uncomplicated to predict (Abbaspour-Fard, 2004). Modelling objects as conglomerates also ensures the numerical scheme is not limited in its applications and can be easily extended to model any object shape or size. Accuracy is dependent on the number of spheres used. A higher number of closely packed spheres results in better shape approximation but demands higher computation time to perform the necessary algorithms for each object sphere. Conversely, a lower sphere packing density results in faster computation time but may result in loss of accuracy. Packing density is controlled by sphere spacing Δs, which should be no greater than a single sphere's diameter, as illustrated in Figure 3.3. Figure 3.3a illustrates the maximum possible sphere spacing, whereas Figure 3.3b illustrates a sphere packing density that is twice as high.

3.2.2 Numerical modelling scheme

A discrete element modelling scheme has here been developed specifically for hydrodynamic coupling and is presented is this Chapter. Non-spherical axisymmetrical objects are simulated in space using the multi-sphere method for shape representation. Objects are represented in the $x - y$ plane with two translational degrees of freedom (DOF) and one rotational DOF (about the z axis). The modelling scheme employs a linear visco-elastic contact model with a tangential friction slider to simulate object 'clumping'. The scheme is applied using an object oriented programming approach written in the programming language C++.

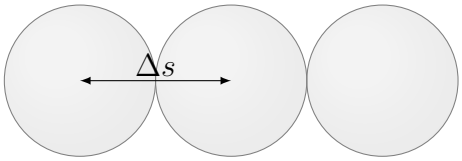

(a) $\Delta s = 2R$

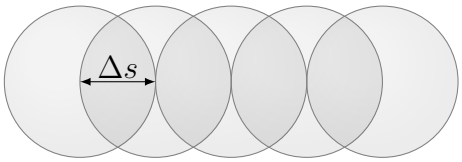

(b) $\Delta s = R$

Figure 3.3: Examples of objects modelled by rigidly joined spheres with spacing Δs.

Multi-sphere method for shape representation

The multi-sphere method is employed for its simplicity in calculating contact force directions. Objects within the discrete element scheme are represented by fixing spheres along a central axis. The number of spheres is directly proportional to the accuracy of the shape representation. Figure 3.3 shows two multisphere approximations of a cylindrical object, such as a log. In Figure 3.3a sphere centroids are spaced a diameter apart ($\Delta s = 2R$) and in Figure 3.3b the spacing is halved, ($\Delta s = R$). Figure 3.3b more accurately represents a cylinder, whereas Figure 3.3a contains fewer spheres so will achieve higher computational efficiency. Both sphere spacings of $\Delta s = R$ and $\Delta s = 2R$ are used in this work, the choice of spacing is selected prior to computation.

Multi-sphere object calculation

To manage multi-sphere objects within the computational domain, a local and global coordinate system is used. Objects are defined within the global coordinate system and have position vector $\boldsymbol{X}_{obj}$. Object-spheres are defined within both the global and a local coordiante system. The global position vector $\boldsymbol{X}_{sph}$ defines the distance from the domain origin ($\mathbf{O}$) to the sphere's centroid. The local position vector $\boldsymbol{x}_{sph}$ defines distance from the centroid of the parent object to the sphere. The global and local coordinate system for a cylinder consisting of three element spheres is illustrated in Figure 3.4. As an object translates and rotates the values stored in $\boldsymbol{x}_{sph}$ are adjusted while the magnitude of the local position vector ($|\boldsymbol{x}_{sph}|$) remains the same. This preserves object size, shape and rigidity.

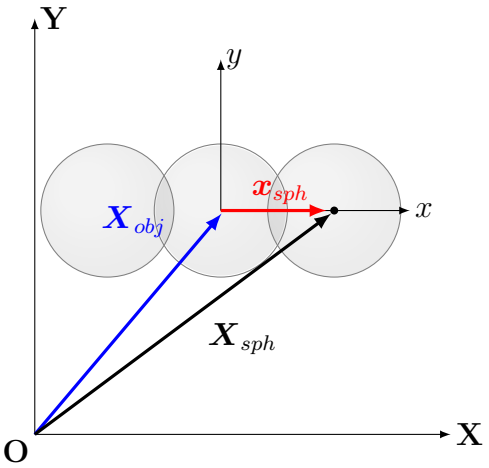

Figure 3.4: A multi-sphere object modelled within a global ($\boldsymbol{X}$) and local ($\boldsymbol{x}$) coordinate system.

Contact detection

The discrete element method predicts the contact mechanics of objects in collision. Object collision is determined according to a contact detection algorithm described here. Contact may only occur between element spheres belonging to different objects. Each sphere is therefore checked for contact against other spheres in the domain, excluding those belonging to the same object. During contact, spheres are permitted to overlap as illustrated in Figure 3.1. Within a single time step the magnitude of the overlap, Δn may not exceed the sum of the two particles radii, ($\Delta n \leq R_A + R_B$). A small enough time step should be selected to maintain this condition. The magnitude of the overlap between two spheres (denoted by the letters A and B) is calculated by:

$$\Delta n = (R_A + R_B) - ||\boldsymbol{X}_{sph(A)} - \boldsymbol{X}_{sph(B)}|| \tag{3.10}$$

The same approach is taken to detect contact between objects and the domain boundaries. For boundary contact, overlap is calculated by:

$$\Delta n = (R) - ||\boldsymbol{X}_{sph} - \boldsymbol{X}_{(boundary)}|| \tag{3.11}$$

Contact is deemed to have occurred when the distance between two sphere centroids is less than the sum of the two radii, or when the distance between a sphere centroid and a boundary is less that the sphere's radii (when $\Delta n < 0$). When contact is detected the inter-sphere contact forces are calculated.

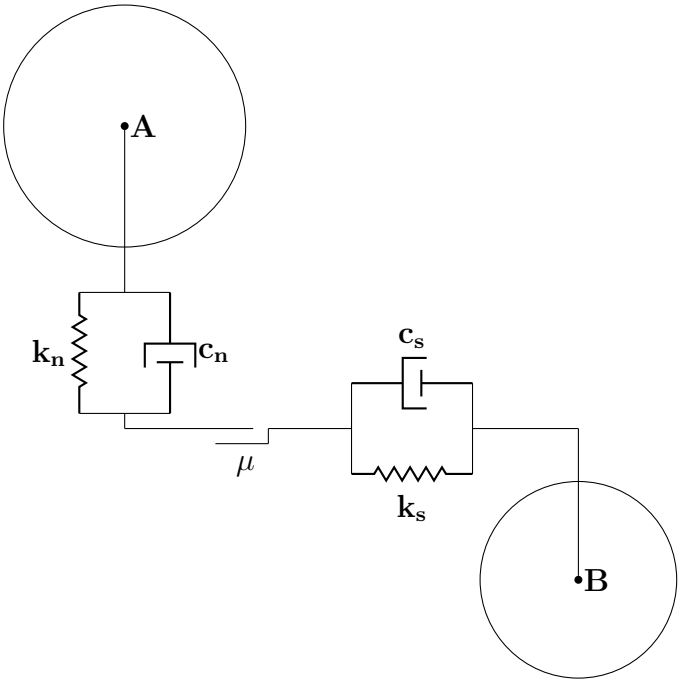

Figure 3.5: A visco-elastic contact model for two colliding spheres. It can be idealised as an elastic spring (k) and viscous dash-pot (c) connecting spheres in the normal (subscript n) and tangential (subscript s) directions. A friction slider (μ) inhibits sliding in the tangential direction.

Visco-elastic contact force calculation

A linear visco-elastic contact model is employed to predict the forces acting on colliding objects. The contact force model is illustrated by Figure 3.5. The chosen system predicts inter-sphere forces in the normal and tangential directions, these are denoted by the subscripts n and s respectively. The total forces in each direction are the sum of an elastic and viscous component, idealised as a spring and dash pot. In the tangential direction a frictional slider limits the magnitude of the total tangential force.

The force due to contact acting on a single sphere is the sum of both normal and tangential forces and is given by:

$$\mathbf{F}_{sph,c} = \sum \left(\mathbf{F}_n + \mathbf{F}_s \right) \tag{3.12}$$

where $\mathbf{F}_n$ and $\mathbf{F}_s$ are the normal and tangential force components. For each contact point N, the normal and tangential force increments, $\Delta F_n \hat{\mathbf{n}}$ and $\Delta F_s \hat{\mathbf{s}}$, are added to existing contact forces $(\mathbf{F}_n)_{N-1}$ and $(\mathbf{F}_s)_{N-1}$:

$$\mathbf{F}_n = (\mathbf{F}_n)_{N-1} + \Delta F_n \hat{\mathbf{n}} \tag{3.13}$$

$$\mathbf{F}_s = (\mathbf{F}_s)_{N-1} + \Delta F_s \hat{\mathbf{s}} \tag{3.14}$$

where $\hat{\mathbf{n}}$ is a unit vector projected in the normal direction from sphere A to sphere B. The unit vector $\hat{\mathbf{n}}$ is derived from the relative displacement vector ($\mathbf{n} = \boldsymbol{X}_{sph(A)} - \boldsymbol{X}_{sph(B)}$) and the magnitude of displacement between the centre points of spheres A and B, $||\mathbf{n}||$. The unit vector $\hat{\mathbf{s}}$ is a 90° rotation of the normal unit vector $\hat{\mathbf{n}}$ projected in the tangential direction. The normal and tangential unit vectors are given by:

$$\hat{\mathbf{n}} = \frac{\mathbf{n}}{||\mathbf{n}||} \tag{3.15}$$

$$\hat{\mathbf{s}} = \begin{bmatrix} \hat{n}_2 \\ -\hat{n}_1 \end{bmatrix} \tag{3.16}$$

The directionless force increments, ΔF_n and ΔF_s are calculated by:

$$\Delta F_n = -K_n \dot{n} \Delta t - C_n \dot{n} \tag{3.17}$$

$$\Delta F_s = -K_s \dot{s} \Delta t - C_s \dot{s} \tag{3.18}$$

where K_n, K_s, C_n and C_s are contact stiffness and damping coefficients illustrated in Figure 3.5. The scalars $\dot{n}$ and $\dot{s}$ are normal and tangential velocity components of the contact (where $\dot{n}\Delta t = \Delta n$).

$$\dot{n} = \dot{\boldsymbol{\upsilon}}_{A,B} \cdot \hat{\boldsymbol{n}} \tag{3.19}$$

$$\dot{s} = \dot{\boldsymbol{\upsilon}}_{A,B} \cdot \hat{\boldsymbol{s}} \tag{3.20}$$

where the relative velocity of contact between spheres A and B is given by the vector $\dot{\boldsymbol{\upsilon}}_{A,B}$. This is defined as:

$$\dot{\boldsymbol{\upsilon}}_{A,B} = (\dot{\boldsymbol{\upsilon}}_A - \dot{\boldsymbol{\upsilon}}_B) - (\dot{\theta_A} R_A + \dot{\theta_B} R_B)\hat{\mathbf{s}} \tag{3.21}$$

where $\dot{\theta}$ is rotational velocity and R is sphere radius. The magnitude of the tangential force is also checked against a Coulomb friction limiter ($F_{s(max)}$), which is proportional to the total normal force F_n and the contact friction coefficient μ:

$$|F_{s(max)}| = \mu F_n \tag{3.22}$$

The inclusion of tangential friction gives rise to a moment. In this work object rotation is only considered about the z axis to allow one degree of rotational freedom. Negating rotation about the x and y object axes simplifies computation and is here considered reasonable for applications where debris float on the water's surface. Rotation occurring about the x or y axis is likely to be minimal and have little effect on debris interaction. The moment acting on a sphere about its z axis is calculated by:

$$M_{sph} = (M_{sph})_{N-1} + \Delta F_s R \tag{3.23}$$

where M_{sph} is a scalar value.

Object force calculation

Within a single time interval, the contact forces acting on each sphere, Equation 3.12 are summed over each object to find the total object force, $\boldsymbol{F}_{obj}$. The total object moment, M_{obj} acts about the z axis through the objects centroid and is the sum of the moment acting on each sphere, and the moment due to sphere forces displaced from the object centroid:

$$\boldsymbol{F}_{obj} = \sum_{i=0}^{no.spheres} \boldsymbol{F}_{sph,c} \tag{3.24}$$

$$M_{obj} = \sum_{i=0}^{no.spheres} M_{sph} + (\boldsymbol{F}_{sph,c} \times \boldsymbol{x}_{sph}) \tag{3.25}$$

where $\boldsymbol{x}_{sph}$ is the local position vector of sphere relative to the object centroid as illustrated previously in Figure 3.4.

Translational and rotational motion calculation

Translational and rotational acceleration ($\ddot{\boldsymbol{X}}_{obj}$ and α_{obj}) are calculated in accordance with Newton's second law.

$$\ddot{\boldsymbol{X}}_{obj} = \frac{\boldsymbol{F}_{obj}}{m_{obj}} + g \tag{3.26}$$

$$\alpha_{obj} = \frac{M_{obj}}{I_{obj}} \tag{3.27}$$

where m_{obj} and I_{obj} are the object mass and moment of inertia. A central differencing time integration scheme (Cundall and Strack, 1979) yields object velocities ($(\dot{\boldsymbol{X}}_{obj})_{t+\frac{1}{2}}$,

$(\omega_{obj})_{t+\frac{1}{2}}$) and positions ($(\boldsymbol{X}_{obj})_{t+1}$, $(\theta_{obj})_{N+1}$) at the new time step:

$$(\dot{\boldsymbol{X}}_{obj})_{t+\frac{1}{2}} = (\dot{\boldsymbol{X}}_{obj})_{t-\frac{1}{2}} + \ddot{\boldsymbol{X}}_{obj}\Delta t \tag{3.28}$$

$$(\omega_{obj})_{t+\frac{1}{2}} = (\omega_{obj})_{t-\frac{1}{2}} + \alpha_{obj}\Delta t \tag{3.29}$$

$$(\boldsymbol{X}_{obj})_{t+1} = (\boldsymbol{X}_{obj})_{t} + (\dot{\boldsymbol{X}}_{obj})_{t+\frac{1}{2}}\Delta t \tag{3.30}$$

$$(\theta_{obj})_{t+1} = (\theta_{obj})_{t} + (\omega_{obj})_{t+\frac{1}{2}}\Delta t \tag{3.31}$$

Updating sphere position

The local position of each sphere within an object is updated through the rotation matrix $R_y(\theta)$ in Equation 3.32 yielding the new local position vector $(\boldsymbol{x}_{sph})_{t+1}$ through Equation 3.33.

$$R_(\theta) = \begin{bmatrix} \cos\theta & 0 & \sin\theta \\ 0 & 1 & 0 \\ -\sin\theta & 0 & \cos\theta \end{bmatrix} \tag{3.32}$$

$$(\boldsymbol{x}_{sph})_{t+1} = (\boldsymbol{x}_{sph})_{t} \begin{bmatrix} \cos\theta_{obj} & 0 & \sin\theta_{obj} \\ 0 & 1 & 0 \\ -\sin\theta_{obj} & 0 & \cos\theta_{obj} \end{bmatrix} \tag{3.33}$$

The sphere's new coordinates are then defined in the global coordinate system according to Equation 3.34.

$$(\boldsymbol{X}_{sph})_{t+1} = (\boldsymbol{X}_{obj})_{t+1} + (\boldsymbol{x}_{sph})_{t+1} \tag{3.34}$$

3.2.3 Numerical stability

The central differencing time integration used for translational and rotational advancement is only conditionally stable and requires selection of a suitable time step. Alternative implicit time integration schemes overcome this limitation, but are computationally expensive (O'Sullivan and Bray, 2003). Instead the time step (Δt) should be less than the critical time step (Δt_c).

A critical time step first proposed by Cundall and Strack (1979) in Equation 3.35 is suitable for systems with a single degree of freedom (1DOF) and linearly elastic contact.

The critical time step in Equation 3.35 is applied in this work for unidirectional object translation and is related to mass (m) and stiffness (k).

$$\Delta t_c = 2\sqrt{\frac{m}{k}} \tag{3.35}$$

For a linearly configured arrangement of disks with two translational DOFs and one rotational DOF, O'Sullivan and Bray (2003) suggests the critical time step in Equation 3.36. The critical time step in Equation 3.36 is applied in this work for applications where objects translate in the x and y directions and rotate about the z axis.

$$\Delta t_c = \sqrt{\frac{1}{2}}\sqrt{\frac{m}{k}} \tag{3.36}$$

3.2.4 Object oriented programming in C++

Two main programming approaches exist; procedural and object-oriented (OO). Procedural programming divides a program into a series of actions or functions that are executed sequentially, whereas OO programming divides a program into objects that contain data and functionality. Balevičius et al. (2006) assessed the computational efficiency of DEM software based on both approaches and found that the procedural approach achieved shorter computational time than the OO approach. However, Peters and Dziugys (2002) reported that an OO approach achieves a high degree of flexibility and extendability through the reduction of a complex system into flexible modules. OO programming is well suited to discrete element systems (Peters and Dziugys, 2002). In this work, flexibility and extendability is considered key to enabling hydrodynamic coupling therefore an OO approach is favoured. The approach has a number of additional functionalities that lend it well to the discrete element method:

- **Class structure** - In OO programming a class is defined as a template for a specific type of object and contains the variables and functionality of that object type. Objects are instances of a class and contain actual values corresponding to class variables. For application to the discrete element method a template for floating objects is defined by `Class:Objects`, illustrated by Figure 3.6. Instances of `Class:Objects` refer to specific objects such as vehicles, tree trunks and branches.

- **Encapsulation** - Encapsulation binds the data and methods relating to an object together into a single class. For example, within `Class:Object`, object properties such as mass, density and dimensions are stored. This enables a complex system of many variables and functions to be reduced to a modular system. This improves the

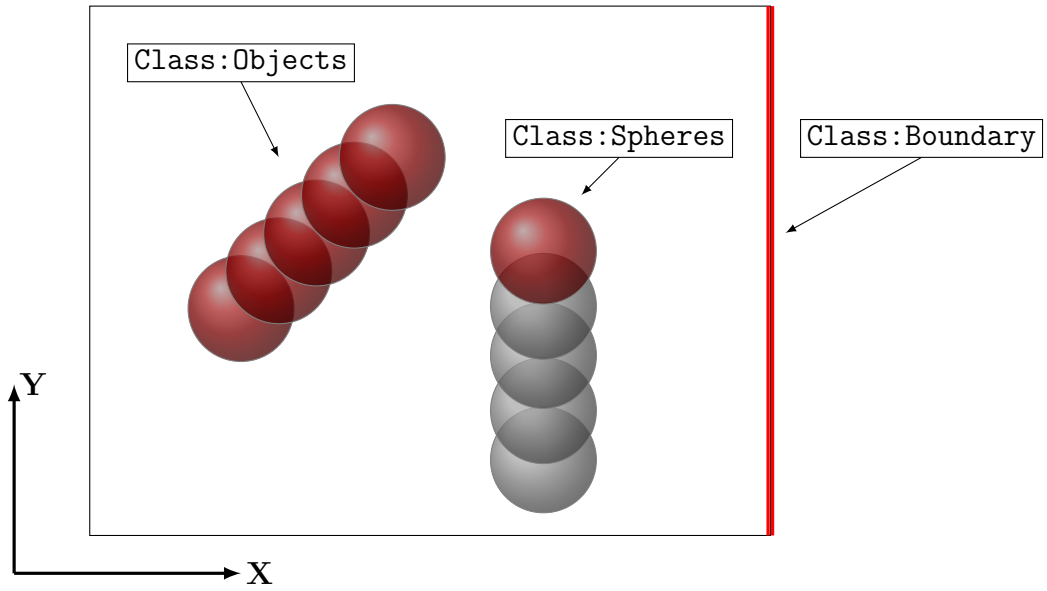

Figure 3.6: Diagram showing a simplified visualisation of the class system employed by object oriented DEM code.

extendability of the DEM scheme as new modules can be added without needing to access or alter existing modules. For a DEM scheme aimed at model coupling this enables additional subroutines to be easily added at a later stage.

- **Inheritance** - Inheritance through a hierarchical class structure is a useful feature of OO programming, particularly when applied to the multi-sphere method for shape representation (presented in Section 3.2.2). As well as classes, subclasses are defined that inherit some variables and functionality from their parent class. When applied to the multisphere method, the `Class:Object` contains the subclass, `Class:Spheres`. This enables object spheres to inherit necessary properties from the object to which they belong.

In this work, a discrete element system is developed using an OO approach and implemented through the programming language C++. Programming in C++ enables model compatibility with hydrodynamic schemes implemented in C++ and CUDA programming languages. Figure 3.6 illustrates a simplified version of the DEM class structure developed here.

3.2.5 Analytical verification of the discrete element scheme

The contact model employed in this discrete element scheme has been verified against analytical solutions for two idealised test cases that solve 1D object translation resulting

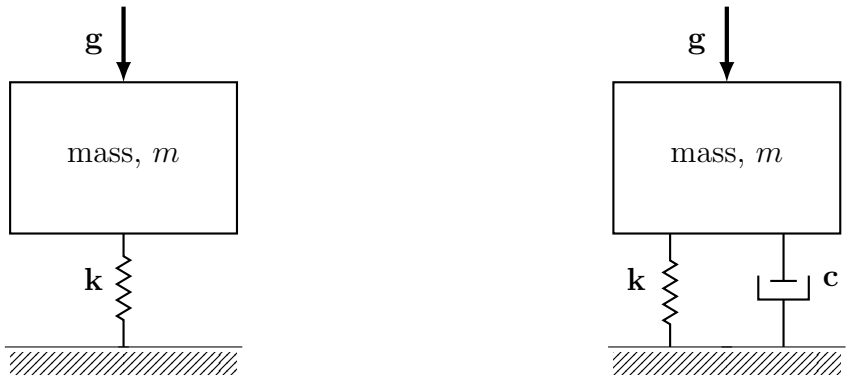

(a) Linear spring (b) Linear spring and viscous dash-pot

Figure 3.7: Mass-spring systems derived from vibration theory (Thompson, 1966).

from contact. The solutions are derived from vibration theory and can be idealised as the mass spring systems shown in Figure 3.7. Translational object motion for a purely elastic normal contact (Figure 3.7a) and a visco-elastic normal contact (Figure 3.7b) are simulated. An additional analytical solution is sought to verify rotational motion of an axisymetrical object under an instantaneous, oblique force.

Case 1 - free fall of a ball with elastic contact

The first verification problem was presented by Chen et al. (2007) and solves the free fall, contact and rebound of a ball. The ball is dropped from height y_0 onto a horizontal surface. Rebound is entirely elastic, therefore no energy loss is incurred. The contact stage is idealised as the mass-spring vibrating system shown in Figure 3.7a. The duration of contact is dictated by contact stiffness k, which for a 1D contact is equal to normal stiffness k_n. To solve the analytical solution, the test case is split into three stages; an initial free fall stage, contact with a solid boundary, and the final rebound stage.

- **Free fall stage**

Between its initial position (y_0) and contact with the boundary ($y - r_s = y_b$) the ball is in free fall and is described by the motion integrals:

$$\ddot{y} = g \tag{3.37}$$

$$\dot{y} = \int \ddot{y} dt = gt \tag{3.38}$$

$$y = \int \dot{y} dt = \frac{1}{2} g t^2 \tag{3.39}$$

where y is the vertical position of the ball's centroid above the horizontal boundary at $y = 0$. Air resistance is neglected as the balls initial displacement y_0 is small.

- **Contact stage**

The contact stage is treated as a mass-spring problem and the equation for the ball's acceleration is obtained from vibration theory (Thompson, 1966).

$$\ddot{y} + \left[g - \frac{k}{m}(r - y) \right] = 0 \tag{3.40}$$

where the initial conditions are: $y_{t=0} = y_0$ and $\dot{y}_{t=0} = -\sqrt{2g(y_0 - r)}$. Chen et al. (2007) provide a closed form solution of the above differential equation for y.

$$y = -\sqrt{2g(y_0 - r)}\sqrt{\frac{m}{k}} \sin\left(\sqrt{\frac{k}{m}}t\right) + \frac{mg}{k}\cos\left(\sqrt{\frac{k}{m}}t\right) + \left(r - \frac{mg}{k}\right) \tag{3.41}$$

- **Rebound stage**

Chen et al. (2007) describes the sphere's rebound as the exact opposite of the free fall stage with initial conditions: $y_{tr=0} = r$ and $\dot{y}_{tr=0} = \sqrt{2g(y_0 - r)}$.

$$\ddot{y} = -g \tag{3.42}$$

$$\dot{y} = \dot{y}_{tr=0} + \int \ddot{y}dt = \sqrt{2g(y_0 - r)} - gt \tag{3.43}$$

$$y = y_{tr=0} \int \dot{y}dt = r + \sqrt{2g(y_0 - r)}t + \frac{1}{2}gt^2 \tag{3.44}$$

Case 2 - free fall of a ball with viscous damping

Chen et al. (2007) also presented a case for the free fall of a ball with viscous damping. This is presented as a mass-spring-damping problem and the governing differential equation can again be derived from the theory of vibration. A viscous damping term is introduced to the contact stage with equations of motion for the free fall stage remaining unchanged. The normal damping term ($c = c_n$) is derived as a fraction (ζ) of the critical damping term (c_{crit}).

$$c = \zeta c_{crit} \tag{3.45}$$

where $\zeta = \frac{c}{c_{crit}}$ is the damping ratio. The critical damping term is a function of contact

stiffness k.

$$c_{crit} = 2\sqrt{mk} \tag{3.46}$$

- **Free fall stage**

The equations of motion for the free fall stage are the same as in the un-damped case (Equation 3.37, 3.38 and 3.39).

- **Contact stage**

Under viscous damping the contact stage is treated as the mass-spring-damper problem illustrated in Figure 3.7b and is described by the differential equation:

$$\ddot{y} - \left[k(r-y) + mg - c\dot{y}\right] = 0 \tag{3.47}$$

where the initial conditions equal those presented earlier for the un-damped case. Chen et al. (2007) provides a general closed form solution for the governing differential equation:

$$\begin{aligned} y = &-\frac{1}{2}\frac{exp\left(-\frac{(c-\sqrt{c^2-4km}t}{2m}\right)m(\sqrt{c^2-4km}(-gc-2k\sqrt{2g(y_0-r)})-gc^2+4mgk)}{k(4km-c^2)} \\ &-\frac{1}{2}\frac{exp\left(-\frac{(c+\sqrt{c^2-4km}t}{2m}\right)m(\sqrt{c^2-4km}(gc+2k\sqrt{2g(y_0-r)})-gc^2+4mgk)}{kc(4km-c^2)} \\ &+\left(r+\frac{mg}{k}\right) \end{aligned} \tag{3.48}$$

The term $\sqrt{c^2-4km}$ plays an important role in the above solution. If damping is critical ($c = c_{crit}, \zeta = 0$) then $\sqrt{c^2-4km} = 0$ and sphere's displacement will decay rapidly to 0. If $c > c_{crit}, \zeta > 1$, $\sqrt{c^2-4km}$ is positive and real, the system is said to be over-damped and displacement exponentially decays towards zero. If $c < c_{crit}, \zeta < 1$ the system is said to be under damped. The term $\sqrt{c^2-4km}$ is a complex number and displacement has an oscillatory response which diminishes towards zero. Here an under-damped system has been reproduced where $\zeta < 1$. With initial conditions $y_{t=0} = 0$ and $\dot{y}_{t=0} = 0$ the exact solution for ball displacement is:

$$y = r + \exp\left(-\zeta\sqrt{\frac{k}{m}}t\right)\left(\left(\frac{\sqrt{2g(y_0-r)}}{\sqrt{\frac{k}{m}}\sqrt{|\zeta^2-1|}}\right)\sin\left(\sqrt{\frac{k}{m}}\sqrt{|\zeta^2-1|}t\right)\right) \tag{3.49}$$

- **Rebound stage**

Viscous damping does not affect rebound so the equations of motion are the same as in the previous example with the initial position $y_{t=0} = r$. The initial velocity for rebound is given by:

$$\dot{y} = \frac{\left(\sqrt{2g(y_0 - r}\exp\left(\zeta\sqrt{\frac{k}{m}}t\right)\left(\sqrt{\frac{k}{m}}\sqrt{|\zeta^2-1|}\right)\cos\left(\sqrt{\frac{k}{m}}\sqrt{|\zeta^2-1|}t\right)\right)}{\sqrt{\frac{k}{m}}\sqrt{|\zeta^2-1|}} \\ \frac{-\zeta\sqrt{\frac{k}{m}}\sin\left(\sqrt{\frac{k}{m}}\sqrt{|\zeta^2-1|}t\right)}{\sqrt{\frac{k}{m}}\sqrt{|\zeta^2-1|}} \tag{3.50}$$

Case 3 - rotation of an object due to instantaneous force

When modelling non-spherical objects, rotational motion becomes an important process affecting overall transport. The following idealised test case is presented by Abbaspour-Fard (2004) for an instantaneous, oblique force acting on a multi-sphere object. Here a solution is derived for the rotational motion of a cylindrical object. A cylinder of length l(m), diameter $d(m)$ and mass moment of inertia I (kg.m^2) is suspended in space, with no gravitational force acting upon it. An instantaneous point load, F(N) is applied to the cylinder at a horizontal distance, x'(m) from its centroid. The force is applied for the duration of one time step, Δt(s) and then removed.

- **Initial acceleration**

The initial angular acceleration of the object is calculated according to Newton's second law of motion:

$$a = \frac{F}{m} \tag{3.51}$$

$$\alpha = \frac{M}{I} \tag{3.52}$$

where a is acceleration, α is angular acceleration, F is object force and M is moment about the centroid and is calculated by:

$$M = Fx' \tag{3.53}$$

Because the force, F is applied instantaneously, the objects velocity reaches its maximum within the first time step. Therefore for the first time step:

$$v = v_0 + a\Delta t \tag{3.54}$$

$$\omega = \omega_0 + \alpha\Delta t \tag{3.55}$$

where v is velocity and ω is rotational velocity.

- **Perpetual motion**

After the duration of the initial time step, no external forces are applied to the object, therefore velocity (v) remains constant and the object remains in perpetual rotation with angular velocity ω. Object position (x) and rotation about its centroid (θ) are described by:

$$x = x_0 + vt \tag{3.56}$$

$$\theta = \theta_0 + \omega t \tag{3.57}$$

where x_0 and θ_0 are the object's initial position and orientation.

3.2.6 Comparison of analytical and numerical results

The analytical solutions to the test cases described above have been compared to numerical results produced using the discrete element modelling scheme introduced in this chapter. The results are presented here. For test cases one and two, balls are represented by a single sphere. The physical properties of the sphere and experimental parameters for the first two tests cases are provided in Table 3.1. In both cases a sphere of radius $0.01m$ and density $500kg/m^3$ is initialised 0.5m above a solid horizontal boundary. For the first case, a purely elastic contact is modelled ($c_n = 0.0$). For the second case local contact damping is applied.

Physical properties

Sphere property	Test case 1	Test case 2
Radius, r	$0.01m$	$0.01m$
Density, ρ	$500kg/m^3$	$500kg/m^3$
Spring stiffness, k	$100,000N/m$	$100,000N/m$
Damping coefficinet, c	$0N/m$	$348N/m$
Initial displacement, y_0	$0.5m$	$0.5m$
Initial velocity, $\dot{y}_0$	$0.0m/s$	$0.0m/s$

Table 3.1: Physical properties of analytical validation problems 1 and 2

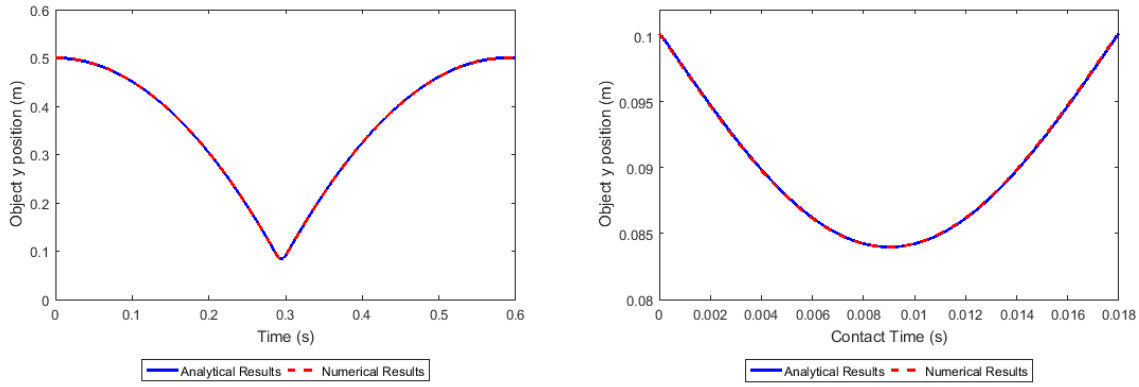

(a) Ball displacement for total simulation time. (b) Ball displacement for contact duration.

Figure 3.8: Analytical test case 1: comparison between numerical and analytical results for object position on the vertical axis.

Analytical test case 1 - un-damped elastic contact

The discrete element modelling scheme is used to predict the displacement of a solid ball rebounding off a horizontal boundary. The numerical results are compared to the analytical solution described previously. In this test case an elastic contact model is tested. A time step of 0.0001 seconds is selected. Figure 3.8 presents the analytical and numerical results. Figure 3.8a shows the displacement of the ball from its initial position. After 0.28 seconds the ball makes contact with the solid boundary. The ball is considered in contact when $y \leq r$. Figure 3.8b shows the ball's displacement for the duration of the contact, which lasted 0.018 seconds. As no damping is applied in this test case, the ball returns to its original position after 0.6 seconds. With continued simulation the ball will continue to bounce indefinitely. Compared to the analytical solution, the numerical model performs well, no discernible difference is obvious between numerical and analytical solutions presented in Figure 3.8.

Analytical test case 2 - damped elastic contact

In this test case a damping parameter of $\zeta = 0.3$ is selected, resulting in a damping coefficient of $348 N/m$ that is introduced to the analytical set-up described previously. Figure 3.9 shows a comparison between numerical and analytical results. From its initial position of 0.5m the ball falls with a constant acceleration equal to gravity. After 0.28 seconds the ball makes contact with the solid horizontal boundary. Contact lasts 0.0188 seconds (Figure 3.9b). At the end of contact, the ball rebounds to a height of 0.16m above the solid boundary. Compared to the analytical solution, the numerical model performs

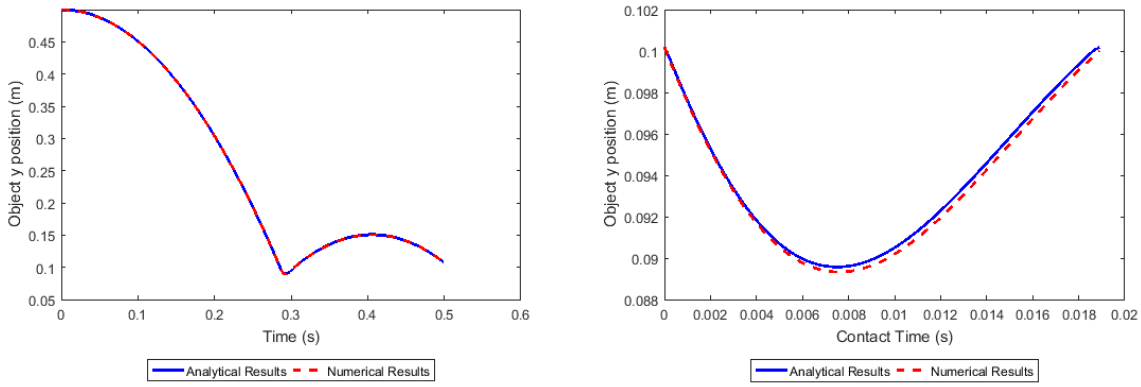

(a) Ball displacement for total simulation time. (b) Ball displacement for contact duration.

Figure 3.9: Analytical test case 2: comparison between numerical and analytical results for object position on the vertical axis.

reasonably well. It slightly underestimates the position of the ball after rebound but is still very similar.

Analytical test case 3 - rotation due to an instantaneous force

Physical properties

Object property	Test case 3
Radius, r	$0.01m$
Length, l	$0.1m$
Density, ρ	$800kg/m^2$
Mass, m	$0.025kg$
Mass moment of inertia, I	$0.000125kg.m^2$
Initial velocity, $\dot{y}_0$	$0.0m/s$

Table 3.2: Physical properties of analytical validation problem 3

In this test case the discrete element method is used to predict the translation and rotation of a cylindrical object after the application of an instantaneous eccentric force. The physical properties of the cylinder are described in Table 3.2. Within the discrete element method the cylinder is modelled as nine spheres with sphere diameters equal to the cylinder diameter and spheres rigidly fixed along the cylinder axis. The spheres have a spacing between their centroids equal to the object radius ($\Delta s = R$). A force of $0.5kN$ is applied to the cylinder at a distance $x' = 0.02m$ from its centroid, for the duration of one time step ($\Delta t = 0.0001$) after which the force is removed. During the first time step of the simulation the analytical and numerical schemes both solve translational and

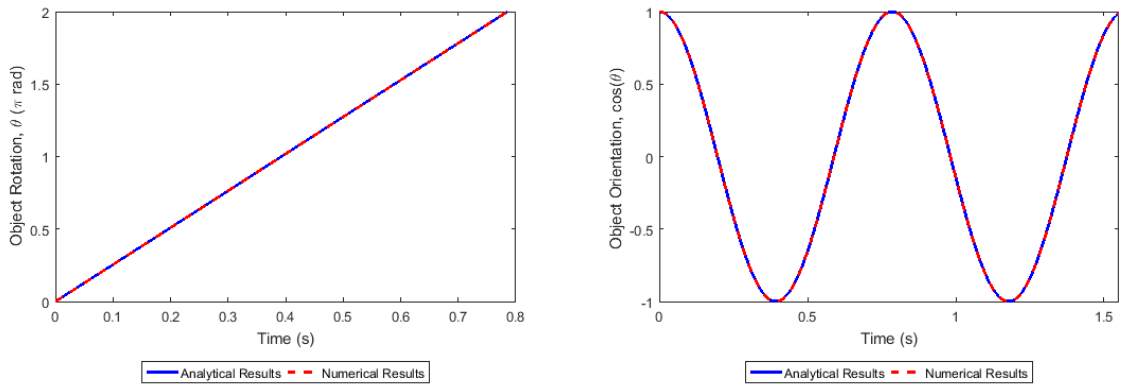

(a) Cumulative object rotation for total simulation time.

(b) Object orientation for total simulation time.

Figure 3.10: Test Case 3: comparison between numerical and analytical results for object rotation and object orientation.

rotational accelerations of :

$$a = 20000 m/s^2$$

$$\alpha = 80000 rad/s^2$$

After the initial time step both the analytical and numerical schemes solve constant translational and rotational velocities of:

$$v = 2.0 m/s$$

$$\omega = 8.0 rad/s$$

Figure 3.10 shows a comparison between numerical and analytical results for object orientation and cumulative rotation. Figure 3.10a shows the cumulative rotation of the object in radians and Figure 3.10b shows the object's orientation with respect to time, given by $cos(\theta)$. The discrete element method developed here makes accurate predictions of the analytical solution given the time step $\Delta t = 0.0001$ seconds. No discernible difference is observed between numerical and analytical results.

3.3 Assumptions and limitations

There are a number of assumptions and limitations associated with the DEM developed here. The DEM predicts translation with 2DOF and rotation with 1DOF, therefore object position in the z direction is assumed to be unchanging, and any rotation about the x and y axes is negated. When considered in the context of floating debris, it is reasonable to simplify rotation to 1DOF. It is within this plane that rotation has the most significant effect on debris motion and blockage. However, a floating object is likely to undergo considerable vertical translation, especially during initial floating. Debris position in the z axis will therefore be addressed further in Chapters 4 and 5, where the hydraulic coupling procedure is used to account for vertical displacement.

3.4 Conclusion

This chapter has described the numerical methods that provide the basis of a new numerical modelling tool aimed at simulating the transport dynamics of floating objects when mobilised by flash flooding. Two numerical approaches have been presented. The first is a finite volume Godunov-type hydrodynamic scheme that solves a system of 1D or 2D PDEs describing fluid flow. Notably, the hydrodynamic scheme is shock capturing and therfore highly suited to modelling flash flood events. The hydrodynamic scheme was developed by researchers at Newcastle University and has already been extensively validated. Also presented is the discrete element method (DEM) which forms the other constituent part of the new floating debris modelling tool developed in this work. A new piece of DEM code has been developed here which is computationally suited for coupling with the hydrodynamic scheme presented previously. The discrete element scheme is written using the programming language C++ and employs the multi-sphere method for shape representation. This enables any shape of object to be easily modelled. The discrete element scheme developed here has been validated for three analytical test cases and performs to an acceptable level of accuracy in each.

Chapter 4

Modelling floating debris transport in 1D

This chapter presents a new 1D numerical modelling tool for simulating floating debris transport that couples a 1D finite volume Godunov-type hydrodynamic scheme with the discrete element method. A detailed description of these numerical methods has been provided in Chapter 3. The new floating debris modelling tool, presented here, predicts the transport dynamics of spherical and cylindrical shaped floating objects in unidirectional flow and is applicable to singular debris transport in an approximately uniform channel. In this chapter, the 1D coupling procedure and accompanying force derivation are described. The numerical methods are verified against an analytical solution to the equations of motion for the idealised transport of a sphere in steady, uniform flow. Experimental investigations are presented for objects transported under dam break conditions in a hydraulic flume. These results enable a better understanding of the physics governing debris transport. Finally, the new 1D floating debris modelling tool is applied to five experimental test cases. Model predictions of water depth and object position are validated against experimental results.

4.1 A force-balanced hydraulic coupling procedure

Intrinsic to the discrete element scheme described in Chapter 3 are forced object interactions governed by Newtonian mechanics. It follows, therefore that hydrodynamic coupling may be achieved through the application of hydraulic forces to objects in contact with fluid flow. These hydraulic forces are derived from the fluid momentum principal so as to be consistent with the governing 1D St.Venant equations (Equation 3.5 and 3.6). According to Newtonian mechanics, an equal and opposite force is also experienced by the

contacting fluid. This counter hydraulic force generates a reduction in flow velocity and increase in stage, thus realising the backwater effects of a blockage. Here force balanced coupling is achieved by applying an equal and opposite object force to fluid cells through the hydrodynamic source terms in Equation 3.5.

4.1.1 Hydraulic force calculation

Liang et al. (2016) derived the force and pressure components acting at a fluid cross section, according to momentum principal. Their derivation is applied in this work to determine the hydraulic force components acting on a floating object. Considering open channel flow, the total force at any fluid cross section can be decomposed into a force due to hydrostatic pressure (P) and a hydrodynamic force due to momentum transfer. The hydrodynamic force is typically given by the fluid momentum at its cross section: $\rho_w QU$, where ρ_w is fluid density, Q is discharge through the cross section and U is the average velocity (Liang et al., 2016). At a given cross section, the total fluid force ($F_{c.s}$) is therefore:

$$F_{c.s} = P + \rho_w QU \tag{4.1}$$

Dividing both sides of Equation 4.1 by the cross section area A, yields the total average fluid pressure. For a rectangular cross section this is given by:

$$\bar{f} = \bar{p_s} + \bar{p_d} = \rho_w g\bar{h} + \rho_w U^2 \tag{4.2}$$

where $\bar{p_s}$ and $\bar{p_d}$ are the hydrostatic and hydrodynamic pressure components and $\bar{h}$ is water depth to the centroid of the submerged face. For the total average pressure acting horizontally on a floating sphere, Equation 4.2 becomes:

$$\bar{f} = \bar{p_s} + \bar{p_d} = \bar{p_s} + \rho_w {U^*}^2 \tag{4.3}$$

where $U^* = U - \dot{x}$; U is the depth averaged fluid velocity and $\dot{x}$ is horizontal velocity of the floating object. Under a hydrostatic pressure distribution, the hydrodynamic pressure component acts uniformly over the submerged depth of an object. The hydrostatic pressure component, however varies linearly with depth, from 0 at the water's surface to its maximum at the base of the submerged object.

Calculating relative to the centroid of a submerged sphere, the total average hydrostatic pressure can be described by the integral:

$$\bar{p_s} = \rho g \int d - z dz \tag{4.4}$$

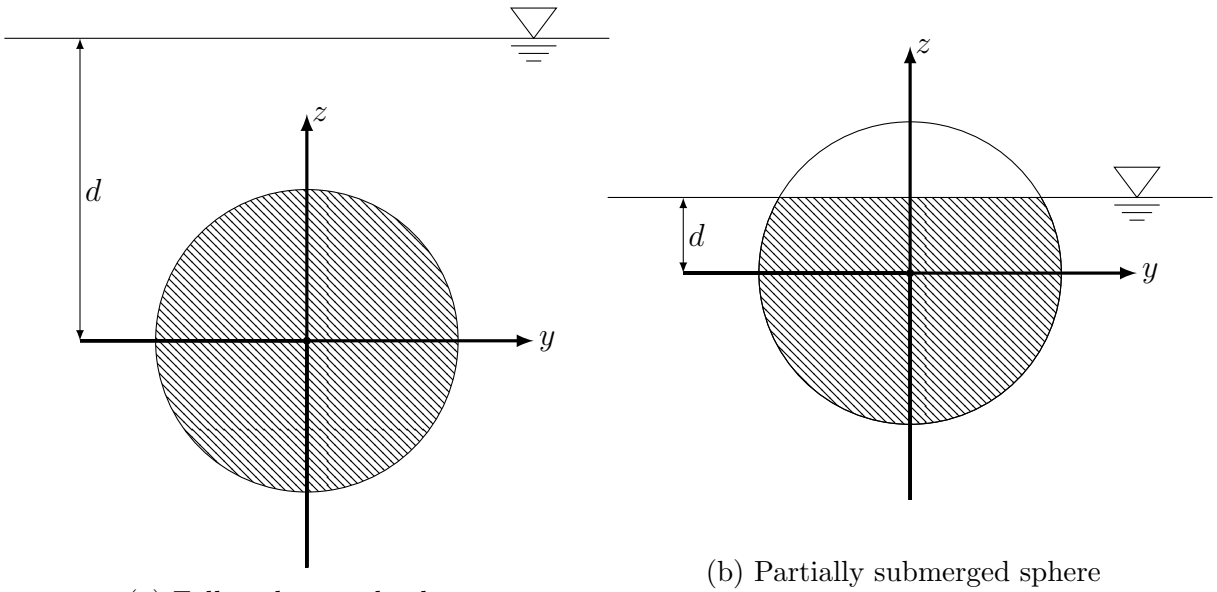

(a) Fully submerged sphere

(b) Partially submerged sphere

Figure 4.1: Hydrostatic force derivation diagram for fully and partially submerged spheres.

where d is water depth relative to the centroid of the sphere. Equation 4.3 then becomes:

$$\bar{f} = \rho_w U^{*^2} + \rho g \int d - z dz \tag{4.5}$$

Applying the pressure components over the projected horizontal area of the submerged portion of a floating sphere (A_{sub}) yields the total hydraulic force F_h, given by:

$$F_h = f_s + f_d = \bar{p_s} A_{sub} + \bar{p_d} A_{sub} \tag{4.6}$$

The projected submerged area (A_{sub}) is described by the integral:

$$A_{sub} = 2 \int \sqrt{R^2 - z^2} dz \tag{4.7}$$

where R is the radius of the sphere. Therefore total hydrostatic and hydrodynamic force components acting on a partially or fully submerged sphere may be described by:

$$\bar{p_s} A_{sub} = 2\rho_w g \int \Big(d - z\Big) \sqrt{R^2 - z^2} dz \tag{4.8}$$

$$\bar{p_d} A_{sub} = 2\rho_w U^{*^2} \int \sqrt{R^2 - z^2} dz \tag{4.9}$$

Equation 4.8 and 4.9 are solved for upper and lower limits of z relative to the centroid of the sphere. For a fully submerged sphere the upper limit is R and the lower limit is

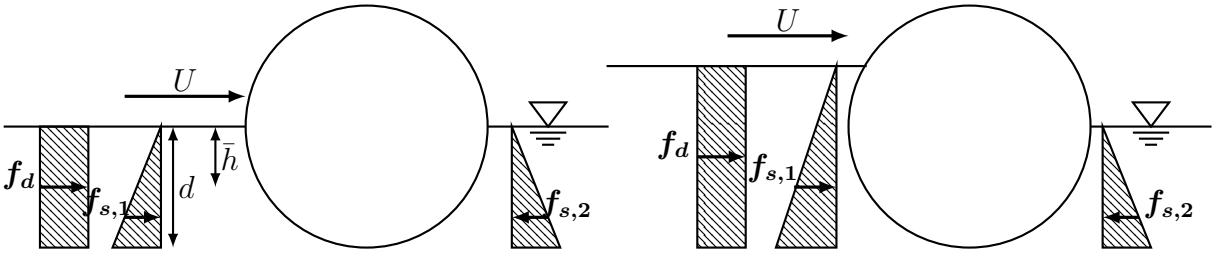

(a) Hydrostatic equilibrium. (b) Unequal hydrostatic forces.

Figure 4.2: 1D Hydraulic force combinations acting on a floating sphere.

$-R$. For a partially submerged sphere the upper and lower limits are d and $-R$.

Equation 4.6 is applied at the upstream and downstream boundaries of the sphere as illustrated for a single sphere in Figure 4.2. The hydrodynamic force component, f_d acts only in the direction of fluid velocity and is therefore only applied to the flow facing side of the object. The hydrostatic component f_s is applied in both the upstream and downstream directions.

As Figure 4.2 illustrates, the actual point of action of the hydrostatic and hydrodynamic force components are offset from the centre of the object, however through the discrete element method, all forces are applied directly through the sphere's centre. Using this method there is no resulting momentum due to fluid affecting individual spheres.

Under uniform flow conditions, illustrated by Figure 4.2a, a floating object is considered in hydrostatic equilibrium, $f_{s,1} = f_{s,2}$. Only the hydrodynamic force contributes to the resultant load. However, when the upstream and downstream water depths differ, as in Figure 4.2b, the hydrostatic force becomes influential. Such a scenario is expected to occur during surge type conditions that result in differing water depths upstream and downstream of an object. Likewise, when debris becomes blocked at structures, backwater effects will exert a hydrostatic pressure on the upstream face that is not equated in the downstream.

Vertical forces

In the presented scheme, objects are transported with a single degree of translation in the horizontal direction. This is dictated by the horizontal hydraulic forces in Equation 4.6. However it is also necessary to determine an object's position on the vertical axis in order to calculate values for submerged horizontal area (A_{sub}) and depth to submerged centroid (d). An object floats due to the effects of buoyancy. According to Archimides

principal, the buoyant force acting on a floating object is positive and given by:

$$F_b = \rho_w g V_{sub} \tag{4.10}$$

where V_{sub} is the submerged volume of the floating object. The buoyant force is opposed by a negative force, F_w equal to the weight of the object:

$$F_w = \rho_{obj} g V_{obj} \tag{4.11}$$

where ρ_{obj} is the object density, and V_{obj} is the total volume of the object. The governing St. Venant equations assume a hydrostatic vertical velocity profile and therefore assume no hydrodynamic force due to fluid velocity. However if an object moves in the vertical direction, for example when floating upwards towards the water's surface the relative velocity of the static fluid column to the moving sphere exerts a hydrodynamic force opposing the direction of travel. The problem becomes more complex when the object penetrates the water's surface. Surface tension inhibits an object from breaking the water surface and surface waves act to dampen the oscillatory response of an object bobbing vertically. The vertical displacement of a floating object through a column of liquid is therefore a complex problem requiring the analysis of many opposing forces. Calculating the vertical position of a floating object by assessing all of these forces would prove complex and computationally costly. The actual vertical forces are considered to have little effect on object translational motion.

Instead, an alternative, simplified approach for predicting object vertical position is suggested here. Consider a floating sphere in static equilibrium, as illustrated in Figure 4.3. With zero vertical displacement only two vertical forces act on the sphere; a buoyant force (Equation 4.10) and force due to gravity (Equation 4.11). If, at each time interval the sphere is assumed to be in static equilibrium, the submerged volume (V_{sub}) and subsequently A_{sub} and d may be found directly by equating the buoyant and gravitational forces. In equilibrium the submerged volume of a floating sphere is given by:

$$V_{sub} = \frac{\rho_{obj} V_{obj}}{\rho_w} \tag{4.12}$$

In the modelling scheme presented here the vertical position of the object at each time step is estimated explicitly using Equation 4.12.

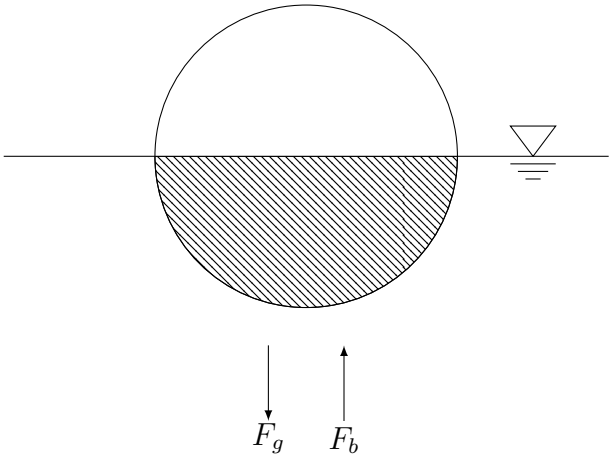

Figure 4.3: Vertical forces acting on a partially submerged sphere floating in vertical static equilibrium.

Hydraulic coupling

Hydraulic forces are calculated for each sphere within a multi-sphere object. With hydraulic coupling, the total force acting on a multi-sphere object within the discrete element method is the sum of hydraulic forces and contact forces. The object force is given by:

$$\boldsymbol{F}_{obj} = \sum_{i=0}^{n_o spheres} \boldsymbol{F}_{sph,c} + \boldsymbol{F}_{sph,h} \tag{4.13}$$

where $\boldsymbol{F}_{sph,h}$ is the sum of the hydraulic forces acting on a single sphere. Due to inviscid assumptions, hydraulic forces do not generate tangential forces about a sphere's centroid. However hydraulic forces do contribute to object moment when acting on a sphere offset from the object centroid. For the 1D modelling tool presented here, object moment is not considered. A 2D coupled modelling tool is presented in Chapter 5 that considers object rotation.

4.1.2 Object counter-force calculation

Channel blockage by floating debris is one of the key processes that increase upstream water levels and cause flow rerouting. In accordance with Newton's third law, floating objects exert an equal and opposite force to fluid. Ruiz-Villanueva and al. (2014*b*) used a similar approach, but considered viscous drag. Here reactions to the hydrodynamic and hydrostatic forces are equated in the horizontal direction. Opposing forces are applied to fluid flow as shear stress resulting in:

$$\tau_{obj} = \frac{F_{sph,h}}{A} \tag{4.14}$$

where A is an arbitrary area over which the stress acts. For a 1D scheme τ_{obj} is a scalar value given by:

$$\tau_{obj} = \frac{F_{sph,h}}{\partial x}, \tag{4.15}$$

Object coupling

The object shear stress calculated in Equation 4.15 are applied to each fluid cell through the source terms in equation 3.5 and 3.6. With the additional object shear stress, these become:

$$\partial_f \mathbf{u} + \partial_x \mathbf{f} = \mathbf{s} \tag{4.16}$$

$$\begin{aligned} \mathbf{u} &= \begin{bmatrix} \eta \\ q \end{bmatrix}, \mathbf{f} = \begin{bmatrix} \mathrm{q} \\ \frac{q^2}{\eta - Z_b} + \frac{g}{2}(\eta^2 - 2\eta Z_b) \end{bmatrix}, \\ \mathbf{s} &= \begin{bmatrix} -\frac{\partial x b(x)}{b(x)} q \\ -\frac{\partial x b(x)}{b(x)} \frac{q^2}{\eta - Z_b} - g\eta \partial x Z_b - C_f u|u| - \frac{\tau_{obj}}{\rho} \end{bmatrix} \end{aligned} \tag{4.17}$$

4.2 Analytical verification

The 1D coupled modelling tool presented here is first verified against an analytical solution to the equations of object motion. An analytical test case is presented here for the transport of a solid ball under steady uniform flow conditions in an open channel. The ball's density is exactly half that of the fluid, so the ball is transported with one hemisphere submerged, and one hemisphere above the fluid surface. The analytical test case is illustrated in Figure 4.4.

Sphere transport in steady uniform flow

Under steady uniform flow conditions, fluid depth and velocity remain constant with respect to time and distance along the channel. Therefore a floating sphere remains in hydrostatic equilibrium, and a hydrodynamic force results from the free stream velocity ($U = U\infty$). The acceleration of a floating sphere in steady uniform flow conditions can therefore be described by:

$$\ddot{x} = \left[\frac{\rho_w A_{sub} (U_\infty - \dot{x})^2}{m} \right] \tag{4.18}$$

For an initially stationary sphere, with an initial displacement of zero ($x_{t=0} = 0$ and

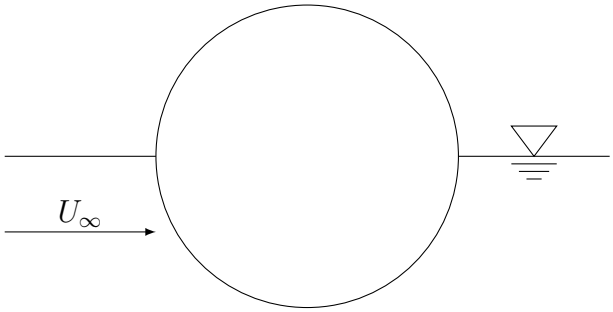

Figure 4.4: A partially submerged ball transported by steady uniform flow with velocity U_∞.

$\dot{x}_{t=0} = 0$), the velocity of the sphere at any point in time (t) is given by:

$$\dot{x} = \frac{\rho A U_\infty t}{\rho A t + \left(\frac{m}{U_\infty}\right)} \tag{4.19}$$

The horizontal displacement of the floating sphere (x) at any point in time is given by:

$$x = \frac{-m \log\left(\rho A t + \frac{m}{U_\infty}\right) + \rho A U_\infty t + m}{\rho A} + \frac{m \log\left(\frac{m}{U_\infty}\right) - m}{\rho A} \tag{4.20}$$

Analytical verification results

The new 1D floating debris modelling tool presented in this chapter is applied to simulate the transport of a solid ball floating in steady uniform flow. The ball has radius $10cm$ and density $500kg/m^3$. It is initially positioned in an open channel so that its centre of mass is at the exact elevation of the water's surface. The water depth is sufficiently high ($h >> 2R$) that ball floats freely and no contact occurs between it and the channel bed. As the ball's density is exactly half that of the fluid no vertical displacement occurs. From its initial resting position the ball is transported horizontally by steady uniform flow with a constant free stream velocity, $U_\infty = 5m/s$. The computational domain is divided into rectangular cells with horizontal length, $\Delta x = 0.05m$. As no contact occurs between the ball and the domain boundaries, the values of the contact parameters (K_n, C_n, K_s, C_s, μ) do not affect the simulation. Applying a time step of $t = 0.0001s$ the numerical and analytical solutions for ball velocity and displacement are shown in Figure 4.5. After a total simulation time of two seconds, the ball reaches its asymptotic velocity limit of $5m/s$. At which point it has been transported $10m$ horizontally from its initial position. The numerical model accurately achieves the analytical results as there is no noticeable difference between the results presented in Figure 4.5.

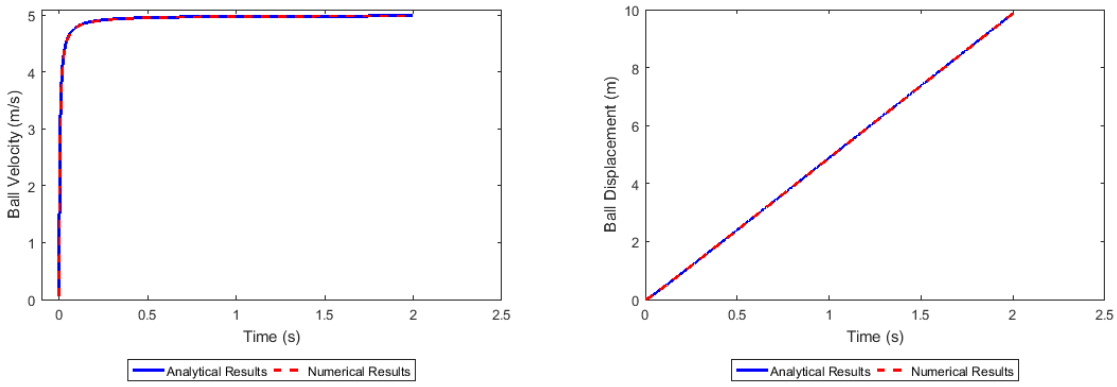

(a) Horizontal velocity of a floating ball (b) Horizontal displacement of a floating ball

Figure 4.5: Analytical verification - comparison of numerical and analytical solutions to the transport of a floating ball in steady uniform flow

4.3 Dam break experiments and validation

So as to better understand the physical processes that govern floating debris transport, an experimental study is performed to analyse the transport mechanisms of woody debris under surge-like flow conditions. The experiments are performed in a $35.5m$ long flume at the hydraulic research facility, Hohai University, China. The flume is set up to generate dam break conditions, which can be considered hydrodynamically similar to the destructive 'walls of water' observed during flash flooding.

4.3.1 Experimental set-up

Destructive 'walls of water' generate surge-like conditions that cannot be properly understood through standard flume set-up. However, the associated complex transitional hydraulic features can be replicated in a flume through dam break simulations (Albano et al., 2016; Goseberg et al., 2016; Nistor et al., 2011). Here experiments are performed in a 1m $\times$ 35.5m hydraulic flume. The experimental set-up is illustrated in Figure 4.6. The upstream region of the flume is adapted to incorporate a 5.5m x 1m reservoir, served by a pump and retained by a vertically lifting gate. Near-instantaneous gate release is achieved by a motor-driven dropping weight system. The flume is constructed from composite glass and steel vertical walls with a smooth-finished concrete bed. Four vertical depth gauges penetrate the flume in the downstream region, their locations are detailed in Figure 4.6. The depth gauges are calibrated prior to each experiment and record water depth at intervals of 0.0028 seconds. To capture the propagation of the wave front and entrained

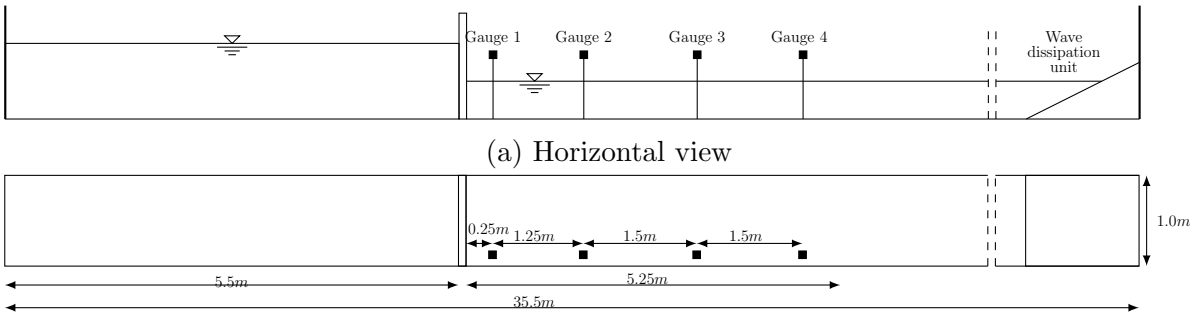

(a) Horizontal view

(b) Vertical view

Figure 4.6: Dam break flume experimental set-up.

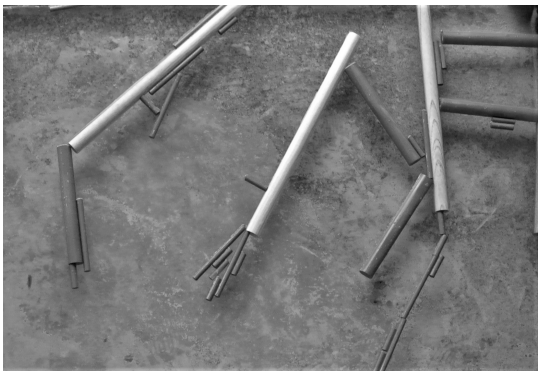

(a) Assorted wooden dowels floating freely.

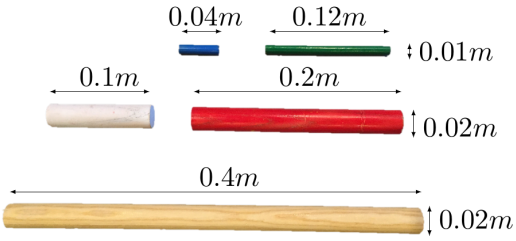

(b) Dimension of wooden dowels.

Figure 4.7: Painted wooden dowels used to replicate floating woody debris.

debris, a high-frame-rate digital camera is positioned above the flume 12m downstream of the western boundary and facing towards the gate. The camera records flume activity at a rate of 50 frames per second. Visual markers on the flume walls denote channel length. These enable post-experimental analysis of debris and wave-front position with respect to time.

Floating objects

Assorted wooden dowels are used to replicate floating woody debris in the flume experiments. The dowels depicted in Figure 4.7 are scaled at a ratio of 1:25 from the common LWD debris sizes described by Bocchiola et al. (2006). The dowels are made of beech wood and are painted to make them easily recognisable within the flume. Table 4.1 provides the physical properties of each of the six different debris sizes, which have been found through direct measurement and calculation. Where necessary, reasonable estimates of contact properties are made. The damping coefficients are calculated at a ratio $\zeta = 0.3$ of critical damping.

Scale Woody Debris

	Wood	Red	White	Green	Blue
Length (m)	0.4	0.2	0.1	0.12	0.04
Diameter (m)	0.02	0.02	0.02	0.01	0.01
Quantity	3	9	3	25	30
Mean density (kg/m^3)	850	850	850	540	540
Mass (kg)	0.109	0.054	0.027	0.005	0.002
Moment of inertia (kgm^2)	0.0015	0.00018	0.000023	0.000006	0.000001
K_n (kN/m)	30	30	30	30	30
C_n (kN/m)	20	20	20	20	20

Table 4.1: Physical properties of cylindrical wooden dowels used to replicate woody debris in dam break flume experiments.

1D Experiments

The experiments are performed in a uniform rectangular channel with no channel obstructions. In each case a singular wooden dowel is introduced to the flume and transported from its starting position by the approaching wave-front. The dowels are initially positioned downstream of the gate, 0.5m across the channel width, with 0° of rotation. Experiments are performed with varying water depths upstream and downstream of the gate; including wet bed and dry bed initial downstream water depths. The experimental set-up is designed so as to be easily reproduced by the 1D coupled modelling tool presented in this chapter. Of the initial conditions tested, five experimental cases have been selected to provide numerical model validation. These five validation cases have been selected on the quality of recorded images, visibility of wooden dowels within the flume, and stability of dowels within the centre of the channel (ie. minimal rotation). The five validation cases presented can, therefore, be considered approximately 1D.

4.3.2 Numerical modelling

A 12m × 1m section of the flume is selected as the computational domain. This contains the upstream reservoir and a 6.5m downstream stretch incorporating each of the four gauge points. The domain is divided into 1 200 cells with grid spacing of $\Delta x = 0.01m$. A Manning's coefficient of $n = 0.011s/m^{1/3}$ is applied uniformly across the entire domain. The wooden dowels are approximated using the multi-sphere method with a sphere spacing equal to dowel radius $\Delta s = R$. The experimental test cases are simulated for a duration of 40 seconds, with a time step of 0.0001 seconds. Hydrodynamic predictions are validated against experimental results for water depth at each of the four gauge points. The numerical predictions are validated against observed results for debris horizontal position

with respect to time, which has been recorded by analysing the captured images frame-by-frame. First wet-bed initial conditions are tested in cases 1,2 and 3. Test cases four and five present dry bed applications and are used to validate the numerical treatment of wet/dry interfaces.

Statistical validation

In addition to visual validation, statistical validation is performed to quantify the level of agreement between predicted and measured values. There are many different statistical validation techniques available to compare data sets. Here a Root Mean Square Error (RMSE) statistical comparison is favoured. Where many statistical comparisons are unitless, the value of RMSE has the same units as the data being compared. In this case, the units of RMSE are metres. A small value of RMSE indicates a closely matching data set. For debris transported by a dam break wave, in the 5.5m downstream stretch of flume, an RMSE value of less than 0.5m is here considered acceptable. For water depth at the four gauge points, acceptable levels of RMSE depend of the initial difference in upstream and downstream water depths. Here an RMSE value of less than 10% of the upstream and downstream depth differential is considered acceptable. The RMSE of a predicted data set relative to the corresponding observed values is given by:

$$RMSE = \sqrt{\frac{\sum_{i=1}^{n}(X_{obs,i} - X_{model,i})^2}{n}} \tag{4.21}$$

where X_{obs} is observed value, X_{model} is predicted value at time i for a data set containing n values.

1D Test case 1 - a wet bed experimental application

Initial conditions for the first test case are provided in Table 4.2. A green wooden dowel with dimensions $0.12 \times 0.01m$ is initially placed in the flume at $x = 6.44m$. Figure 4.8 shows captured images of the flume at 0, 2, 3.5 and 5 seconds after the gate is lifted. The white frame in the images indicates $0.5m$ distance intervals from the lifting gate.

The green dowel is particularly difficult to see due its small size and dark colour. The images in Figure 4.8 have been digitally enhanced in an effort to improve visibility. At t =0 the gate opens and a sharp-fronted shock wave propagates downstream. The wave front remains roughly rectangular as it propagates through the flume. Figure 4.8a shows that at t =0 the green debris is stable in the flume and has retained its alignment since initial placement. After 2 seconds the dowel is impacted by the wave front and begins to be transported downstream. At t =2 seconds the dowel is positioned just upstream of

Initial Conditions	
Upstream depth, η_u	$0.21m$
Downstream depth, η_d	$0.095m$
Uniform Manning roughness, n	$0.015s/m^{1/3}$
Dowel diameter, $\varnothing$	$0.01m$
Dowel length, l	$0.12m$

Table 4.2: 1D Test case 1 - initial conditions.

the wave front and has undergone a very slight rotation. At t =3.5 seconds the dowel is transported behind the wave front and continues to rotate. After 5 seconds the wave front reaches the end of the flume section and there is significant lag between the transported dowel, which is now oriented approximately 50 ° clockwise of its starting alignment.

Figure 4.9 compares the numerical and experimental results of water depth time history at the four gauge points. At each gauge the numerical scheme accurately predicts time of arrival of the initial wave front. However, numerical predictions do not achieve the maximum observed depth at the four gauges. The initial 'spikes' in observed water depth may be caused by the wave front splashing upon initial impact with the depth gauges. The numerical results do capture the subsequent peaks and match the overall shape of the graph well. The resulting RMSE values for gauges 1, 2, 3 and 4 are 0.0063m, 0.0058m, 0.0065m and 0.0068m respectively which indicate good agreement between predicted and observed values. Numerical and experimental values for debris position are presented in Figure 4.10. Although the numerical scheme captures the initial impact of the dam break wave, it underestimates the object's average velocity after impact which is illustrated by the gradient of each data series in Figure 4.10. This causes a time lag between observed and predicted object position. The correlation between predicted and observed debris position achieves an RMSE value of 0.6306m, indicating a poor agreement.

1D Test case 2 - a wet bed experimental application

Initial Conditions	
Upstream depth, η_u	$0.315m$
Downstream depth, η_d	$0.1m$
Uniform Manning roughness, n	$0.015s/m^{1/3}$
Dowel diameter, $\varnothing$	$0.02m$
Dowel length, l	$0.2m$

Table 4.3: 1D Test case 2 - initial conditions.

Initial conditions for the second test case are provided in Table 4.3. Here the upstream

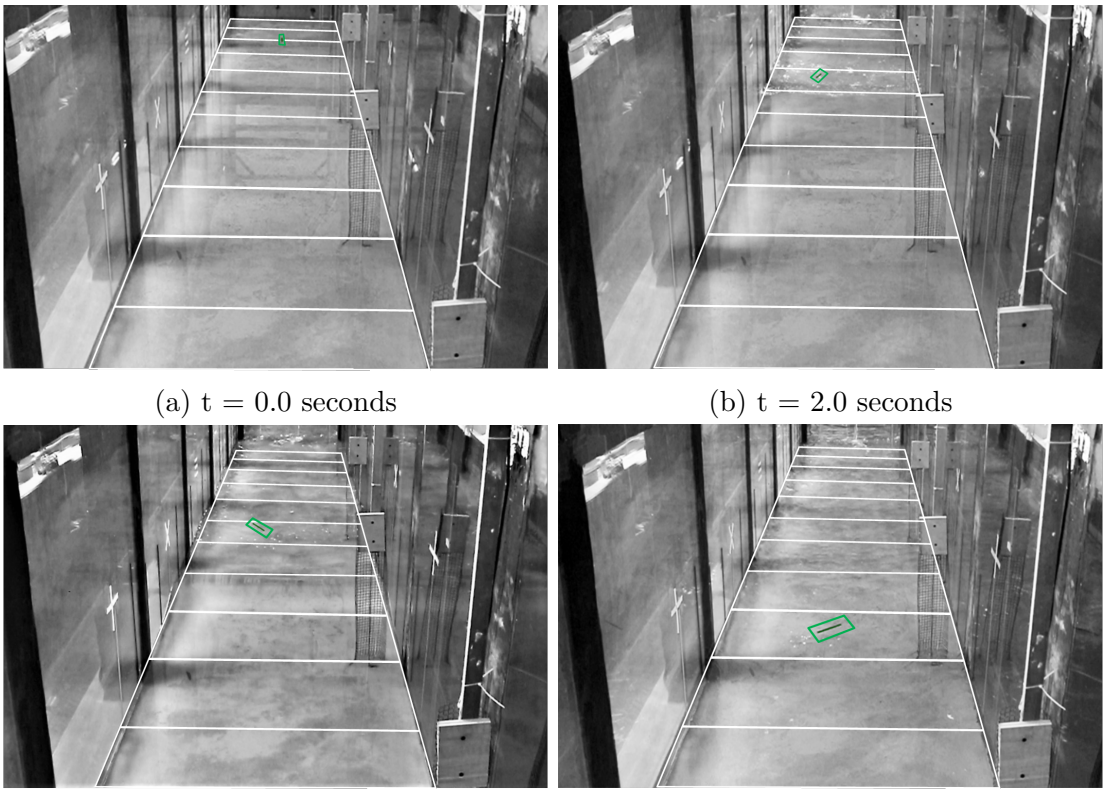

(a) t = 0.0 seconds

(b) t = 2.0 seconds

(c) t = 3.5 seconds

(d) t = 5.0 seconds

Figure 4.8: 1D Test case 1 - captured images showing position of debris.

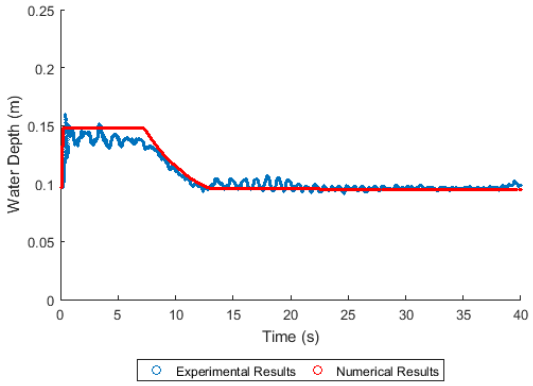

(a) Gauge 1

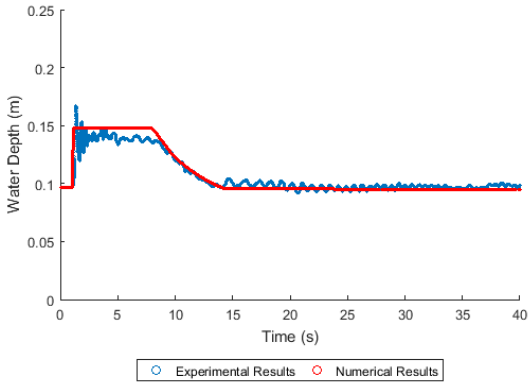

(b) Gauge 2

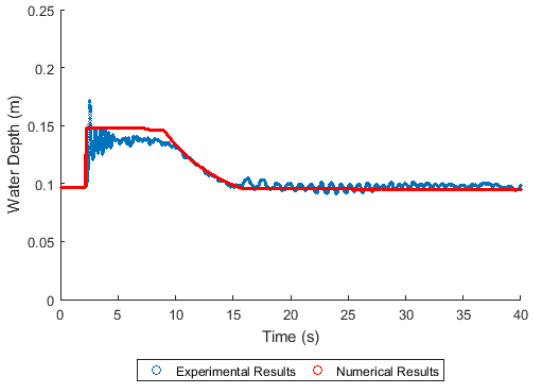

(c) Gauge 3

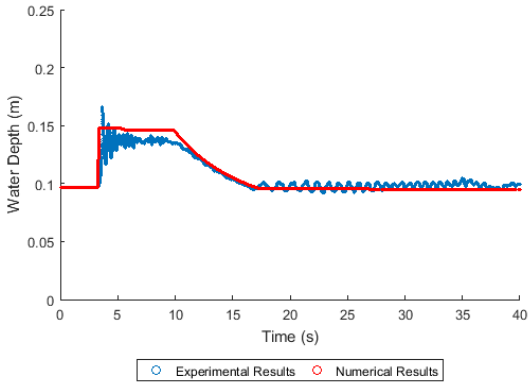

(d) Gauge 4

Figure 4.9: 1D Test case 1 - water depth (h m) with respect to time (t s).

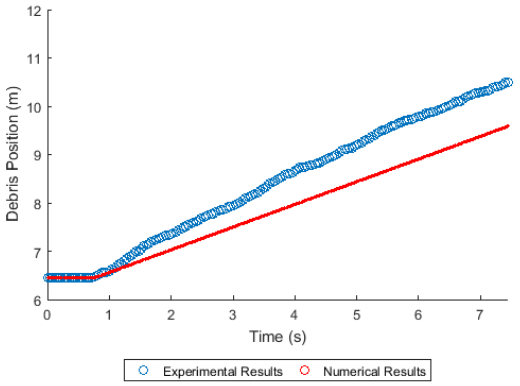

Figure 4.10: 1D Test case 1 - debris horizontal position with respect to time.

reservoir retains a water depth of 31.5cm. Downstream of the gate, is an initial wet bed depth of 10cm. A $0.1m \times 0.02m$ wooden dowel is initially placed at x=6.3m y=0.5m with zero degrees of rotation. Figure 4.11 shows captured images of the flume at 0, 2, 3.5 and 5 seconds after the gate is released. Figure 4.11a shows the flume at $t = 0$, an instant before the gate is released. As the wooden dowel is initially floating freely it rotates slightly out of 0° alignment. Upon lifting of the gate, the retained water is released and a rectangular wave front propagates downstream. The wooden dowel is entrained in the path of the wave and is transported downstream, roughly along the centre of the channel. Once transported the dowel maintains its orientation through 2 to 5 seconds.

Figure 4.12 compares water depth at the four gauge points, as measured and numerically predicted. The numerical scheme predicts time of arrival of the approaching wave well but slightly over predicts the elevation of the peaks. The corresponding values of RMSE for Gauges 1, 2, 3 and 4 are 0.00882m, 0.0109m, 0.0133m and 0.0153m indicating an acceptable level of agreement.

Figure 4.13 compares results for horizontal position of the dowel with respect to time. At $t = 0.5$ the wave front impacts the dowel, which then begins to move downstream from its initial position. From initial impact, it takes approximately 5 seconds for the dowel to travel the length of the study area. The numerical scheme accurately captures the initial wave impact and the position of the transported object with respect to time. This is reflected by an RMSE value of 0.1712m.

1D Test case 3 - a wet bed experimental application

Initial conditions	
Upstream depth, η_u	$0.225m$
Downstream depth, η_d	$0.105m$
Uniform Manning roughness, n	$0.015s/m^{1/3}$
Dowel diameter, $\varnothing$	$0.02m$
Dowel length, l	$0.4m$

Table 4.4: 1D Test case 3 - initial conditions.

Initial conditions for test case 3 are provided in Table 4.4. Upstream and downstream initial depths are 22.5cm and 10.5cm respectively. The largest $40cm \times 2cm$ wooden dowel is initially placed at $x = 6.8m$, $y = 0.5m$ with an orientation of 0°. Figure 4.14 shows captured images of the flume at 0, 2, 3.5 and 5 seconds after the gate is lifted. Because the initial depth differential between upstream and downstream is small (12cm) the resulting wave is shallow and propagates slower than in previous test cases. As the wooden dowel

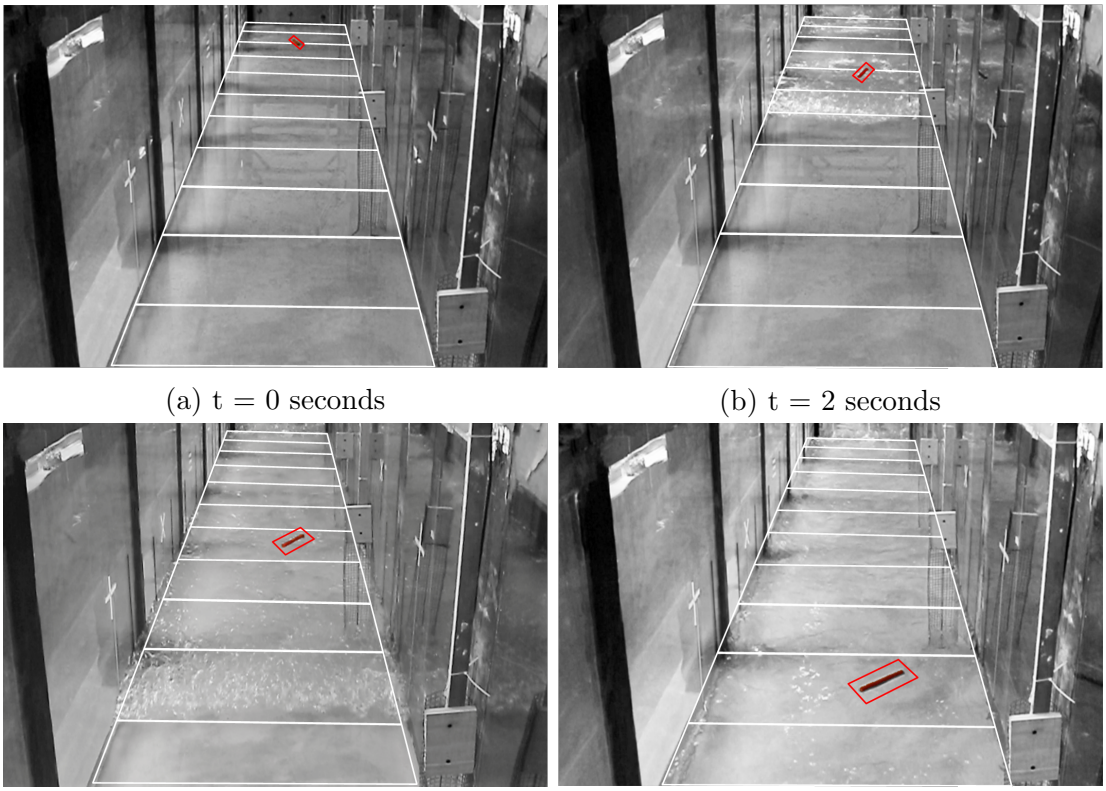

(a) t = 0 seconds

(b) t = 2 seconds

(c) t = 3.5 seconds

(d) t = 5 seconds

Figure 4.11: 1D Test case 2 - captured images showing position of debris.

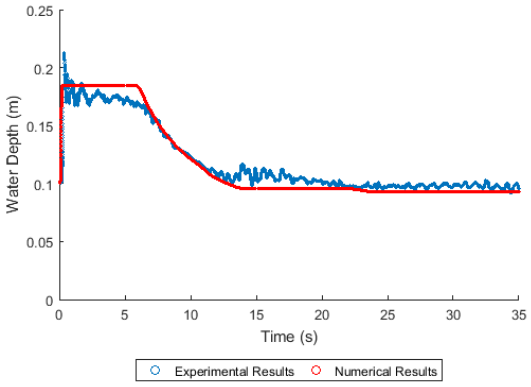

(a) Gauge 1

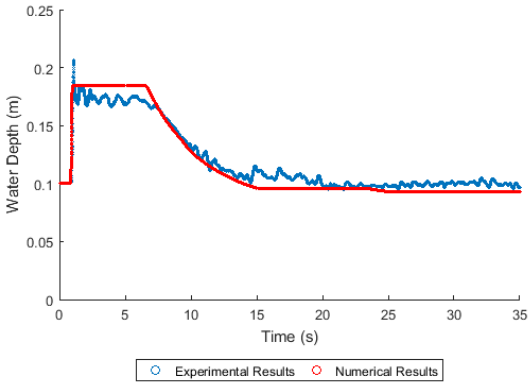

(b) Gauge 2

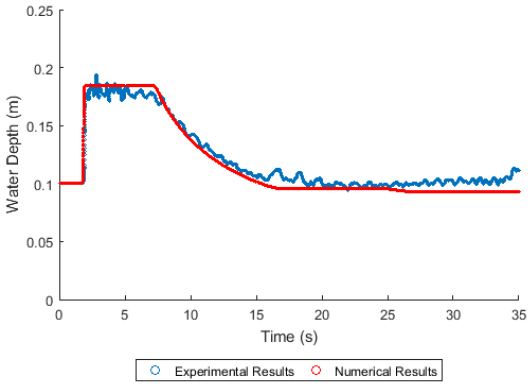

(c) Gauge 3

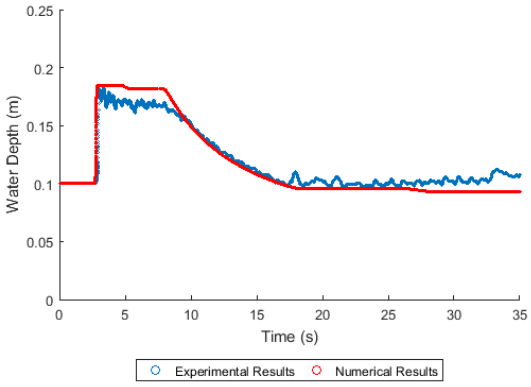

(d) Gauge 4

Figure 4.12: 1D Test case 2 - water depth (h m) with respect to time (t s).

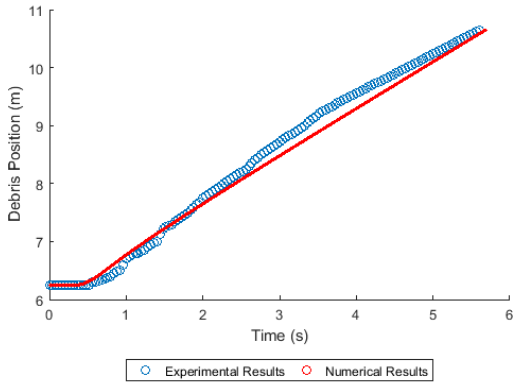

Figure 4.13: 1D Test case 2 - debris horizontal position with respect to time.

is transported downstream, it rotates significantly from its initial orientation. Figure 4.15 compares predicted and measured water depths at gauge points 1, 2, 3 and 4. Aside from initial splashing as the wave impacts the gauge, the numerical scheme accurately predicts both time of arrival and depth of the approaching wave front (RMSE = 0.0051m, 0.0048m, 0.0049m and 0.0059m respectively).

Figure 4.16 compares measured values for the horizontal position of the wooden dowel with the numerical predictions. Here the numerical scheme under predicts the total distance traveled by the dowel. Furthermore the experimental results show that the actual velocity of the wooden dowel fluctuates significantly during transport, whereas the numerical scheme predicts a near constant velocity after initial transport. Statistical comparison between predicted and observed debris position affirms a poor correlation (RMSE = 0.7101m). The significant difference between predicted and measured velocities in this test case could be due to instability and rotation of the wooden dowel within the flume. As it rotates, the area of the wooden dowel that is exposed to oncoming flow changes, at 0° orientation, only the circular cross section is exposed, whereas at 90° the full length of the dowel is exposed. Where exposed area is at a maximum the total hydraulic force is a maximum, and where exposed area is reduced, the resulting hydraulic force is reduced. In the test case presented here, the 1D numerical scheme does not predict object rotation and so may underestimate the total hydraulic force acting on the wooden dowel.

1D Test case 4 - a dry bed experimental application

Initial conditions	
Upstream depth, η_u	$0.205m$
Downstream depth, η_d	$0.0m$
Uniform Manning roughness, n	$0.015s/m^{1/3}$
Dowel diameter, $\varnothing$	$0.02m$
Dowel length, l	$0.1m$

Table 4.5: 1D Test case 4 - initial conditions.

The initial conditions for test case 4 are presented in Table 4.5. In this dry bed application, a water depth of 20.5cm is retained upstream of the gate, and a $10cm \times 2cm$ wooden dowel is placed at $x = 6.25m$, $y = 0.5m$ with 0° orientation. Prior to lifting of the gate, the position of the dowel on the dry bed is fixed. Figure 4.17 shows the flume 0, 1, 2 and 3 seconds after lifting the gate. After lifting, the resulting wave propagates downstream. As the waves propagates there are a number of reflective waves that traverse

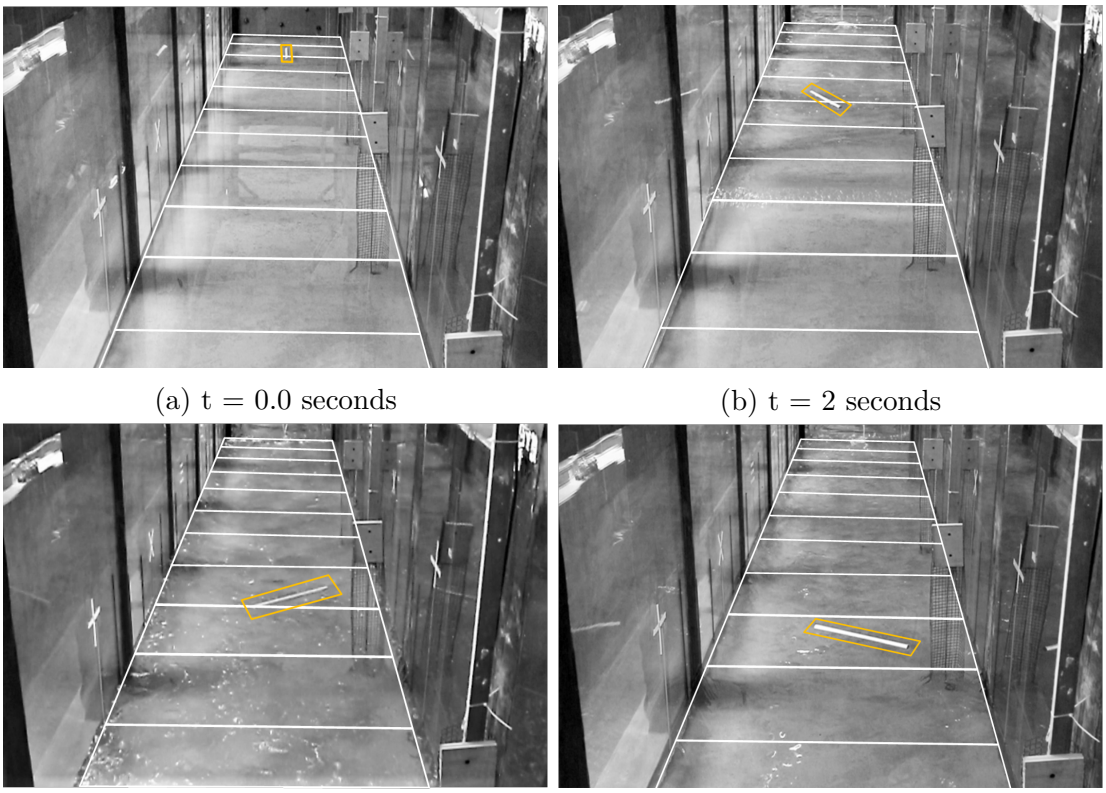

(a) t = 0.0 seconds

(b) t = 2 seconds

(c) t = 3.5 seconds

(d) t = 5 seconds

Figure 4.14: 1D Test case 3 - captured images showing position of debris.

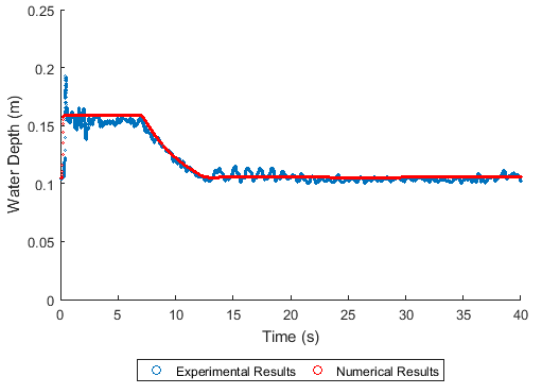

(a) Gauge 1

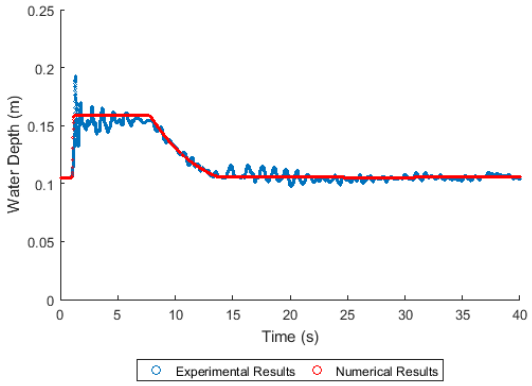

(b) Gauge 2

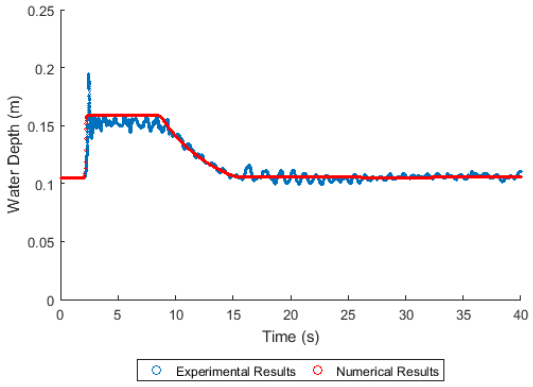

(c) Gauge 3

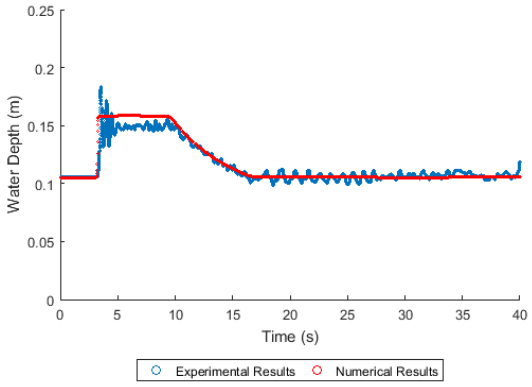

(d) Gauge 4

Figure 4.15: 1D Test case 3 - water depth (h m) with respect to time (t s).

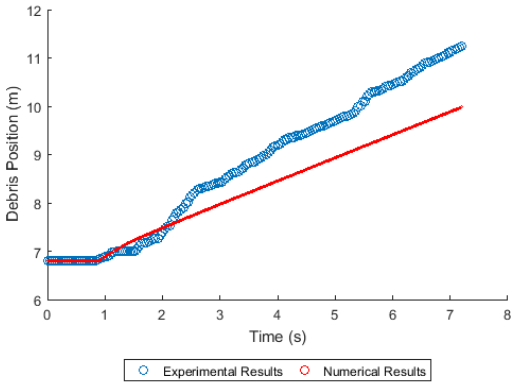

Figure 4.16: 1D Test case 3 - debris horizontal position with respect to time.

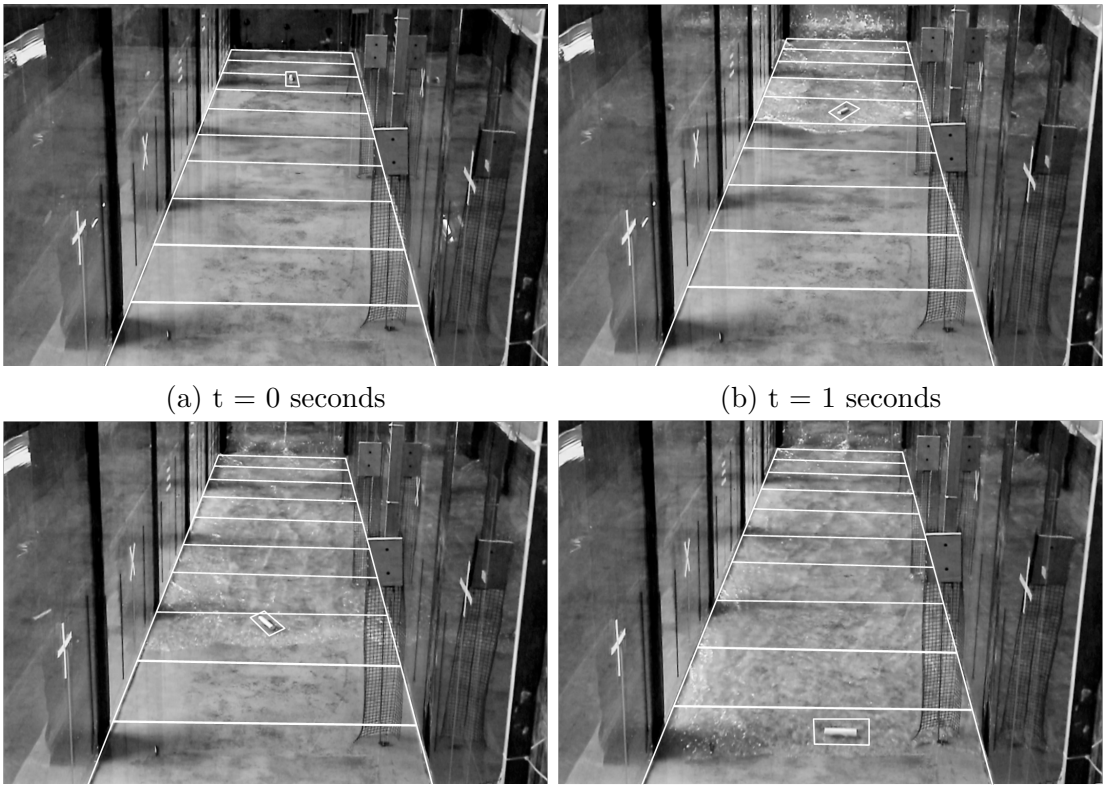

(a) t = 0 seconds (b) t = 1 seconds

(c) t = 2 seconds (d) t = 3 seconds

Figure 4.17: 1D Test case 4 - captured images showing position of debris.

the channel. Despite this, the wooden dowel is transported approximately along the centre of the channel. After 3 seconds the dowel has rotated approximately 90° from its initial orientation. Figure 4.18 shows the time histories of water depth at each of the four gauge points. Numerical predictions for time of arrival of the approaching wave are accurate. However at Gauge 1 the numerical scheme overestimates the maximum elevation of the wave, and for all four gauges it over predicts water elevation after the initial wave has passed. This results in a statistical validation of RMSE = 0.0130m, 0.0097m, 0.0090m and 0.0098m. Figure 4.19 shows the time evolution of the wooden dowel's horizontal position, which results in RMSE = 0.0130m. Both incipient motion and total distance traveled are captured well by the numerical scheme.

1D Test case 5 - a dry bed experimental application

This initial conditions for test case 5 are provided in Table 4.6. Initially a water depth of 41cm is retained by the gate. A $10cm \times 2cm$ wooden dowel is initially placed at $x = 6.75m$, $y = 0.5m$ with an orientation of 0°. Figure 4.20 shows the evolution of the dam break wave and wooden dowel through the flume at 0, 1, 1.5 and 2 seconds after

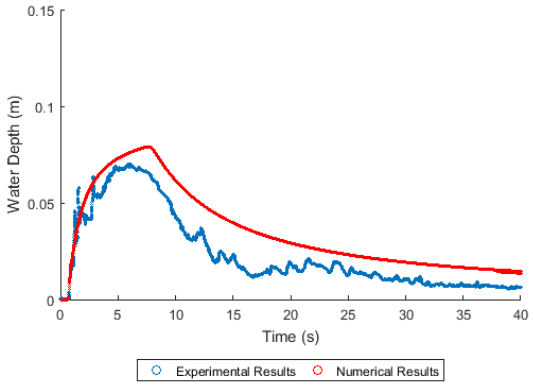

(a) Gauge1

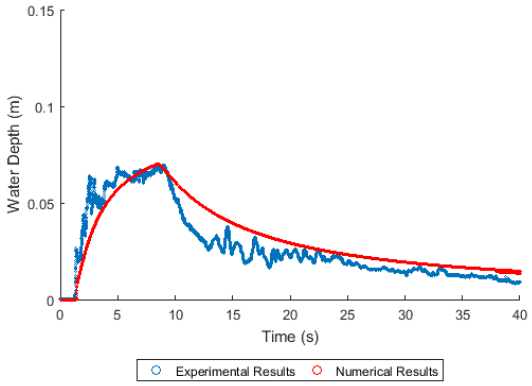

(b) Gauge 2

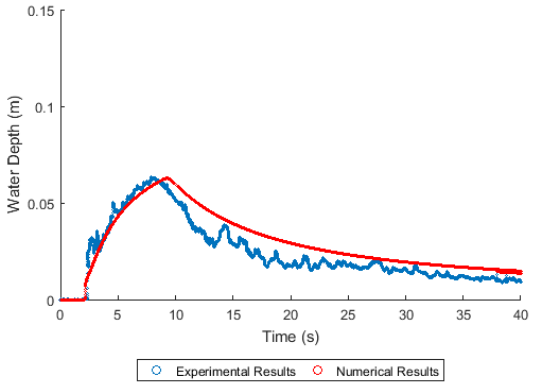

(c) Gauge 3

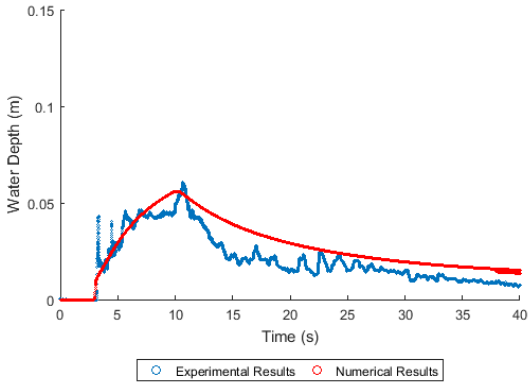

(d) Gauge 4

Figure 4.18: 1D Test case 4 - water depth (h m) with respect to time (t s).

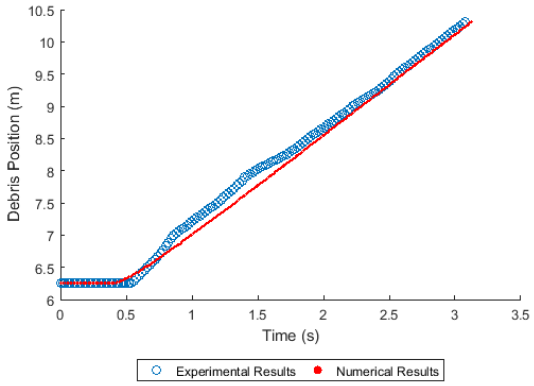

Figure 4.19: 1D Test case 4 - debris horizontal position with respect to time.

Initial Conditions	
Upstream Depth, η_u	$0.41m$
Downstream Depth, η_d	$0.0m$
Uniform Manning Roughness, n	$0.015s/m^{1/3}$
Dowel Diameter, $\varnothing$	$0.02m$
Dowel Length, l	$0.1m$

Table 4.6: 1D Test case 5 - initial conditions.

the gate is lifted. After the gate is lifted a sharp-fronted wave progresses downstream entraining the wooden dowel in its path. As the wave propagates a number of reflective waves traverse the channel. The wooden dowel remains centrally located within the flume width and rotates only a small amount as it is transported by the wave. Figure 4.21 compares the predicted and observed water depths. For Gauge 1 the arrival and depth of the oncoming wave is accurately captured by the numerical scheme but after the wave has passed, water depth is over predicted, resulting in RMSE = 0.0126m. At Gauges 2, 3 and 4 it slightly underestimates the peak surface elevation but captures the tail of the wave better (RMSE = 0.0094m, 0.0087m and 0.0108m). The numerical scheme also captures the overall transport of the wooden dowel well as numerical predicted position closely matches observed (RMSE= 0.0126m) as shown in Figure 4.22.

4.3.3 Discussion of results

The proposed 1D modelling tool predicts arrival time and water depth of a dam break wave well for both wet bed and dry bed experimental cases. For some of the wet bed applications, instability of the wooden dowel before the release of the gate may have caused rotation during transport and increased hydraulic forces. This may, in part, explain why the numerical predictions of distance traveled underestimated actual values for some of the wet bed cases. A number of other physical processes are also simplified by the 1D numerical scheme. The water velocity values, used to compute hydrodynamic force components are averaged over the depth of the fluid. The actual vertical velocity profile is effected by bed friction and surface tension, therefore numerical predictions of water depth will underestimate velocity at the surface. This may also lead to significant variation when calculating the forces on floating objects as the hydrodynamic force at the surface will be higher than the force averaged over total depth. The smaller, lower mass dowels also appear to be disproportionately affected by surface tension. This process is not captured by the numerical scheme. For the dry bed applications, debris transport is more accurately captured by the 1D coupled modelling tool.

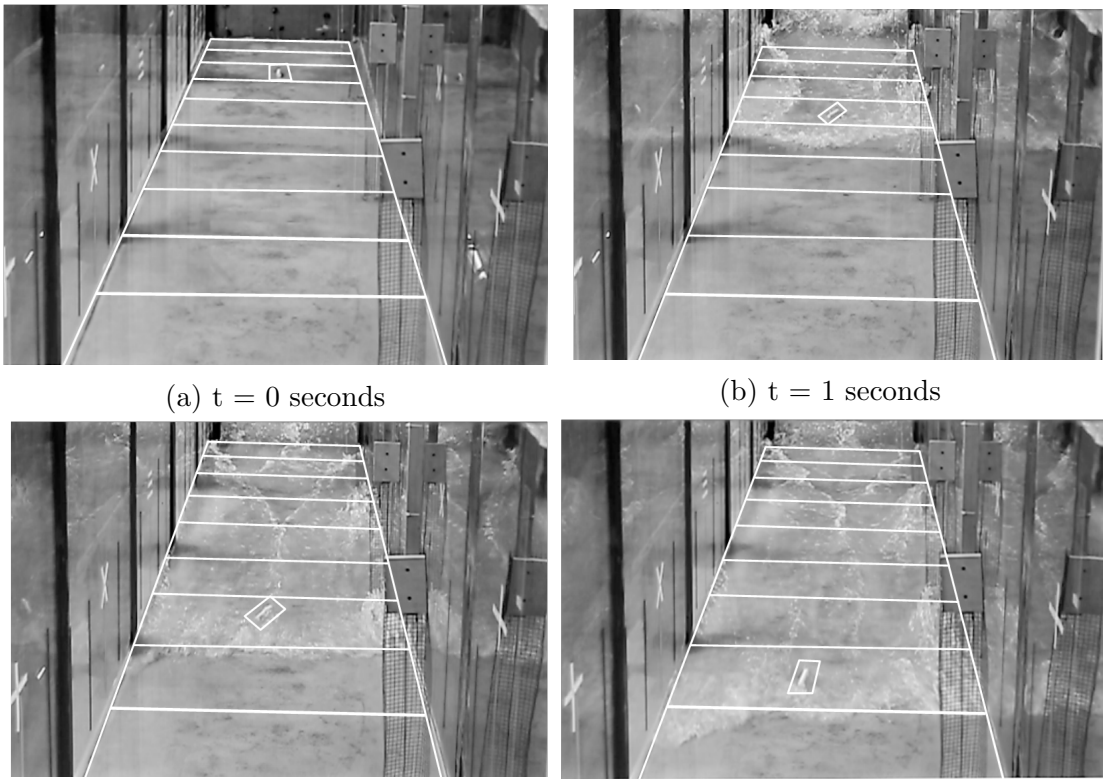

(a) t = 0 seconds

(b) t = 1 seconds

(c) t = 1.5 seconds

(d) t = 2 seconds

Figure 4.20: 1D Test case 5 - captured images showing position of debris.

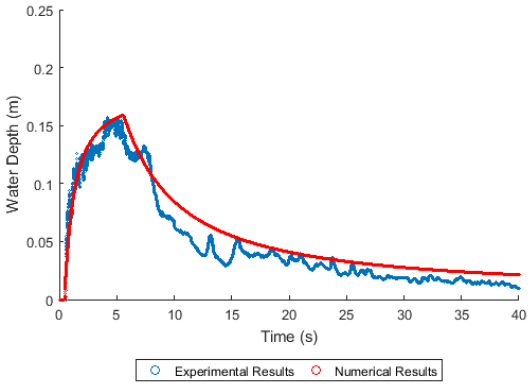

(a) Gauge 1

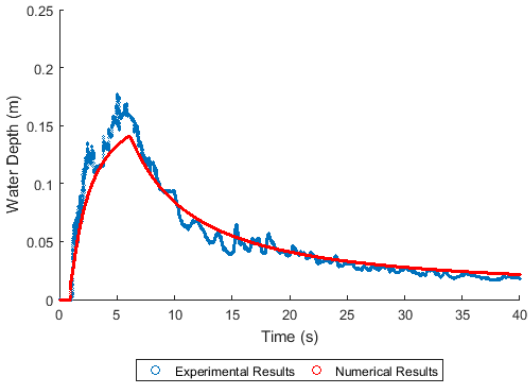

(b) Gauge 2

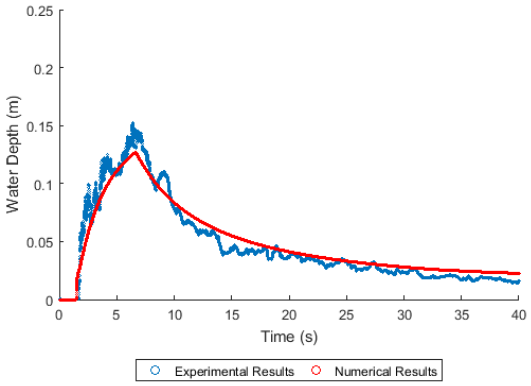

(c) Gauge 3

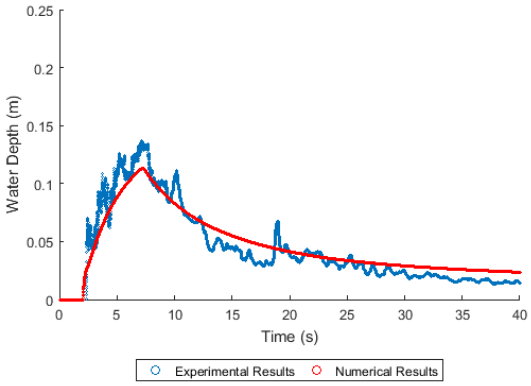

(d) Gauge 4

Figure 4.21: 1D Test case 5 - water depth (h m) with respect to time (t s).

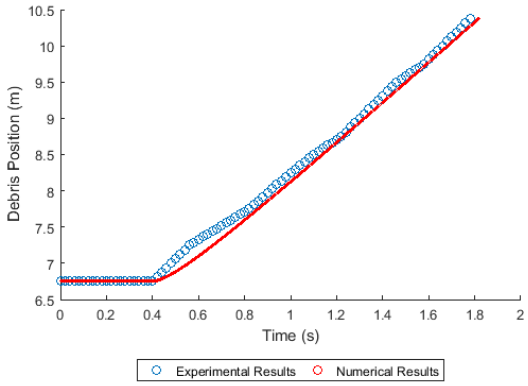

Figure 4.22: 1D Test case 5 - debris horizontal position with respect to time.

4.4 Conclusion

This chapter has presented the development of a 1D floating debris modelling tool that couples a 1D hydrodynamic finite volume scheme with the discrete element. The tool predicts water depth and depth averaged velocity with one horizontal dimension and the position, velocity and acceleration of spherical or cylindrical shaped objects floating with one translational degree of freedom. The coupling method has been verified against an analytical solution to the equations of object motion. With an appropriate time step, the numerical model solves the governing equations to an acceptable level of accuracy. The new 1D debris modelling tool has been validated against a series of experimental test cases where individual wooden dowels are transported by a dam break wave. The model performs well for most applications, however, where significant object rotation occurs, the numerical predictions tend to underestimate object velocity and result in under-prediction of the total distance traveled. Approximations of vertical fluid velocity profile may also contribute to under-prediction of object velocity. The results presented in this chapter demonstrate that a coupled finite volume-discrete element modeling tool is able to simulate the physical processes governing debris transport in a hydraulic flume where minimal rotation occurs. However in order to model more complex processes such as interaction with structures, a more sophisticated tool is required to predict 2D flow variables, object rotation and domain interaction. This is presented in the following chapter.

Chapter 5

2D Modelling of floating debris at obstacles

In Chapter 4 a 1D debris modelling tool has been presented that predicts unidirectional debris transport under 1D flow conditions. Though applications of such a tool are limited, the experimental and analytical validation performed in Chapter 4 demonstrates that a force balanced coupling of hydrodynamic and discrete element modelling schemes is able to simulate the physical behavior of floating objects. In this chapter the debris modelling scheme is developed further to predict more complex debris dynamics. This chapter presents a 2D debris modelling tool designed for simulating flash flood debris transport, over complex domains, where there is significant interaction between floating debris, hydraulic structures, and channel hydraulics. The scheme makes improvements over the previous 1D scheme by predicting flow variables in two horizontal dimensions and floating debris transport with translational and rotational degrees of freedom. Coupling between a 2D hydrodynamic scheme and the discrete element method is achieved through a balanced force coupling approach, which has been previously validated for 1D applications (Chapter 4). The new 2D debris modelling tool is validated against experimental studies performed in a hydraulic flume. Experimental test cases are used to examine the transport mechanisms of an array of scaled woody debris entrained by a dam break wave in the path of a fixed domain obstacle. The experimental findings provide an insight into the physics governing debris transport and enable validation of the 2D debris modelling scheme. Model validation is performed for three experimental test cases: two arising from experiments presented here; and an additional test case arising from experimental studies presented by Albano et al. (2016).

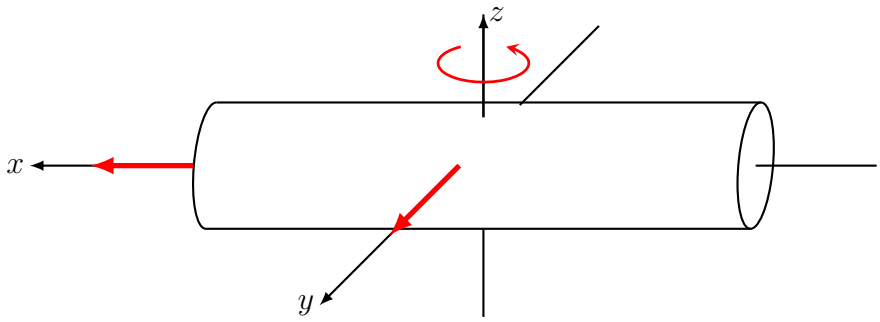

Figure 5.1: Translation in the x and y directions and rotation about the z axis for a floating cylindrical object.

5.1 A fully coupled 2D debris modelling scheme

The 2D coupled scheme presented in this chapter employs a finite volume Godunov-type hydrodynamic scheme. The scheme solves the governing shallow water equations to predict flow variables; depth and depth averaged velocity over a 2D Cartesian grid. Coupled with the hydrodynamic solver is a discrete element numerical scheme that predicts object motion in two horizontal dimensions with a single rotational degree of freedom; this is illustrated by Figure 5.1. The hydrodynamic and discrete element numerical schemes have been described in detail in Chapter 3. The numerical methods are coupled together using a force-balanced coupling procedure that is described for 1D application in Chapter 4. In this chapter the coupling procedure is extended to predict floating debris dynamics in a 2D system. While a description of the coupling procedure is not repeated, improvements made on the 1D coupled scheme are described here in detail. The coupling method described in this Chapter is entirely novel. No detailed coupling methodology is available within the relevant literature, therefore the methods described here have been developed and validated for the first time.

5.1.1 Representing floating objects within a 2D Cartesian grid

Unlike other approaches, where DEM is coupled with a similar discrete system (eg. SPH), here the two coupled modelling systems are based on differing forms of numerical discretisation. Within the hydrodynamic scheme, the computational domain is divided into a set of finite volumes. Whereas within the DEM, discrete objects behave within a continuum of open space. Coupling between these two numerical approaches is therefore not straightforward. The finite volume Godunov-type hydrodynamic scheme, employed here, divides the domain by a Cartesian grid of cells with spacing Δx and Δy. The DEM, divides floating objects into a series of connected spheres with spacing Δs (described in

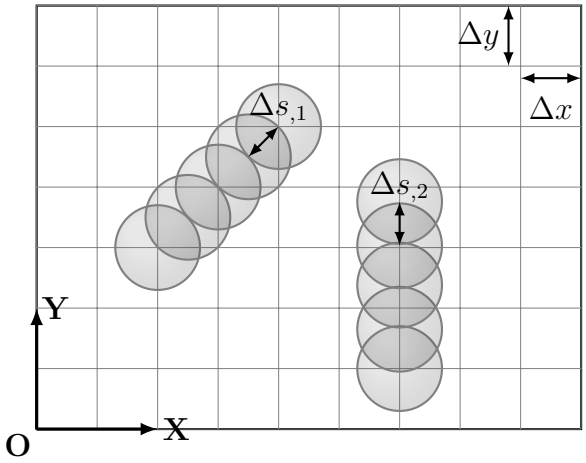

(a) Discrete element objects within Cartesian hydrodynamic grid

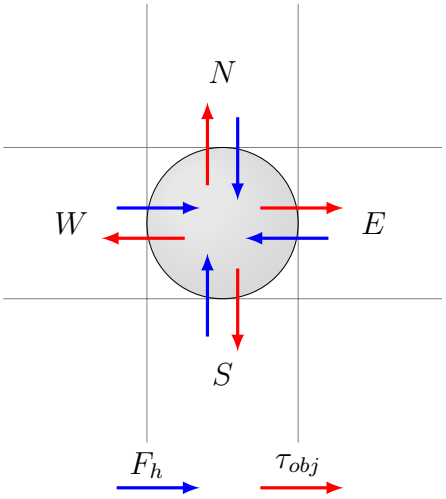

(b) Balanced forces for a single sphere

Figure 5.2: Visualisation of the domain discretisation applied within the new 2D floating debris modelling tool.

Chapter 3, section 3.2.2). Within the coupled scheme, multi-sphere objects are overlayed onto the hydrodynamic domain as illustrated by Figure 5.2a. The Cartesian grid and object global coordinate system share an origin (**O**). Each fluid cell contains the flow variables η, q_x and q_y and each object-sphere contains the transport variables ($\dot{\boldsymbol{x}}$, $\boldsymbol{x}$, ω and θ).

Force coupling in 2D

The hydraulic forces (F_h) and opposing object shear stresses (τ_{obj}) are calculated using the method described in Chapter 4, section 4.1. Within the 2D scheme, flow variables from adjacent grid cells are used to calculate hydraulic forces. Each adjacent grid cell borders either the north, east, south or western boundary of the sphere under consideration; this is illustrated in Figure 5.2b. Hydraulic forces are applied normal to the sphere boundary in the x or y directions (shown in Figure 5.2b). The object shear stresses (τ_{obj}) are applied to fluid cells and oppose the hydraulic forces as illustrated in Figure 5.2b. The reactionary τ_{obj} is applied through the source terms of the SWEs using the same method as presented for the 1D St.Venant equations in Chapter 4, section 4.1. Adding τ_{obj} to the SWEs (Equations 3.1 and 3.2) yields the following new source terms:

$$\mathbf{s} = \begin{bmatrix} 0 \\ \frac{(-\tau_{bx}-\tau_{obj,x})}{\rho} - g\eta\frac{\partial z_b}{\partial x} \\ \frac{(-\tau_{by}-\tau_{obj,y})}{\rho} - g\eta\frac{\partial z_b}{\partial x} \end{bmatrix} \tag{5.1}$$

where:

$$\tau_{obj,x} = \frac{f_{d,x} + f_{s,x}}{\partial x}, \tau_{obj,y} = \frac{f_{d,y} + f_{s,y}}{\partial y}, \tag{5.2}$$

5.1.2 Force application for multi-sphere objects

Where two spheres join within a multi-sphere object their contacting portions are here referred to as bound. For example in Figure 5.3b the eastern portion of the red sphere is bound to its neighbour. A point of difficulty arises when applying hydraulic forces to spheres with bound interfaces, as these portions of the sphere should not experience any force. Within the DEM, contact forces at bound interfaces are automatically prevented. However, without intervention, hydraulic forces would automatically by generated at all four adjacent grid cells to an object-sphere, as shown in Figure 5.2b. Handling hydraulic forces at bound interfaces requires special treatment; the following adjustment to the hydraulic force calculation is here proposed.

An imaginary box is placed around each sphere with north, south, east and west flow facing boundaries, illustrated by Figure 5.3a. Each box face is treated as either free, partially bound of fully bound. For example, Figure 5.3a illustrates a sphere where all four faces are free. Figure 5.3b illustrates a sphere where the east face is free; the west face is bound; and the north and south faces are partially bound. Figure 5.3c illustrates a sphere where north and south are partially bound; east and west are fully bound. Figure 5.3d illustrates a sphere where all four faces are bound. Values are allocated to the four faces that determine the proportion of each that is exposed to the flow. The value of each 'exposed face' lies within the range 0 to 1 and is stored within a vector ($[n, e, s, w]$). A face value of 0 denotes fully bound; where 0% of the face is exposed to flow. A value of 1 denotes a free face where 100% is exposed to flow; and $0 > face < 1$ denotes partially exposed where exposure lies between 0% and 100%. The values stored in the face vector $[n, e, s, w]$ are multiplied by the hydraulic force components at each sphere boundary to yield the adjusted net hydraulic force ($F_{h,adj}$).

5.1.3 Rotation about the object centroid

In the coupled debris modelling tool presented here, object rotation is simulated as acting about a vertical local axis penetrating an object's centroid (shown in Figure 5.1). To conform with in-viscid fluid assumptions, tangential hydraulic forces are ignored. However, hydraulic forces with points of action offset from the object centroid give rise to a moment acting about the vertical local axis. The adjusted hydrostatic and hydrodynamic

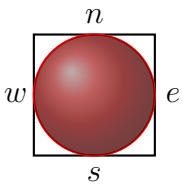

(a) A single sphere with four free faces

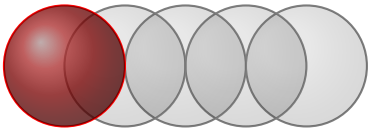

(b) An object-sphere with one bound and two partially bound faces

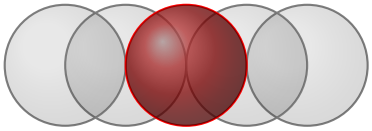

(c) An object-sphere with two bound and two partially bound faces

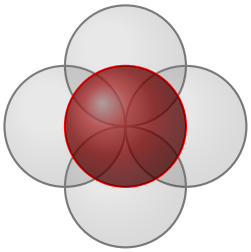

(d) An object-sphere with four bound faces

Figure 5.3: Examples of multi-sphere objects with bound and free flow faces in the north, east, south and west directions. In each example the sphere under consideration is highlighted in red.

force components are applied to each object-sphere with their points of action through the sphere's centroid. This is an approximation of the actual point of action, which ensures that individual spheres do not experience a hydraulic moment. The adjusted hydraulic forces contribute to the total moment acting on a multi-sphere object. Moments acting about the local x and y axes are ignored because rolling and pitching motions are thought to have minimal influence on debris dynamics. The adjusted hydraulic force vectors for each sphere contribute to total object moment as described by Equation 5.3.

$$M_{obj} = \sum_{i=0}^{n.spheres} M_{sph} + (\boldsymbol{F}_{sph,c}\boldsymbol{x}_{sph}) + (\boldsymbol{F}_{h,adj}\boldsymbol{x}_{sph}) \tag{5.3}$$

As an object rotates, the location of bound interfaces between spheres also changes. To account for this, values defining the proportion of a sphere exposed to flow, stored within the face vector ($[n, e, s, w]$'), are also adjusted to account for the rotation. For example Figure 5.4a shows a multi-sphere object with zero degrees of rotation ($\theta = 0$). The red sphere of interest has two bound faces (e and w) and two partially bound faces (n and s). Figure 5.4b shows a 45° rotation of the same object. After the rotation, the location of the red sphere remains unchanged, however the corresponding values for exposed faces have rotated so that all four faces are now partially bound and partially exposed to flow. At each time step, the values stored in the face vector ($[n, e, s, w]$') are updated to account for rotation.

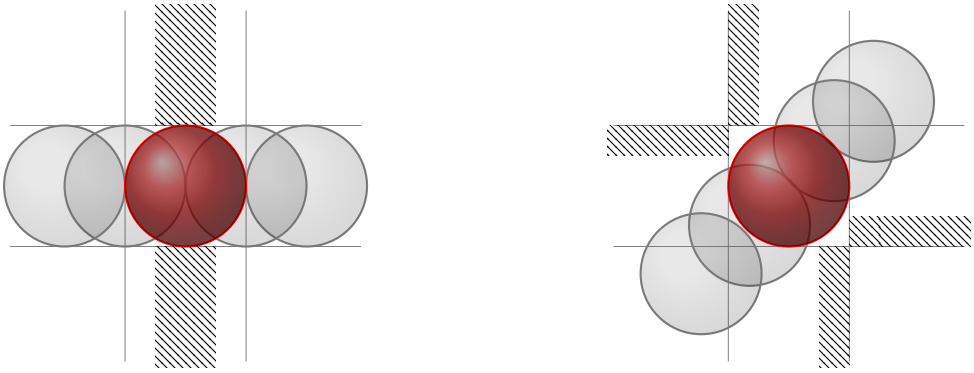

(a) $\theta = 0°$ (b) $\theta = 45°$

Figure 5.4: A multi-sphere object rotating from an initial orientation of $\theta = 0°$ to $\theta = 45°$. For the sphere under consideration (highlighted in red) the proportion of each face exposed to flow also rotates. The total exposed area for all four faces remains constant throughout rotation.

5.2 Experimental study of debris transport in the presence of obstacles

The interaction of floating debris with fixed hydraulic structures is an important process that can significantly alter flash flood dynamics and cause structural damage. Here flume experiments are performed to investigate the transport dynamics of an assortment of wooden dowels entrained by dam break flow conditions and the mechanisms by which they interact with a fixed domain obstacle. While there have been many similar studies into wood transport performed in a hydraulic flume (Bocchiola et al., 2008, 2006; Lyn et al., 2003) most have not investigated debris transport mechanisms under the surge-like flow characteristics associated with flash flooding. Here, dam break conditions are recreated in a hydraulic flume to investigate the specific physical processes that dominate this type of debris transport. The experimental data presented here enables model validation of the new 2D floating debris modelling tool presented in this chapter. Specifically its shock capturing features and ability to predict the position of floating objects are tested.

5.2.1 Experimental configuration

The experimental set-up is illustrated in Figure 5.5. The flume shares the same material and dimensional properties as the previous study presented in Chapter 4. It is $35.5m$ in horizontal length and $1m$ in width. The upstream boundary is closed and at 5.5m a lifting gate retains an upstream water body. Upon near-instantaneous gate lifting, the retained water is released and propagates downstream as a steep-fronted wave. Downstream of

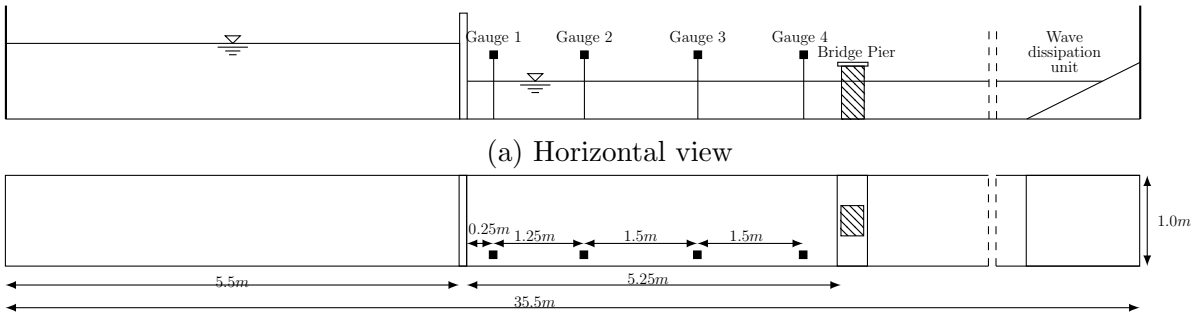

(a) Horizontal view

(b) Vertical view

Figure 5.5: Dam break flume experimental set-up

the gate, four depth gauges measure at time intervals of 0.0028 seconds and a high-frame-rate camera captures images of the flume at a rate of 50 frames per seconds. The upstream boundary is closed and at the open downstream boundary a wave dissipation unit prevents reflective waves from traveling upstream. The experimental set-up differs from the experiments presented in Chapter 4 in two ways. A scale model bridge is introduced to the downstream region of the flume and acts as a fixed obstacle throughout the experiments. A multitude of debris are introduced to the flume and transported simultaneously by the dam break wave. These are replicated by wooden dowels of varying sizes that are positioned in the flume prior to gate lifting. During each experimental run, the wooden dowels are entrained by the dam break wave and transported through the bridge openings.

Fixed domain obstacle

The model bridge consists of a pier and deck and is positioned 5.25 m downstream of the gate as illustrated in Figure 5.5. The bridge is constructed from perspex and is scaled at a ratio of 1:25. Assuming a structure that spans a 25m wide channel supported by a central $3.75m \times 3.75m$ pier, the resulting scaled model consists of a $0.15m \times 0.15m$ pier supporting a $1m \times 0.23m$ deck. Figure 5.6 illustrates the obstacle's shape and dimensions. The bridge is fixed in position by a large weight, with a mass of approximately 9.5kg.

Woody debris

A selection of wooden dowels are used to replicate floating woody debris. These have the same dimensions and material properties as described in Chapter 4, Figure 4.7 and Table 4.1. In the test cases presented here an assortment of dowel sizes are positioned within a $1m \times 1m$ section of channel just downstream of the gate. Both wet bed and dry bed initial conditions are tested and results for both are presented here. For the dry bed

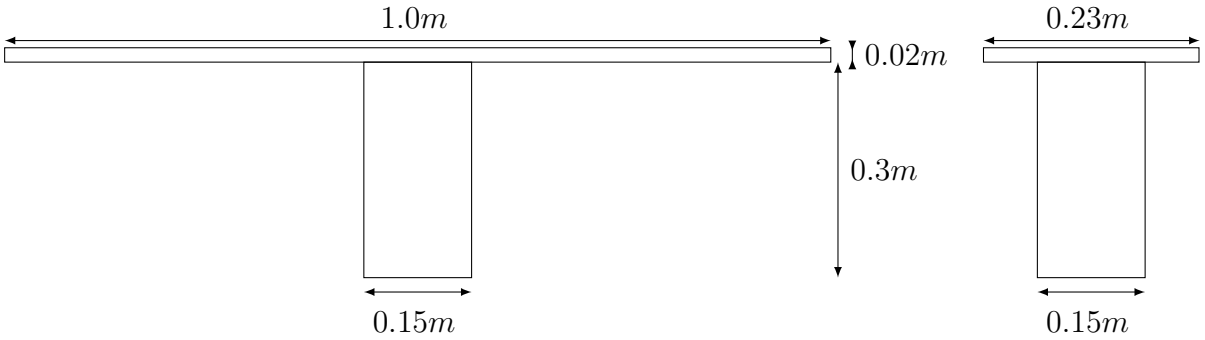

(a) Front view (b) Side view

Figure 5.6: Dimensions of perspex bridge pier

condition, wooden dowels are placed in a regular configuration. For the wet bed condition, movement while floating means that a regular configuration is not feasible. Instead the dowels are placed randomly and their positions photographed.

5.2.2 Experimental observations

In all of the experimental cases studied, the wooden dowels are transported downstream by a steep fronted dam break wave. Of the five debris sizes studied, those with the larger 2cm diameter are easily identifiable within the flume and when entrained by the wave front. The 1cm diameter dowels are difficult to identify visually. Figure 5.7c demonstrates the visual difference between the smaller and larger dowel. The transport mechanisms of the smaller and larger dowels also differ. The larger dowels tend to travel independently whereas the smaller dowels clump together. Figure 5.7b shows smaller dowels being transported downstream as a large mass. Although this transport mechanism is reported in literature, the causation my differ between flume experiments and field observations. For example, debris clumps are reported to arise in rivers because of irregular shaped branches that become entangled. Whereas in the flume the wooden dowels used are smooth cylinders. It is therefore more likely that dowel clumping in the flume occurs due to the disproportionate effects of surface tension on objects with smaller masses. If this is the case, the transport mechanism is associated with scaling and not truly representative of a floating debris transport process. Initial placement of dowels also affects their transport configuration, for example where dowels are initially sparsely placed within the flume, their transport tends to be spread, with more objects traveling independently, for example in Figure 5.7c. Where objects are initially closely packed, objects are more likely to travel as a large mass as in Figure 5.7b. In all cases, all wooden dowels are 'washed through' the bridge aperture during the experiments. In a very small number of cases an object

becomes stationary at the structure for a very short duration. For example Figure 5.7d shows a number of debris temporarily caught at the bridge pier. However, in no cases are these dowels stable enough to cause blockage of the bridge opening. There are a number of factors that appear to have contributed towards this;

- High velocity flow appeared to wash debris through.
- The bridge aperture was large compared to wooden dowels.
- The bridge pier was small compared to channel width.
- Floating objects were small compared to channel width.

In contrast to the deliberately placed channel obstacle, which does not cause significant debris entrapment, in some cases, the wave gauges interfere with debris transport and in a number of cases dowels become trapped at the wave gauge. For example Figure 5.7a shows a large dowel with 2cm diameter that has been lodged at a wave gauge. This entrapment supports conclusions made by Bocchiola et al. (2008) who suggested a relationship between opening size and blockage probability. Where the span between the gauge and channel wall is smaller than dowel length, entrapment is more likely. When dowels become trapped at depth gauges, the surface elevation just upstream of the entrapment is observed to increase, therefore it is likely that unintentional debris entrapment has affected depth measurements where these occurred.

5.2.3 Numerical modelling of debris transport

A 12m $\times$ 1m section of the flume is selected as the computational domain and contains the reservoir, fixed obstacle and four gauge points. The computational domain is divided into a cartesian grid of 120 000 cells with grid spacing of 0.01m. A Manning's bed friction coefficient of 0.011s/m$^{1/3}$ is selected through model calibration and applied uniformly to the entire domain. The northern, western and southern boundaries are allocated as reflective boundaries and the eastern domain boundary is treated as open. The bridge pier is represented by increasing the bed elevation to a height of 0.3m for all cells contained by the obstacle. Wooden dowels are approximated using the multi-sphere method for shape representation. Spheres are rigidly joined along a central axis with a spacing between centroids (Δs) equal to radius of the dowel. In each experimental case an assortment of wooden dowels are included. These range in size from the smallest available ($4cm \times 1cm$) to the largest ($40cm \times 2cm$). Within the numerical model, only the larger dowels are

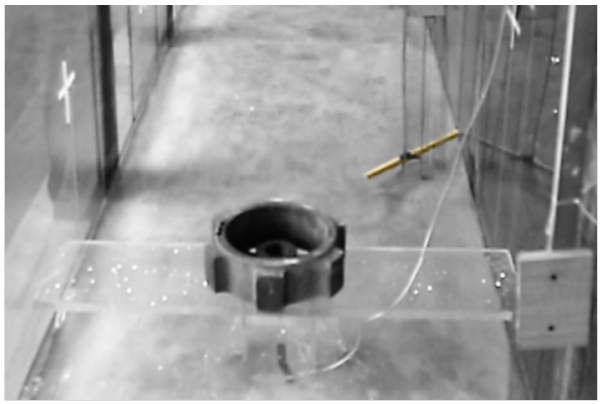

(a) Entrapped dowel

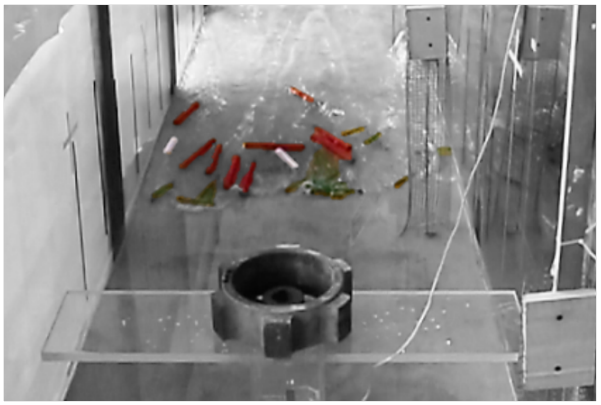

(b) Clumps of dowels

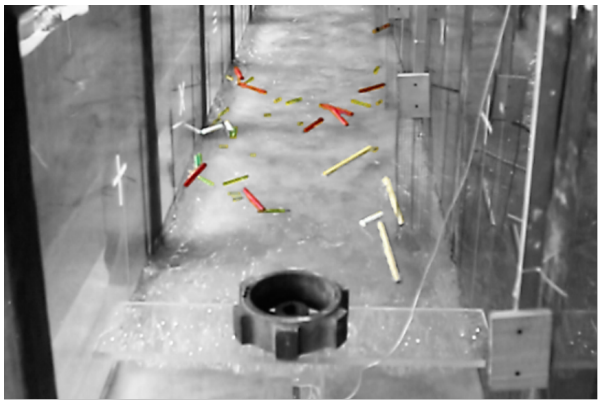

(c) Small and large dowels

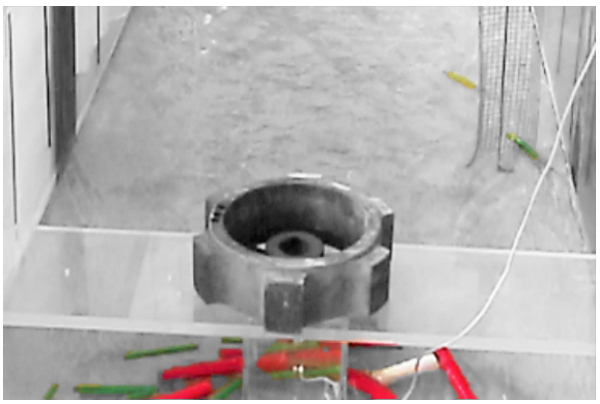

(d) Dowel blockage

Figure 5.7: Images of debris transport captured during flume experiments

simulated ($\varnothing = 2cm$). The smaller dowels ($\varnothing = 1cm$) are ignored for the following reasons;

- The smaller dowels are difficult to identify in the still images, making their transport difficult to validate visually.
- The smaller dowels are disproportionately affected by surface tension, a force that is not included in the numerical scheme, therefore their transport cannot be accurately predicted.
- It is unrealistic to expect a debris modelling tool to simulate all of the objects transported during flooding. It is therefore valuable to test the quality of numerical predictions for situations where not all of the floating objects are represented.
- The inclusion of additional floating objects adversely affects computation time. Therefore, in order to achieve reasonable computation time, only the most influential floating objects are included.

The numerical simulations are run for a total duration of 40 seconds. At each time interval the adaptive time step for fluid flow calculation, Δt (Equation 3.8) is checked against the critical times step for object collision, Δtc (Equation 3.36). The smaller of the two is selected.

Numerical predictions are compared against water depth time histories at the four gauges. The positions of simulated debris are validated visually against photographs captured during the experiment. The photo images have been digitally enhanced to easily identify the large dowels. The white frame visible in the images denotes horizontal distances of 0.5m along the channel, from the lifting gate.

2D Test case 1 - a wet bed application

The initial conditions for the first test cases are provided in Table 5.1. Initially, the depth of water upstream of the gate is 35.5cm and downstream is 5.4cm. Figure 5.2 shows the initial configuration of wooden dowels in the flume prior to gate lifting. A total of 52 wooden dowels are included in the flume, 12 of which are included in the numerical simulation. These are three $40cm \times 2cm$ dowels and nine $20cm \times 2cm$ dowels.

Figure 5.8 shows numerical simulations of fluid velocity and object position at t=3s, 3.5s, 3.8s and 4s. The model predicts the wave to travel approximately 1.1m/s. Wave impact with the bridge pier generates an area of reduced velocity immediately upstream of the obstacle and increased velocity immediately north and south of the bridge pier.

Initial Conditions	
Upstream depth, η_u	$0.355m$
Downstream depth, η_d	$0.054m$
no. of $40cm \times 2cm$ dowel	3
no. of $20cm \times 2cm$ dowel	9

Table 5.1: 2D Test case 1 - initial conditions

Table 5.2: 2D Test case 1 - initial dowel configuration

A wake is clearly visible downstream of the bridge pier after initial wave impact. The numerical model predicts that the floating objects are transported behind the wave front and rotate significantly during transport. Figure 5.9 shows a visual comparison between numerical predictions and experimental observations 1.72, 2.16, 2.72 and 3.44 seconds after the gate is lifted. After initial entrainment by the wave front, the dowels continue to propagate downstream towards the bridge. Most of the wooden dowels appear to travel independently. This is possibly because of their initial configuration within the flume. The smaller dowels are difficult to see. This is particularly true at t=1.72s, where the dowels are being transported among the turbulent wave front. The numerical model predicts that the larger dowels travel independently of one another. However the numerical model slightly under-predicts the position of debris within the channel, suggesting numerical calculation of debris velocity is also under-predicted. Figure 5.10 compares water depth measurements and predictions at the four gauge points, which result in statistical comparisons of RMSE = 0.0273m, 0.0258m, 0.0252m and 0.0269m for Gauges 1 -4 respectively. The numerical predictions match time of arrival of the dam break wave and height of the initial wave front reasonably well.

2D Test case 2 - a dry bed application

Initial conditions for the test case 2 are provided in Table 5.3. Initially, the upstream water depth is 29cm and downstream conditions are dry. Figure 5.2 shows the initial dowel configuration prior to gate lifting. A total of 37 dowels are included in the flume, 12 are simulated in the numerical model (three $10cm \times 2cm$ and nine $20cm \times 2cm$ dowels).

Figure 5.11 shows numerical predictions of fluid velocity and object position at t=0.28s, 1.08s, 2.08s and 2.6s. For the dry bed initial condition, bed roughness significantly affects the velocity of the travelling wave. At each selected time interval the fluid velocity increases towards the wave front. From their initial uniform configuration, the model

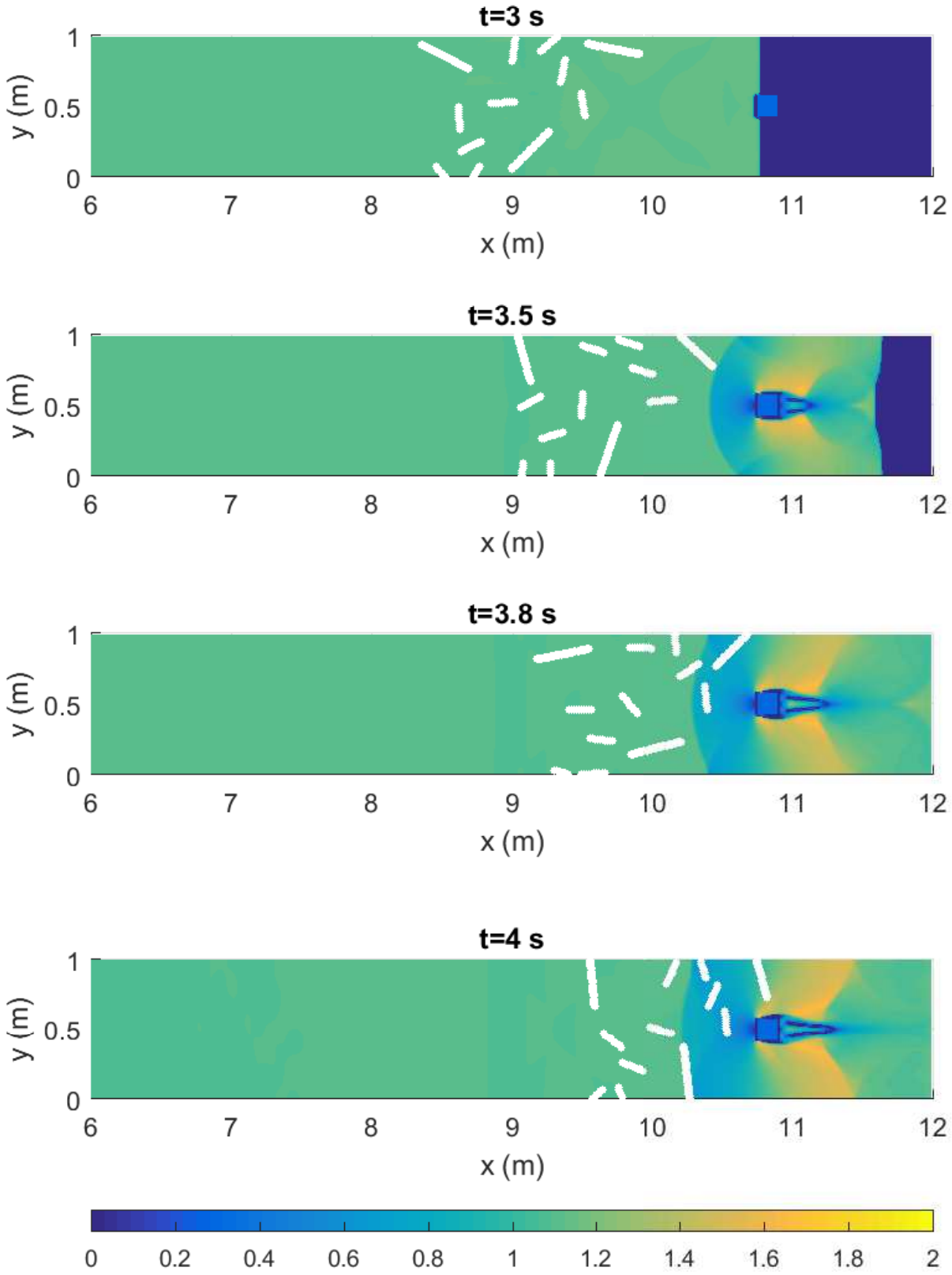

Figure 5.8: 2D Test case 1 - showing object position ($\mathbf{X}_{obj}$, m) and magnitude of the velocity vector ($|\boldsymbol{u}|$ m/s).

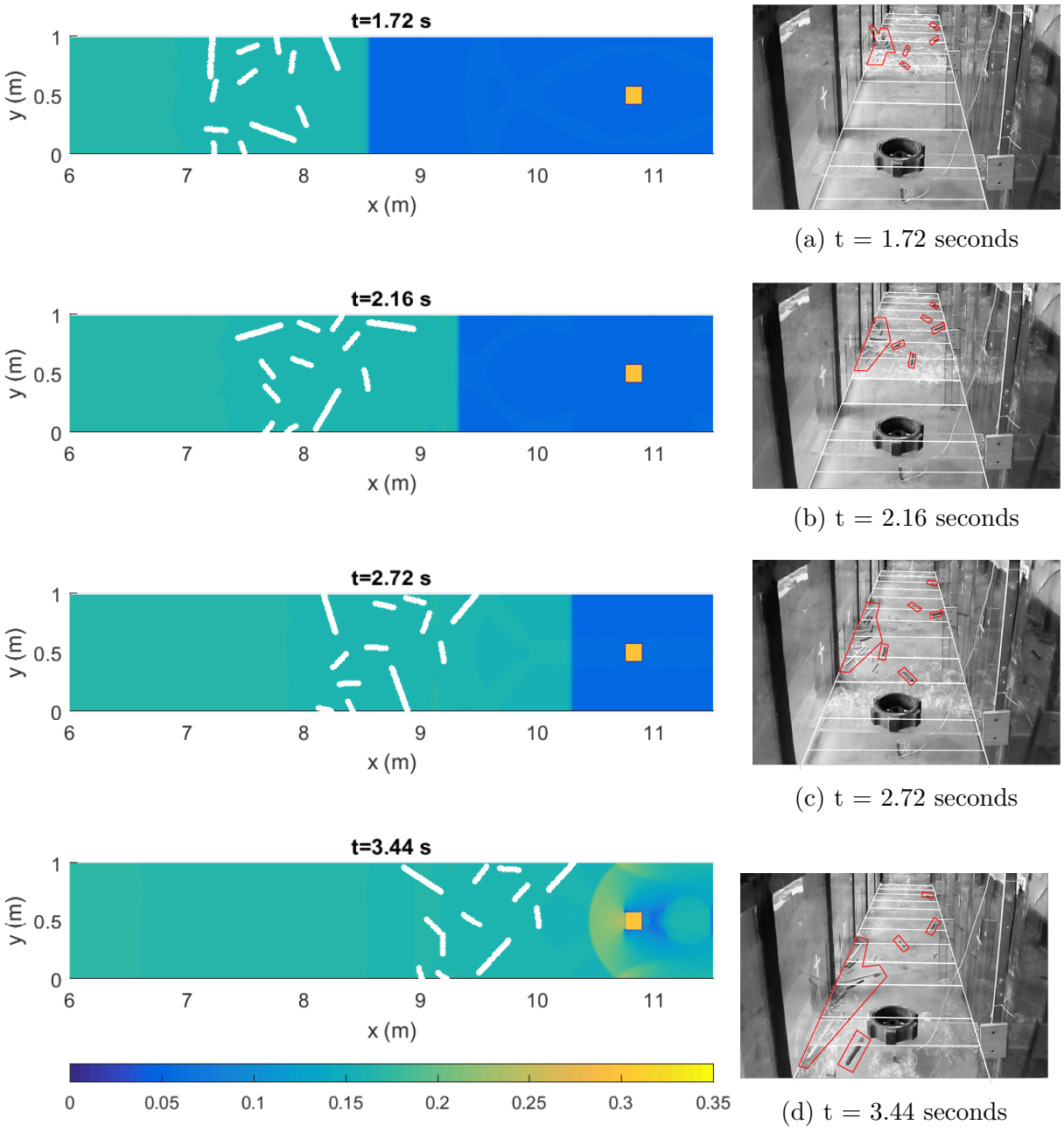

(a) t = 1.72 seconds

(b) t = 2.16 seconds

(c) t = 2.72 seconds

(d) t = 3.44 seconds

Figure 5.9: 2D Test case 1 - visual comparison of 2D modelling results. Numerical results (left) show object position ($\mathbf{X}_{obj}$ m) and water depth (h m).

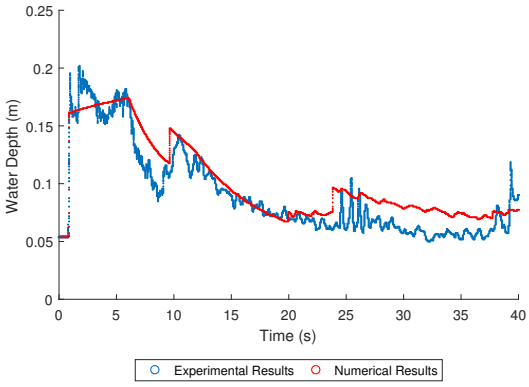

(a) Gauge1

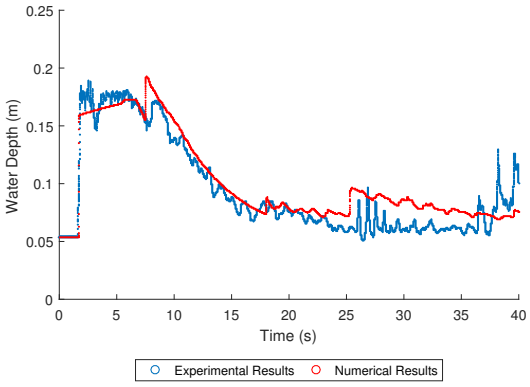

(b) Gauge 2

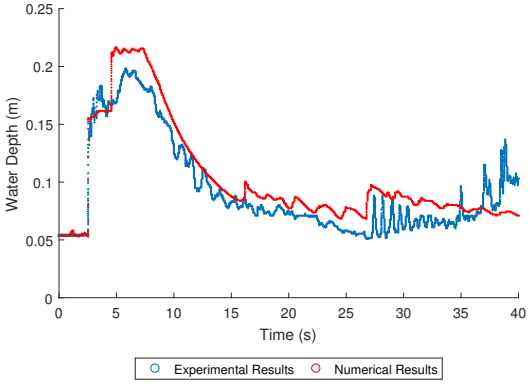

(c) Gauge 3

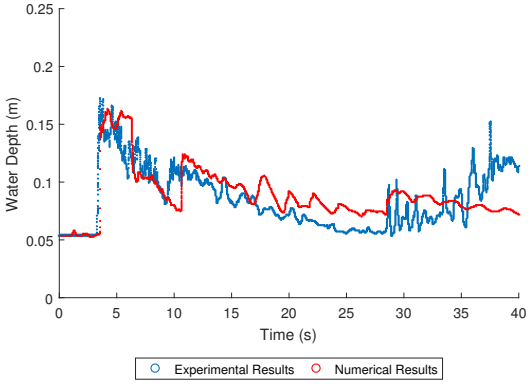

(d) Gauge 4

Figure 5.10: 2D Test case 1 - water depth (h m) with respect to time (t s).

Initial Conditions	
Upstream Depth, η_u	$0.29m$
Downstream Depth, η_d	$0.0m$
no. of $10cm \times 2cm$ dowel	3
no. of $20cm \times 2cm$ dowel	9

Table 5.3: 2D Test case 2 - initial conditions

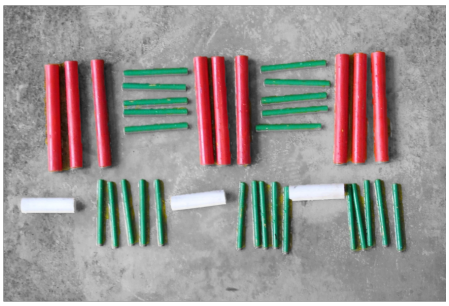

Table 5.4: 2D Test case 2 - initial dowel configuration

predicts that the objects travel as a concentrated mass towards the front of the propagating wave. Figure 5.12 shows the recorded and numerically generated images of the flume after 0.28, 1.08, 2.08 and 2.6 seconds following the gate being lifted. The recorded images show that the wooden dowels are transported downstream in a closer configuration than the previous test case. The close configuration may be due to the proximity of the dowels during initial placement, and the dry bed initial conditions. At 2.6s a number of dowels make contact with the bridge pier. The numerical model predicts that objects are transported as a close configuration and at t=2.6s, two dowels are trapped at the fixed bridge pier. The model, therefore, makes reasonable predictions of object position when compared against experimental observations. Figure 5.13 shows water depth with respect to time, as measured by four depth gauges and predicted by the coupled numerical scheme. Numerical predictions match well to height of the wave front and time of arrival for most gauges. However, at Gauge 2, the numerical scheme under predicts the height of the wave. At Gauges 1, 2 and 4, the numerical model does not capture the height of reflective waves that occur after the initial front has passed. The resulting statistical validation yeilds values of RMSE = 0.0175m, 0.0157m, 0.0170m and 0.0123m for Gauges 1, 2 3 and 4 respectively, indicating an acceptable level of agreement.

5.2.4 Discussion of results

Model validation for the experimental test cases presented here demonstrates that the new 2D debris modelling tool is suitable for predicting floating debris transport in a hydraulic flume. Though the numerical model does not reproduce the exact position of each floating object, the overall transport dynamics are recreated well. The model predicts both sparse and close transport configurations as well as debris entrapment at the fixed obstacle. Furthermore, the numerical model predicts water depth and arrival of the dam break wave to an acceptable level of accuracy, this is reinforced by statistical analysis. According to numerical predictions, the presence of a fixed bridge pier significantly alters flow regimes; generating backwater, increasing flow velocity and producing downstream wakes. During the experiments most debris is washed past the bridge pier with little interaction. In test case 2 some debris becomes caught at the obstacle, though this is temporary. For the experimental test cases presented here debris interaction with the fixed obstacle is limited. Additionally debris entrapment is difficult to identify in the experimental images due to camera positioning.

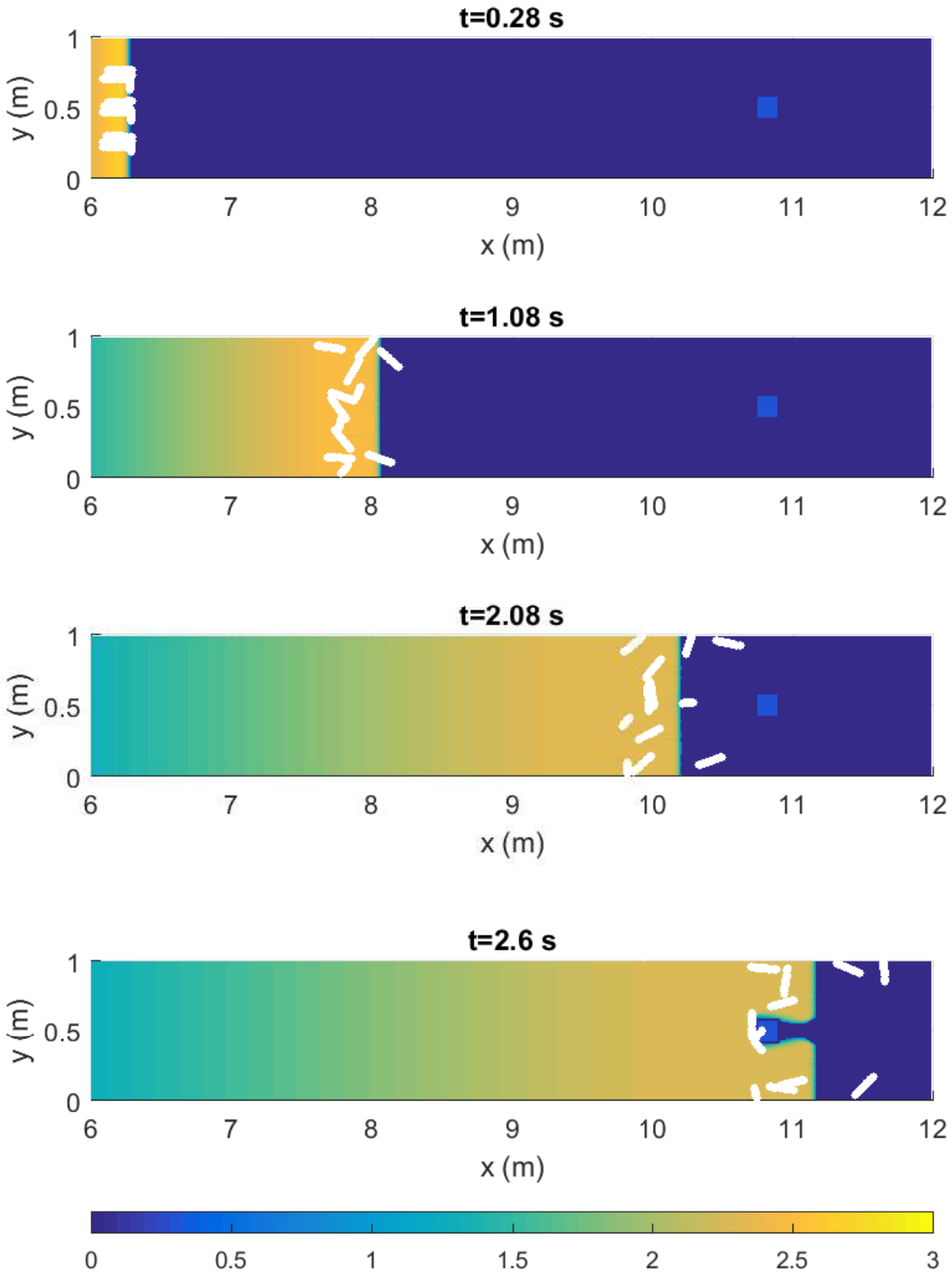

Figure 5.11: 2D Test case 2 - showing object position ($\mathbf{X}_{obj}$, m) and magnitude of the velocity vector ($|\boldsymbol{u}|$ m/s).

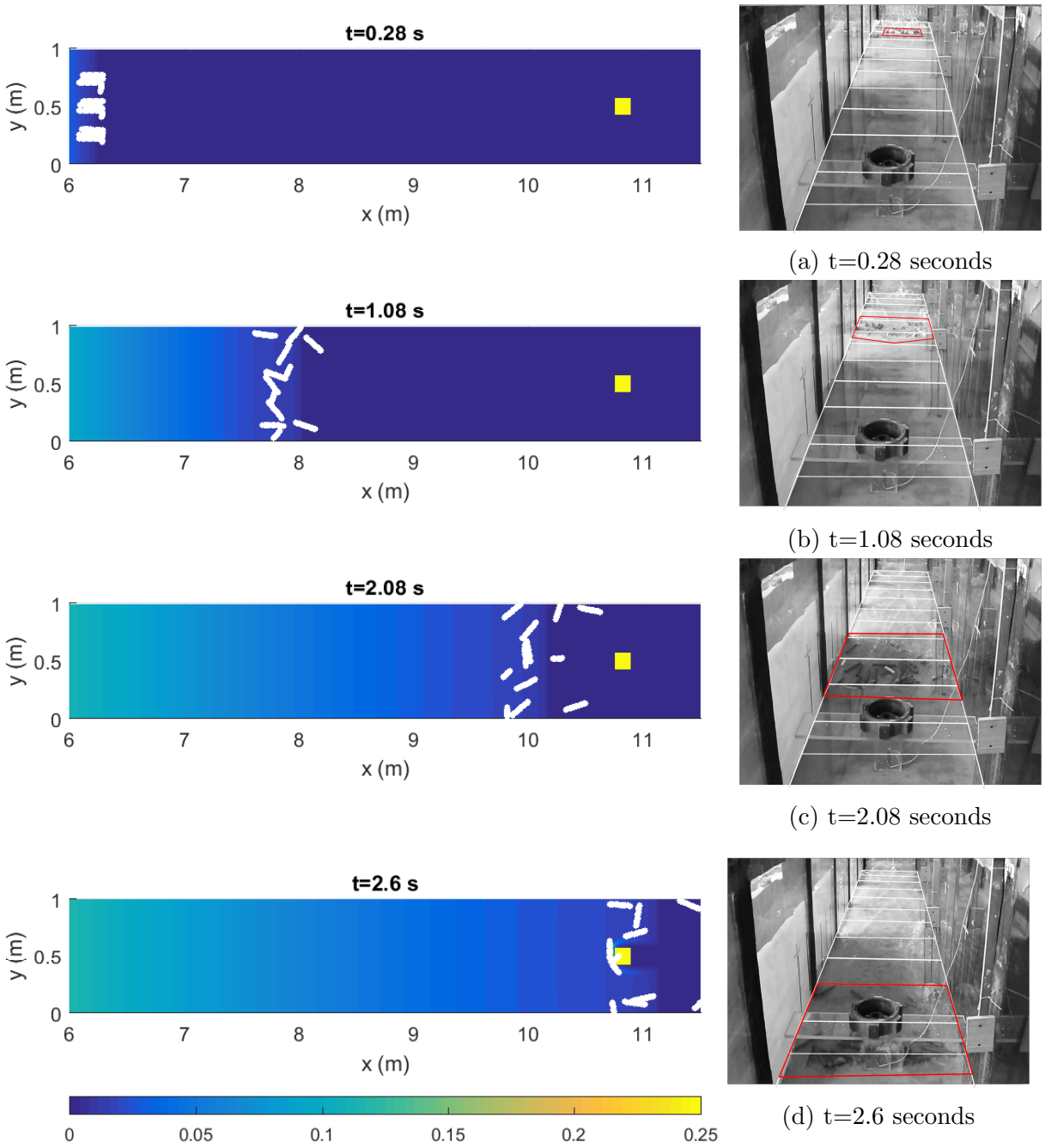

(a) t=0.28 seconds

(b) t=1.08 seconds

(c) t=2.08 seconds

(d) t=2.6 seconds

Figure 5.12: 2D Test case 2 - visual comparison of 2D modelling results. Numerical results (left) show object position ($\mathbf{X}_{obj}$ m) and water depth (h m).

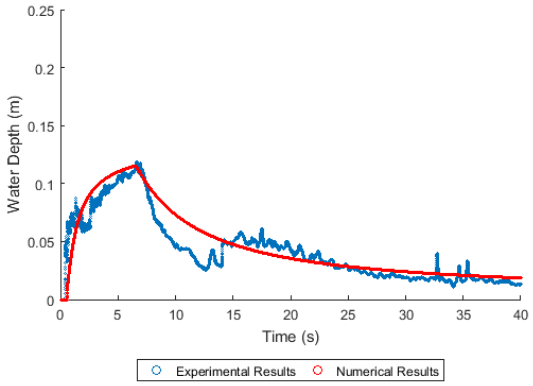

(a) Gauge 1

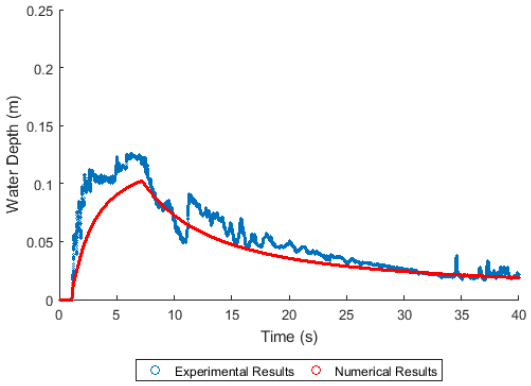

(b) Gauge 2

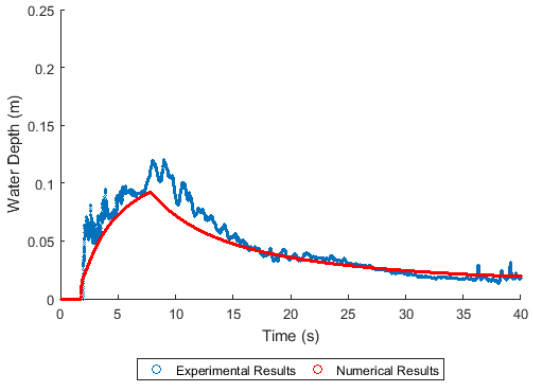

(c) Gauge 3

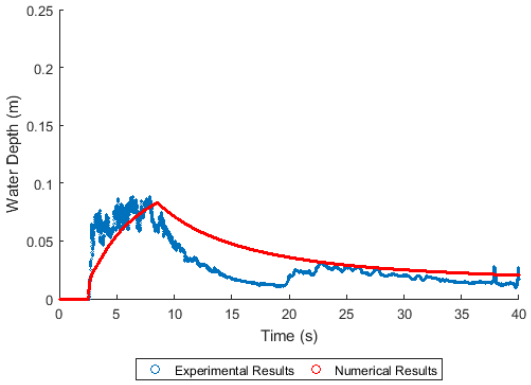

(d) Gauge 4

Figure 5.13: 2D Test case 2 - water depth (h m) with respect to time (t s).

5.3 Model validation for debris at obstacles

An additional validation case is presented here to allow further model validation, in particular of object interaction with obstacles. Experimental data has been sought to validate the numerical scheme's ability to capture debris entrapment. Albano et al. (2016) present an experimental study where objects are transported under dam break surge conditions and the object transport is impeded by fixed domain obstacles. Further model validation is performed against the results presented by Albano et al. (2016) to validate the new 2D debris modelling tool for simulating entrapment at structures.

5.3.1 Experimental configuration

The data presented by Albano et al. (2016) is for experiments performed in a dam break flume. The hydraulic flume has dimensions $0.5m \times 2.5m \times 0.5m$ and is illustrated in Figure 5.14. The channel composition comprises steel and glass walls and a bakelite floor. A reservoir, with horizontal dimensions $0.5 \times 0.5m$ retains an initial upstream water depth of $0.1m$. At $t = t_0$ the retained depth is released via a non-instantaneous vertical gate that is fully open after $t = 2s$. Three free-to-move objects are initially placed downstream of the reservoir. The objects are solid parallelepipeds (measuring $0.118m \times 0.045m \times 0.043m$). Their centres of mass are initially placed at $1.407m$, $0.229m$; $1.515m$, $0.221m$; and $1.622m$, $0.213m$ at a 45 deg angle. In addition to these objects, two fixed obstacles (measuring $0.300m \times 0.150m \times 0.300m$) are placed within the domain. The object's positions are fixed at: a) 1.40 m from the west domain boundary, 0.020 m from the north domain boundary; b) 1.950 m from the west domain boundary, 0.060 m from the south boundary. Water depth evolution over time is measured at two gauge points, positioned directly in front of the two fixed obstacles. Albano et al. (2016) present the results of five experimental runs using the same flume configuration, initial conditions and boundary conditions.

5.3.2 Numerical simulation of debris at obstacles

The experimental set-up is reproduced using the new 2D floating debris modelling tool at a scale of 1:1. The domain is discretised by a Cartesian grid of 240×20 cells, resulting in a grid resolution of $0.025m \times 0.025m$. The two fixed domain obstacles are recreated by increasing the local bed elevation to a height of $0.3m$ in cells containing the two obstacles. The remaining bed elevation is $0m$. The north, south and western walls of the flume are specified as reflective boundaries, the eastern, open flume boundary operates under slip conditions. The upstream reservoir, initially still and retained behind a lifting gate, is

Object parameters			
Length	0.118m	No. of Spheres	5
Width	0.045m	Sphere diameter	0.0225m
Height	0.043m	K_n	20 kN/m
Mass	$0.025kg$	K_s	12 kN/m
Inertia	$0.00034kgm^2$	μ	0.295

Table 5.5: Physical and computational parameters of modelled parallelepipeds

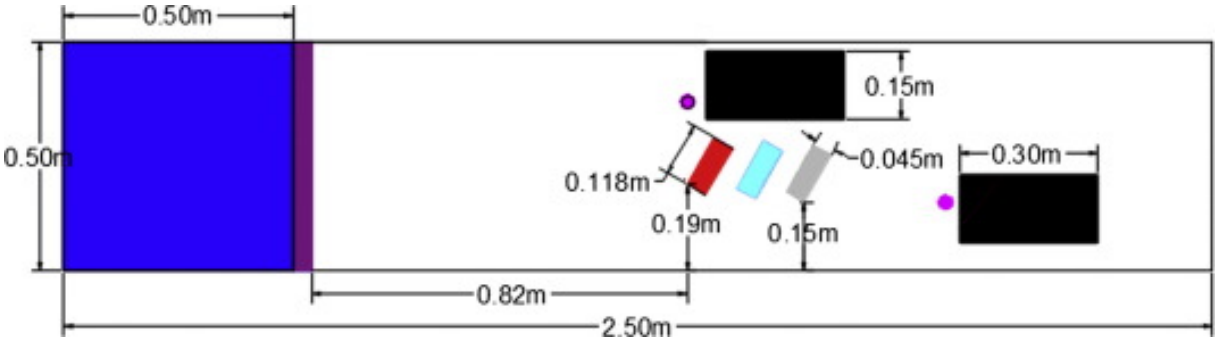

Figure 5.14: 2D Test case 3 - initial conditions for simulation of experimental test case (Albano et al., 2016).

reproduced as an initial water depth of 0.1m that at $t = 0.0s$ is instantaneously released. This is an approximation of experimental reservoir release that has a true release duration of $2.0s$. The three movable objects are initially positioned with their centres positioned as follows; Object 1= (1.407m, 0.229m), Object 2=(1.515m, 0.221m) and Object 3=(1.622m, 0.213m). Each parallelepiped is approximated, using the multi-sphere method, by five joined spheres. The physical and computational parameters applied to model each object are shown in Table 5.5. The initial computational domain configuration is shown in Figure 5.14.

5.3.3 2D Test case 3

Figure 5.15 shows numerical predictions of fluid velocity and object position at t=1s, 1.35s, 1.4s and 1.95s. Figure 5.16 shows numerical predictions for water depth and object positions compared with experimental observations. Comparisons are shown for a short section of the flume at t=1s, 1.35s, 1.4s and 1.95s. After 1s the wave front impacts the first fixed obstacle and begins to transport the first moving object. After 1.35 seconds the water depth immediately upstream of the first fixed obstacle locally increases, Figure 5.15 shows a local decrease in velocity over the same region. At 1.35s all three floating objects have been transported downstream towards the second fixed obstacle. Between t=1.35 seconds and t=1.4 seconds the transport of the three objects is impeded by the second

obstacle. At t=1.95s a region of locally increased velocity is visible within the narrow region between the two fixed obstacles. Immediately upstream of the second obstacle a region of locally deeper water with decreased velocity is generated. At t=1.95s two of the floating objects are transported away from the obstacle, the final object remains trapped. According to Figure 5.16 the numerical model predicts the object position to a high degree of accuracy.

Figure 5.17 shows a comparison between simulated and measured results for object x-position and water surface elevation with respect to time. The numerical model predicts object x-position to a good level of accuracy, this is demonstrated through statistical analysis. Values of RMSE for predicted position relative to observed position are presented in Table 5.6 and demonstrate a good level of agreement. The numerical model makes accurate predictions of the elevation of the dam break wave. However, the time of arrival of the dam break wave is not accurately captured. This is likely because of differences between the numerical and experimental lifting gate. The actual duration of the gate release was 2 seconds. Here the numerical model has been calibrated so that at t=0s the lifting gate is fully open, whereas in the experimental test cases, the gate was partially opened prior to this. The resulting values of RMSE for predicted water depth compared to observed values are presented in Table 5.6. For Gauge 1 the model achieves an acceptable level of agreement with most of the experimental data sets. However for Experiment B and D the RMSE value falls just outside of acceptable limits. For Gauge 2, although the model achieves a good visual fit with experimental water depths, the resulting values of RMSE reflect the delay in arrival of the dam break wave and the maximum observed water levels that are not met by the model. This has resulted in RMSE values outside of acceptable limits for this case.

RMSE (m)					
	Object X1	Object X2	Object X3	Gauge h1	Gauge h2
Experiment A	0.2496	0.0913	0.0692	0.0078	0.0240
Experiment B	0.3749	0.0780	0.1274	0.0130	0.0245
Experiment C	0.1843	0.0882	0.1138	0.0066	0.0285
Experiment D	0.1957	0.0347	0.0887	0.0107	0.0259
Experiment E	0.3224	0.0701	0.1200	0.0095	0.0263

Table 5.6: 2D Test case 3 - statistical validation of numerical predictions for object x-position (X_{obj}) and water depth (h) compared the experimental observations by Albano et al. (2016).

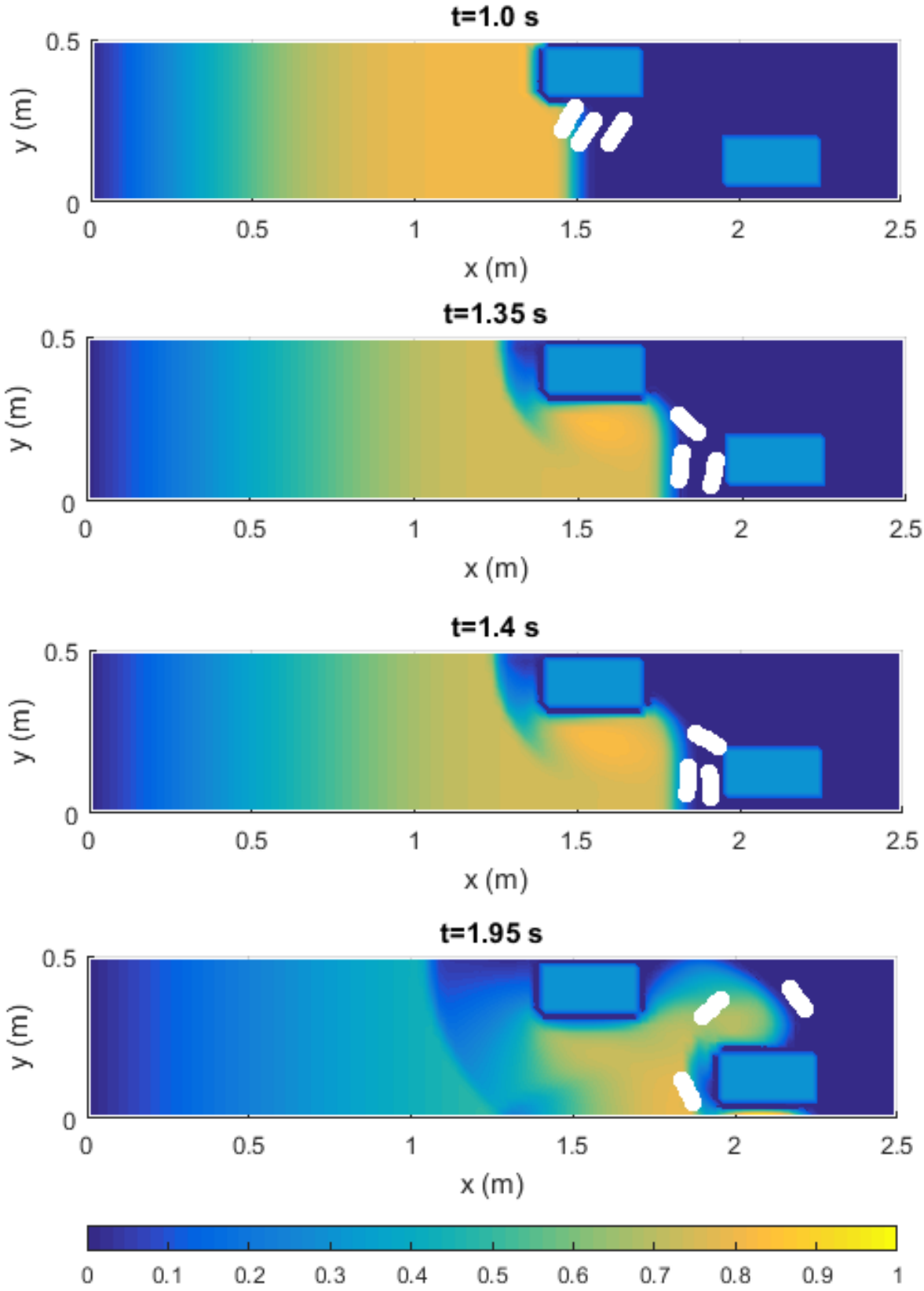

Figure 5.15: 2D Test case 3 - numerical predictions showing object position ($\mathbf{X}_{obj}$ m) and the magnitude of the fluid velocity vector ($|\boldsymbol{u}|$ m/s)

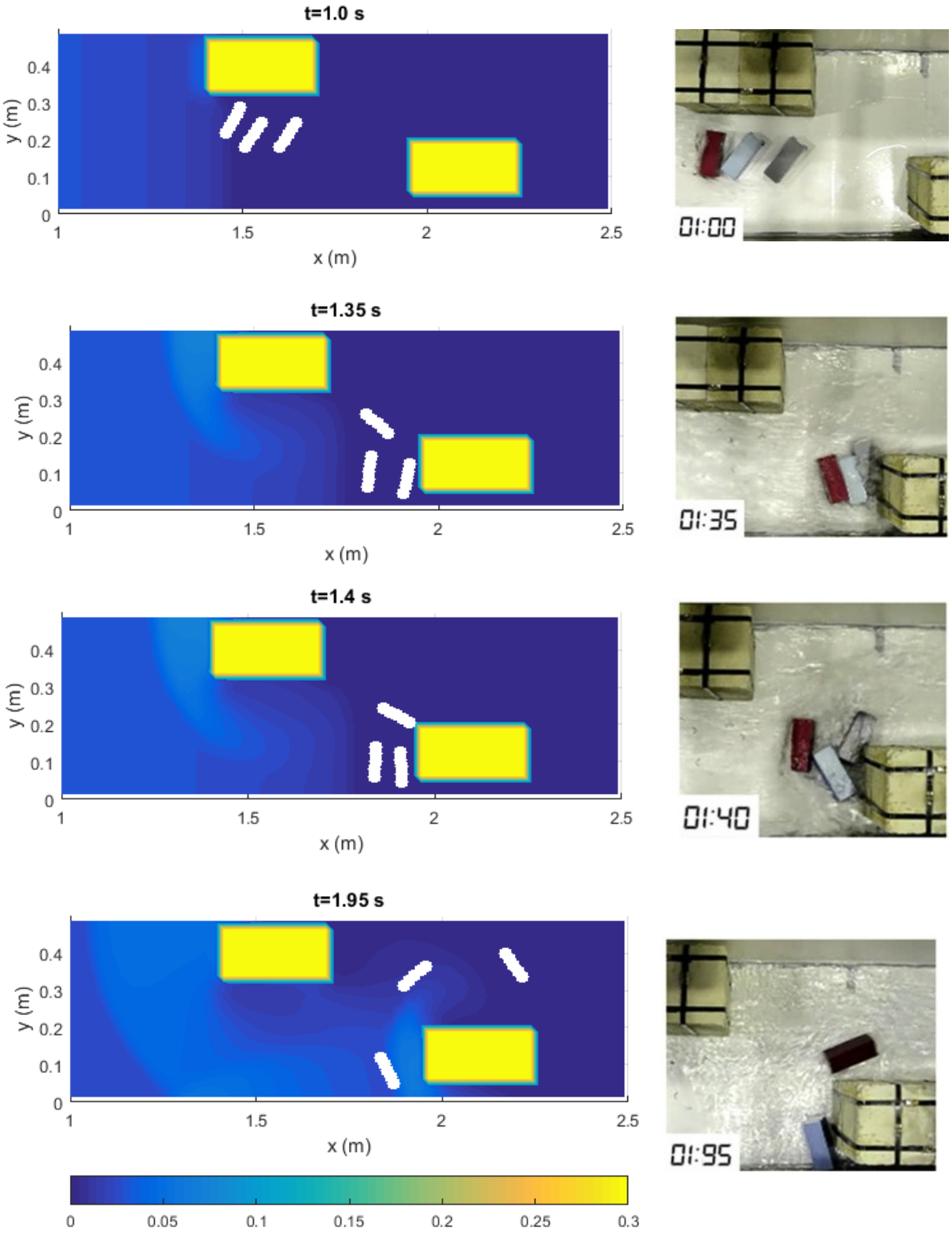

Figure 5.16: 2D Test case 3 - Visual comparison of numerical predictions for object position ($\mathbf{X}_{obj}$ m) and water depth (h m) with experimental observations recorded by Albano et al. (2016).

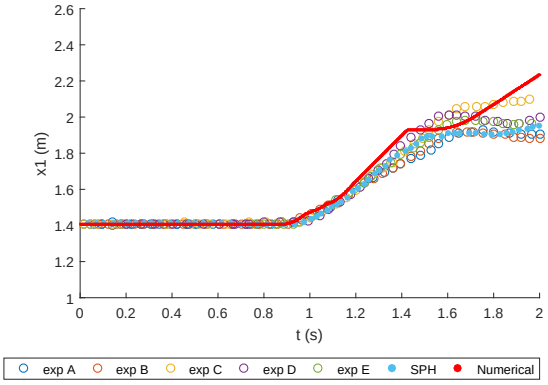

(a) Object 1

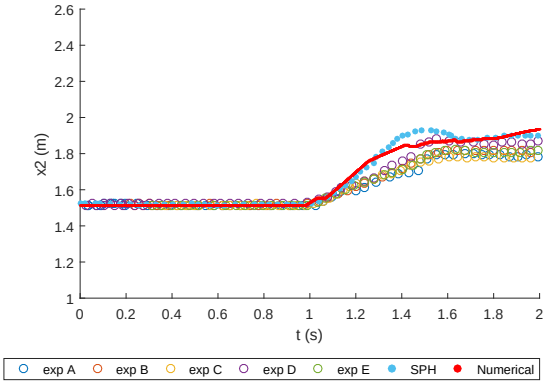

(b) Object 2

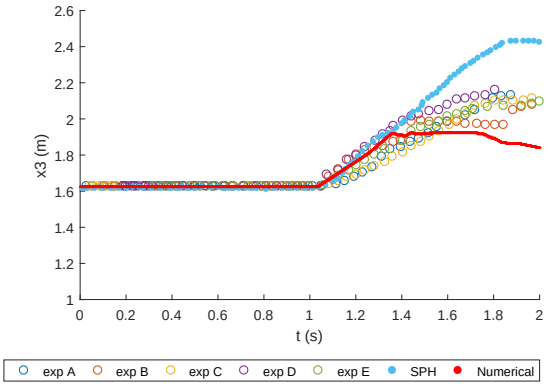

(c) Object 3

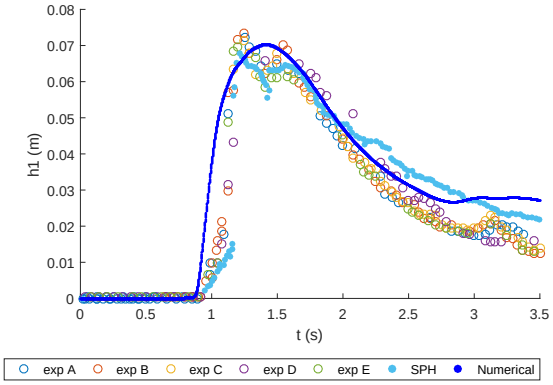

(d) Depth gauge 1

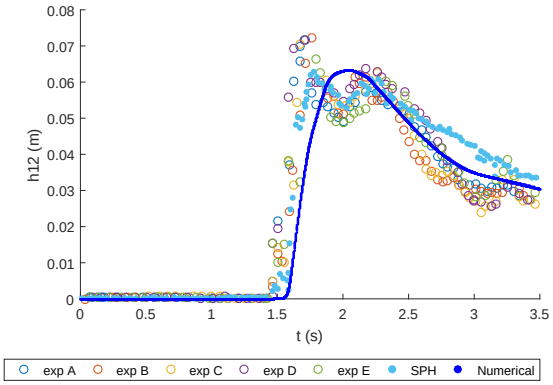

(e) Depth gauge 2

Figure 5.17: 2D Test case 3 - numerical predictions for object x-position (X_{obj} m) and water depth (h m) achieved by the floating debris modelling tool developed in this work. Numerical results are compared against experimental results A, B, C, D and E and SPH model results presented by Albano et al. (2016).

5.3.4 Discussion of results

The results presented here demonstrate that a new 2D floating debris modelling tool developed in this work is able to accurately simulate the entrapment of three parrallellipeds transported by a dam break wave, in the presence of fixed domain obstacles. Visually, the numerical predictions closely match experimental observations. Visual validation is backed-up by acceptable values of RMSE.

In a similar study presented by Albano et al. (2016) numerical modelling is performed using an SPH-based modelling approach. The results presented here are comparable with those achieved by Albano et al. (2016). This is illustrated in Figure 5.17, where results achieved by the floating debris model are compared to those achieved through SPH. However, Albano et al. (2016) identifies the computational cost of SPH modelling as limiting further application; their simulation of the test case presented above resulted in a total computation time of 3 days 9 hours 47 minutes 19 seconds. This study applies a GPU-accelerated finite volume scheme coupled with DEM and results in a total computation time of 33 seconds.

5.4 Conclusion

This chapter has presented a new coupled floating debris modelling tool with improved modelling capability. The new 2D tool predicts depth averaged flow variables and the transport dynamics of axisymmetrical objects with two degrees of translational freedom and rotation about the z-axis. The 2D scheme has been validated for three experimental test cases where objects are transported by a dam break wave past fixed domain obstacles. In all three cases, the model accurately predicts the arrival of the wave front and time evolution of water depths at identified gauge points. The position of the transported debris mass in test cases one and two are well-replicated and for test case three the horizontal position of each object has been both visually and statistically validated to a high level of accuracy. The experimental validation demonstrates that the new coupled floating debris modelling tool presented in this work is able to make accurate predictions of the motion of floating objects transported at a hydraulic flume scale. The results are comparable in accuracy to those presented by Albano et al. (2016), but achieve greatly accelerated computation time.

Chapter 6

Investigating debris processes during flooding in Boscastle 2004

During flash flooding in Boscastle, 2004, assorted floating debris, including a significant number of washed away vehicles, blocked two bridges within the town and were reported to have significantly altered flood stage and extent. In this chapter, the reported impacts of floating debris are investigated further through numerical modelling of the Boscastle flood event. The preceding chapters have presented a new numerical modelling tool for predicting the transport and dynamics of floating debris. Here the new 2D floating debris modelling tool is applied to investigate flooded vehicle transport during flooding in Boscastle.

6.1 Introduction

The flood event that occurred in Boscastle exhibited hydraulics typical of UK flash flooding. This included the transport of a significant cargo of floating debris. Transported objects consisted of tree trunks, vegetation, urban debris and 116 vehicles mobilised during flooding of a riverside carpark. Debris blockages, including at two downstream bridge sites, were concluded to have altered flow paths and caused extensive damage. The Boscastle flood event remains one of the best recorded extreme flood events in the UK (Roca and Davison, 2010) and prompted a number of academic and industry led studies in its aftermath. For this reason flooding in Boscastle provides an excellent resource for investigating floating debris trasport. Records, including a collation of eye witness accounts, photographic evidence and maximum water levels surveyed in the immediate aftermath, provide valuable quantitative and qualitative datasets and have already enabled a number of numerical model reconstructions (HR Wallingford, 2005; Kvočka et al., 2015; Roca and

Figure 6.1: Photograph of Boscastle showing steep-sides catchment characteristics (Cornwall Tour: www.cornwalltour.co.uk/boscastle)

Davison, 2010). Furthermore the availability of information regarding transported vehicles, including the location and capacity of a flooded car park; and the eventual location of washed away vehicles, overcomes difficulties in determining the origin of transported debris.

6.1.1 Catchment characteristics

Boscastle is situated at the mouth of the River Valency on the north coast of Cornwall, illustrated in Figure 6.2a. The town sits within the valley of a small, steep-sided catchment with hillsides rising to the north and south. The catchment covers a total of 20km^2 and, at its highest point, rises to 300m AOD. The steep topography surrounding the town is made evident by the photograph in Figure 6.1, which faces inland from Boscastle's harbour and shows the town straddling the main channel of the Valency. The main channel and its tributaries are bordered by significant areas of woodland (Fenn et al., 2005). As the river passes through Boscastle it runs directly adjacent to a 170 space car park that serves the many tourists visiting Boscastle during the busy summer period. The location of the car park is identified in Figure 6.2b. A tributary to the Valency, the River Jordan enters the town from the south. Two bridges cross the main channel within the town, these are the larger, upstream B3263 road bridge and a smaller, downstream footbridge. Both bridges are identified in Figure 6.2b.

(a) The town of Boscastle situated on the north coast of Cornwall (Google maps)

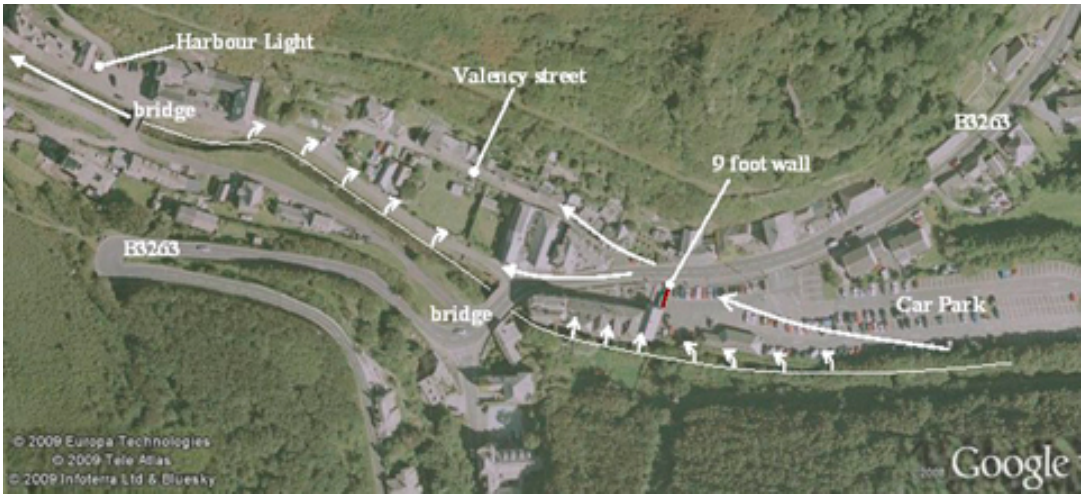

(b) Boscastle town centre - indicating key features and flood flow paths (Roca and Davison, 2010).

Figure 6.2: The town of Boscastle that was hit by flooding on 16th August 2004

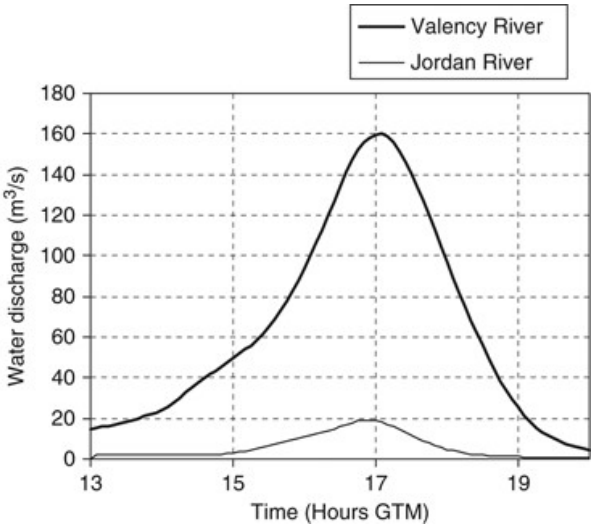

Figure 6.3: Estimated flood hydrograph for the River Valency and River Jordan on 16th August 2004 (Roca and Davison, 2010).

6.1.2 Flooding on 16th August 2004

On 16th August 2004 the town of Boscastle experienced historical flash flooding following extreme heavy rainfall. Approximately 200mm of rain fell over the surrounding catchment within five hours. The intense rainfall combined with steep catchment topography and saturated antecedent soil conditions to produce an estimated 1 in 400 year magnitude flood event. The event lasted from 13:00 BST, when flows in the Valency and its tributaries began to increase, untill 20:00 BST, when water levels had returned to within the river banks (Environment Agency, 2004). Estimated peak discharges of 160 m^3/s in the Valency and 20m^3/s in the Jordan occurred at approximately 18:00 BST (HR Wallingford, 2005).This resulted in a total peak discharge of 180m^3/s in the channel through Boscastle (Roca and Davison, 2010). The flood event hydrograph shown in Figure 6.3 was estimated by HR Wallingford (2005) after the event, through a combination of hydrological and hydraulic event modelling based on rainfall and 'wrack' mark survey data (Roca and Davison, 2010).

Flood hydraulics

The hydraulics observed and recorded during the Boscastle flood event were characteristically 'flashy'. Water depth in flooded streets reached >2m and flow velocities were high (Lhomme et al., 2010). Surface waves, hydraulic jumps and trains of waves were recorded through photographic and video evidence. Numerical predictions reported by Roca and Davison (2010) after the event captured changes in flow regime between subcritical and

supercritical conditions. The B3263 road bridge was almost entirely blocked by entrained debris during the initial stages of the flood. This caused flow diversion to four main overland pathways (Roca and Davison, 2010). Observers reported seeing "walls of water", which described rapid short term stage rises (between 1m and 1.5m) within periods of seconds or miunutes (Fenn et al., 2005). Initial suggestions that the sizeable and rapid stage rise had been caused by the failure of temporary debris dams were later discredited by HR Wallingford (2005). It was concluded, through hydrodynamic modelling, that the more-likely cause was the rapid blockage of bridges or the collapse of a 2.7m wall adjacent to Boscastle car park (HR Wallingford, 2005). The wall collapsed at approximately 16:30 BST (Environment Agency, 2004). Its position is identified in Figure 6.2b.

Floating debris processes

Floating debris played a significant role in flooding on 16th August. During the event, eyewitnesses reported sizeable debris dams that formed in the upper reaches of the catchment and a significant quantity of floating debris transported downstream. Large quantities of washed-out trees, vehicles and other trash accumulated at both the B3263 road bridge and downstream footbridge within the town. At the time of the flood, visitors' cars almost filled the 170 space car park situated towards the east of the town and directly north of the Valency, illustrated in Figure 6.2b (Environment Agency, 2004). At 15:45 BST parked vehicles in the flooded car park began to float. At 16:10 BST vehicles were carried through the town by flood water. In total 116 vehicles were washed away, 84 of which were later recovered from the streets, gardens and harbour of Boscastle; 32 were washed out to sea. Figure 6.4a shows a number of vehicles being washed towards the location of the B3263 bridge. Video footage of the event shows whole trees being washed under the opening of the B3263 bridge. At around 16:10 BST the main B3263 road bridge was blocked by debris, causing water levels upstream to rise rapidly (Environment Agency, 2004). It is likely that some debris initially began to accumulate at the upstream face of the bridge opening, afterwhich progressive blockage took place quickly (HR Wallingford, 2005; Roca and Davison, 2010). At 16:15 BST the main road bridge became impassable. Evidence suggests that flow through the smaller aperture of the downstream footbridge was more or less running freely until a vehicle transported by flood waters became trapped against the upstream face (HR Wallingford, 2005). A red car almost entirely blocked the bridge opening and continued to amass further debris for the remainder of the event (Rowe, 2004). The eventual blockage of the downstream footbridge is shown in Figure 6.4b, the photograph was taken after flood waters had receded.

(a) Flooding and transported vehicles at the B3263 bridge (Fire Brigade)

(b) Debris accumulated at the downstream bridge (Mike Metcalfe, 21:14 BST)

Figure 6.4: Photographic evidence of flooding and debris at the B3263 road bridge and downstream footbridge sites in Boscastle (HR Wallingford, 2005)

Damage

Though there were significant damages to infrastructure in surrounding catchments, the most damage occured within the Valency catchment and particularly within Boscastle itself. Over 70 properties were flooded (HR Wallingford, 2005). In total 100 properties and businesses were effected by the flood (Roca and Davison, 2010). There was significant damage to buildings, road surfaces and bridges; four buildings in Boscastle were later demolished as a result (Lhomme et al. (2010)). The flood damaged water, drainage and electricity supply networks causing interruptions to these services (HR Wallingford, 2005).

6.2 Observed data

The event in Boscastle took place during daylight hours on a busy summer's day. The 16th August falls within most authorities' school holidays so the town was especially busy with visitors taking photos and videos. After the event, the Environment Agency were commended for performing a swift post-event survey and collating eye-witness acounts (HR Wallingford, 2005).

'Wrack' mark data

Of the data collected by the Environment Agency, a series of 'wrack marks' provide a valuable indication of peak water levels during the event. The marks are left by flood-borne trash, suspended sediment and residue usually deposited against vertical surfaces such as walls. The Environment Agency surveyed a total of 72 'wrack marks'. The location

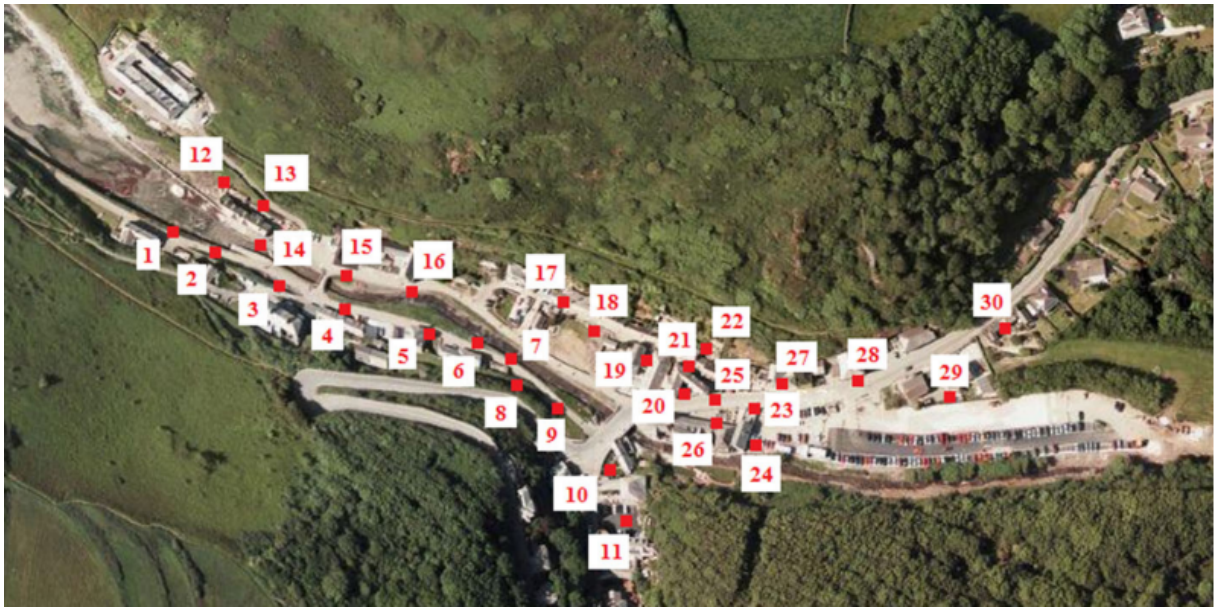

Figure 6.5: The location of 'wrack' mark data points within Boscastle (Kvočka et al., 2015)

of 30 marks within Boscastle town centre are illustrated in Figure 6.1 and the nature of each marking is described in Table 6.1. 'Wrack mark' data was used by HR Wallingford (2005), Lhomme et al. (2010) and Kvočka et al. (2015) as a means of validating numerical model predictions. However there are a number of sources of error associated with 'wrack mark' data. Typically deposited material can span $\pm 15cm$ vertically (Horritt et al., 2010). Horritt et al. (2010) also stress difficulty in identifying maximum trash marks, as several distinct lines may be observed in the same location. The magnitude of the resulting error may be in the order of metres (Horritt et al., 2010). For a flash flood event like Boscastle, surface waves may deposit residue at levels higher than the actual maximum water level. In such cases the wrack mark may overestimate water depth. Table 6.1 describes the origin of each of the 30 'wrack marks'. Figure 6.5 shows the location of each data point on a map of Boscastle. According to Table 6.1, a number of the 30 marks were recorded by Boscastle residents. An additional, human error may therefore arise where data was not collected by a trained professional. For flooding in Carlisle 2005, Horritt et al. (2010) suggest an average uncertainty of $\pm 50cm$, however for flash flooding in Boscastle, no estimates as to data uncertainty are available.

Flood extent data

HR Wallingford (2005) collated much of the available data including a map of flood extent produced by the engineering consultancy Halcrow. Figure 6.6 shows the surveyed flood

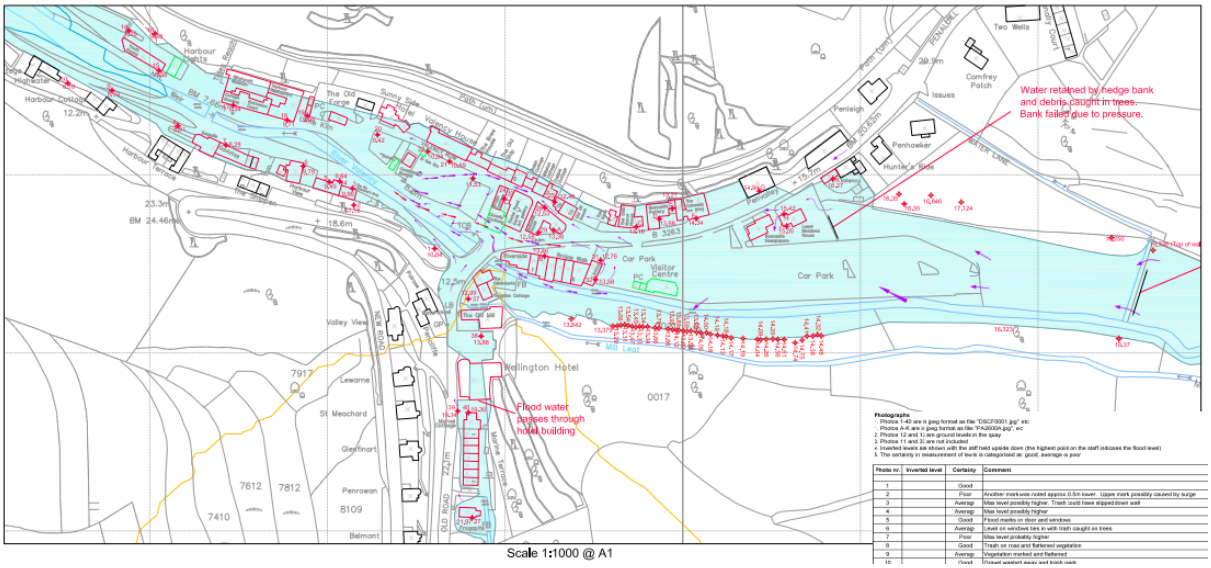

Figure 6.6: Flood extent as surveyed by Halcrow (HR Wallingford, 2005)

extent within the town centre.

Timeline data

Using eye-witness accounts, Environment Agency (2004) produced a timeline of events between 12:00 BST and 21:00 BST on 16th August 2004. Of the information provided, key events related to flood hydraulics and floating debris transport are highlighted in Figure 6.7. All times are approximate and subject to variation. Environment Agency (2004) record the time of peak flows as 17:00 BST, whereas HR Wallingford (2005) and Fenn et al. (2005) estimate peak flows to have occurred in Boscastle at 18:00 BST.

6.3 Numerical modelling of the Boscastle event

The blockage of two bridges by washed-away vehicles and flood debris was a major feature of flooding on 16th August 2004. Not only did these blockages alter the eventual flood pathways but sudden blockage by vehicles may have caused the "walls of water" reported by onlookers. To investigate flood extent and dynamics of the Boscastle event, hydrodynamic modelling is performed using data provided by colleagues at Cardiff University. A finite volume Godunov-type hydrodynamic scheme, developed at Newcastle University is applied to model the event. To investigate the effect of debris blockages at the two bridge sites, two alternative scenarios are tested:

1. **No blockage** - The apertures of both bridges in Boscastle are assumed to be fully

Timeline of events during Boscastle flood:

All times are relative to British Summer Time (BST)

- **13:00** Flows in Valency and tributaries begin to increase
- **15:15** Valency at Boscastle almost full after three hours of extreme rainfall
- **15:30** Valency begins to spill over north bank between the two bridges
- **15:45** Cars in car park start to float; water on B3263 a few inches deep
- **16:00** Witnesses see 3m wall of floodwater sweep across car park into Visitor Centre; deep, fast-flowing water makes B3263 impassable
- **16:10** Main road bridge blocked by debris, causing water levels upstream to rise rapidly; water levels on car park rise and cars start to be carried through village by floodwater
- **16:15** Flooding on Jordan worsens; main road bridge impassable
- **16:30** High wall by car park collapses, sending water surging down B3263; witnesses see another wall of water crash into Visitor Centre, smashing its doors; water from Jordan starts to pour through Wellington Hotel; cars and other large debris washed down either side of Riverside Hotel
- **17:00** Floods at their peak; cars washed down from car park
- **18:00** Floods started to recede
- **20:00** Water levels back within river banks

Figure 6.7: Summary of key events during flooding in Boscastle 2004, using information recorded by Environment Agency (2004)

clear and water is allowed to flow through freely for the duration of the event.

2. **Full blockage** - The apertures of both bridges are assumed to be fully blocked, allowing no flow to pass through, for the duration of the event.

The new floating debris modelling tool developed in this work is well-suited for investigating the dynamics of floating debris during flooding in Boscastle. Therefore an additional application is also presented here. The new floating debris modelling tool is applied to investigate the transport of 116 flooded vehicles from Boscastle's riverside car park. This yields scenario 3:

3. **Modelling floating vehicles** - Vehicle transport is modelled by applying the new floating debris modelling tool. This is achieved by initially placing 116 modelled vehicles within the riverside car park.

6.3.1 Description of the numerical models

For scenarios 1 and 2 described above, a 2D finite volume Godunov-type hydrodynamic scheme is applied. The modelling scheme has been developed at Newcastle University (Liang, 2010) and extensively validated for a variety of flow conditions that share hydrodynamic similarities with flash flooding (Liang et al., 2016). The numerical methods employed by this modelling tool have been described in detail in Chapter 3 and are not repeated here. Scenario 3 is modelled using the new 2D floating debris modelling tool presented in this work. The numerical methods and model coupling employed by this tool have been described in Chapters 3, 4 and 5. The floating debris modelling tool has been validated for 1D and 2D dam break applications which can be considered hydrodynamically similar to flash flood dynamics.

Study domain

The study area is shown in Figure 6.2b. It extends 665m from east to west and 235m from north to south. Surface elevations are obtained from a digital terrain model (DTM) that has been adjusted to incorporate cross sectional data for the River Valency and River Jordan (Kvočka et al., 2015). The domain is discretised into a cartesian grid with spacing $\Delta x = 1m$, $\Delta y = 1m$. As the model is 2D, the vertical dimensions of bridge openings are not automatically handled. Instead, adjustments are made to the DTM to account for blockage dimensions. For scenario 1 and 3, the presence of the B3263 road bridge and lower footbridge are ignored by the model. Therefore terrain data at the two bridge sites corresponds to the channel bed. For scenario 2, the DTM is adjusted to account for full

blockage at both bridges. Terrain elevations at the bridge sites are increased to level with the road surface.

Roughness

The roughness of a flooded area is described by Manning's coefficient (n). A higher value of n describes a rough surface and has the effect of reducing velocity and consequently increasing stage. A lower value of n describes a less rough surface such as hard-standing, which is less reductive to flow velocity. Studies performed by HR Wallingford (2005) applied spatially varying values for Manning's roughness to the Boscastle domain. Values varied from the lowest value of $n = 0.025s/m^{1/3}$, for flow over the B3263 road to a highest value of $n = 0.125s/m^{1/3}$ for flow over the left floodplain. For the main channel a value of $n = 0.04s/m^{1/3}$ was applied. However, Kvočka et al. (2015) argued that within the relatively short river reach affected by flooding in Boscastle, variations in roughness coefficient would not significantly affect flood level. Kvočka et al. (2015) applied an averaged Manning's value of $n = 0.04s/m^{1/3}$ over the Boscastle domain and was able to successfully predict peak flood levels. Kvočka et al. (2015) further investigated the effect of increasing Manning's n over the entire domain. When n was increased within reasonable limits there was little effect on results. For this study a uniform Manning's roughness coefficient $n = 0.04s/m^{1/3}$ is applied over the entire computational domain.

Boundary conditions

Flooding in Boscastle was contributed to by high flows in the River Valency and Jordan. An estimated flood hydrograph is included in Figure 6.3. Although flow in the Jordan also peaked at 18:00 BST, the flood hydrograph shows that the River Valency made the greatest contribution to peak flow through Boscastle. When modelling the Boscastle event, Kvočka et al. (2015) negated flow in the river Jordan and accurately recreated peak flood levels at 30 'wrack' mark locations. For this study, flow in the River Jordan is also neglected. As a result only one inflow boundary is allocated within the study domain. An inflow hydrograph governs time-dependent flow entering the domain through cells along the eastern boundary. At the western domain boundary outflow conditions are specified. At the western domain boundary the River Valency meets the sea. Tide levels at the mouth of the Valency varied during the event. At flood peak the tide was approximately 0.8m AOD and reached a high tide of 3.5m approximately 1h hour later (Kvočka et al., 2015). However, according to HR Wallingford (2005) tidal variances did not affect the flooding of Boscastle. Therefore, as with similar studies (Kvočka et al., 2015; Roca and

Davison, 2010) the downstream boundary condition is fixed at 3.5m AOD for the duration of the simulation.

6.4 Investigating blockage impact

The 2D finite volume Godunov-type hydrodynamic scheme predicts water depth and depth averaged velocity for each domain cell. Additionally the Froude number (Fr) for each cell is calculated through post model analysis. The Fr number indicates the regime of open channel flow where $Fr < 1$ describes subcritical flow, $Fr = 1$ describes critical flow and $Fr > 1$ describes supercritical flow. For a single cell, the Froude number is calculated by:

$$Fr = \frac{|\boldsymbol{u}|}{\sqrt{gh}} \tag{6.1}$$

where $|\boldsymbol{u}|$ is the velocity magnitude and h is water depth. Equation 6.1 results in a dimensionless quantity and therefore has no units.

6.4.1 Scenario 1 - no bridge blockage

Outputs of the hydrodynamic model are shown in Figure 6.8. As no blockage is included in this modelling scenario, flow in the main channel remains unimpeded for the duration of the simulation. The flood extent shown in Figure 6.8 shows a good likeness to findings from a flood extent survey presented by HR Wallingford (2005) and included in Figure 6.6. However as flow in the River Jordan is not considered in the simulation, flooding to the south of Boscastle through the Jordan valley is not captured. Figure 6.8a shows predicted water depths at the flood's peak. The greatest depths are present in and adjacent to the main channel. An area of deep water is also evident on the B3263 road to the north of the channel. Figure 6.8b shows the predicted velocities at the flood's peak. High velocities are evident in the channel and in the car park to the east of the domain. Figure 6.8c shows the corresponding Froude number for each cell, as calculated using Equation 6.1. Predicted flow regimes vary between subcritical and supercritical conditions and are therefore concurrent with results presented by Roca and Davison (2010). There are evidently a high number of transitional regions where transcritical hydraulic features occur. The results presented in Figure 6.8c demonstrate that flooding in Boscastle was a characteristically 'flashy' event.

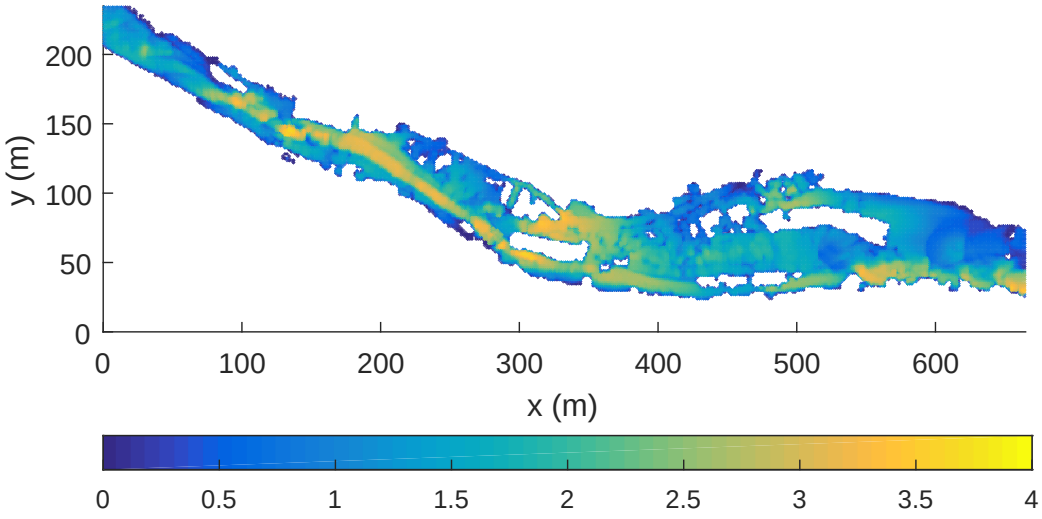

(a) Predicted water depth, h at flood peak (m)

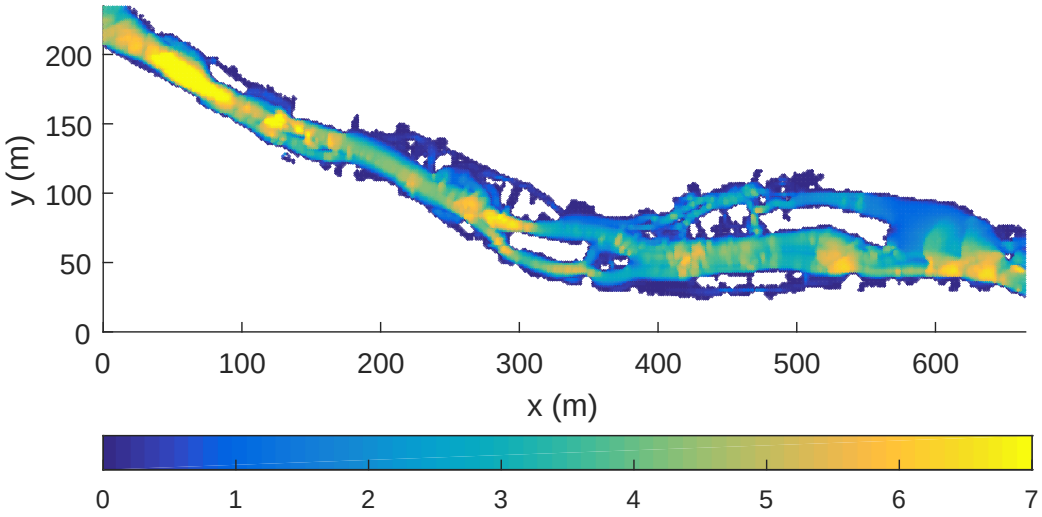

(b) Predicted velocity magnitude, $|\boldsymbol{u}|$ at flood peak (m/s)

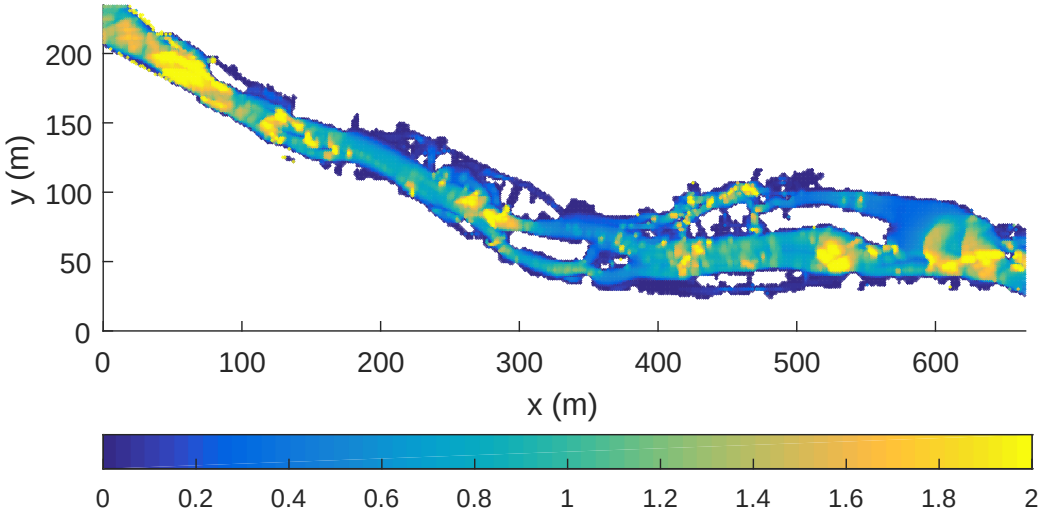

(c) Predicted Froude number, Fr at flood peak

Figure 6.8: Scenario 1 (no blockage) - numerical results

6.4.2 Scenario 2 - full bridge blockage

Figure 6.9 shows the model results for scenario 2. Both bridges have been modelled as fully blocked for the duration of the simulation. Figure 6.9a shows water depth at the peak of the flood. Two areas of increased water depth are evident in Figure 6.9a that were not predicted for scenario 1. Immediately upstream of the B2363 road bridge and the lower footbridge water depth is elevated. The corresponding velocity at these points, shown in Figure 6.9b is lower than its surroundings, demonstrating the effect of bridge afflux. Figure 6.9c illustrates the predicted Froude numbers at peak flow. Numerical results for scenario 2 predict a number of additional regions of supercritical flow within the car park and over the blocked B3263 road bridge. Figure 6.10 shows the predicted change (positive or negative) between results for scenario 1 and scenario 2. Figure 6.10a shows two areas of increased water depth surrounding the B3263 road bridge and the downstream footbridge. Additionally Figure 6.10b shows increased velocity and a corresponding increase in Froude number (Figure 6.10c) at the locations of the two bridges where the elevated channel bed forces flow over the road surface.

Water depths at the 30 'wrack' marks have been predicted for both scenarios and are compared to observed data in Figure 6.11. At the 'wrack' locations, bridge blockage does not appear to significantly affect depth. At mark 8 on the north bank, the numerical models slightly under predict water depth. Likewise, at marks 19, 22 and 23 on the south bank, both numerical models over predict water depth by $> 1m$. There are a number of sources of error associated with 'wrack mark' data that may have contributed to these errors in results. This has been discussed previously. Additionally, discrepancies between numerical and observed results may be due to domain discretisation within the numerical scheme. The domain is divided into a grid of cells containing flow variables. Between the cells ground elevations are interpolated. Where vertical surfaces such as walls are encountered, the model interpolates terrain elevation resulting in a computed sloping surface rather than vertical. As many of the 'wrack' marks have been recorded at walls this error is likely to have affected results. Reducing the grid size would reduce this source of error.

6.5 Investigating vehicle transport

6.5.1 Modelling approach

To model debris transport for scenario 3, the new 2D floating debris modelling tool, presented in Chapter 5 is applied to the Boscastle event. An assortment of natural and

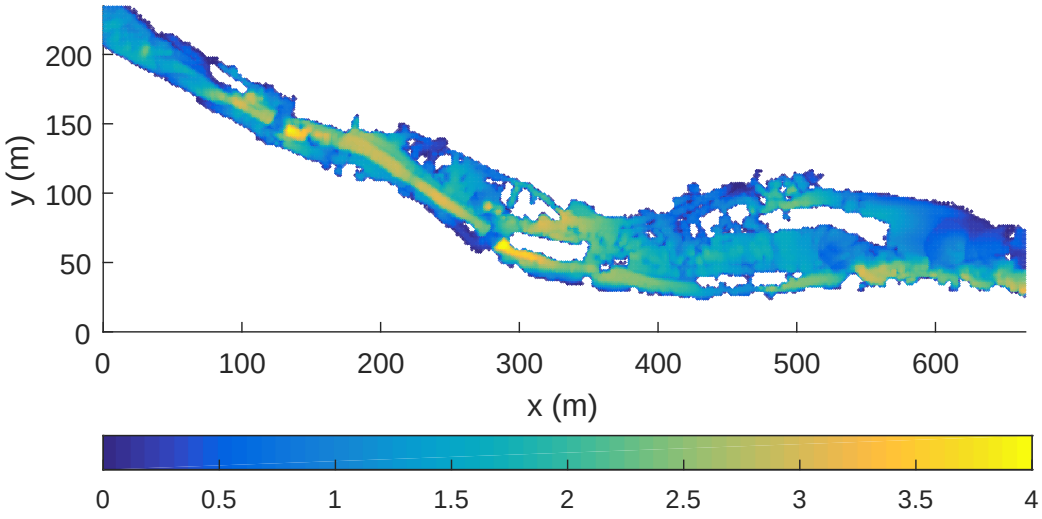

(a) Predicted water depth, h at flood peak (m)

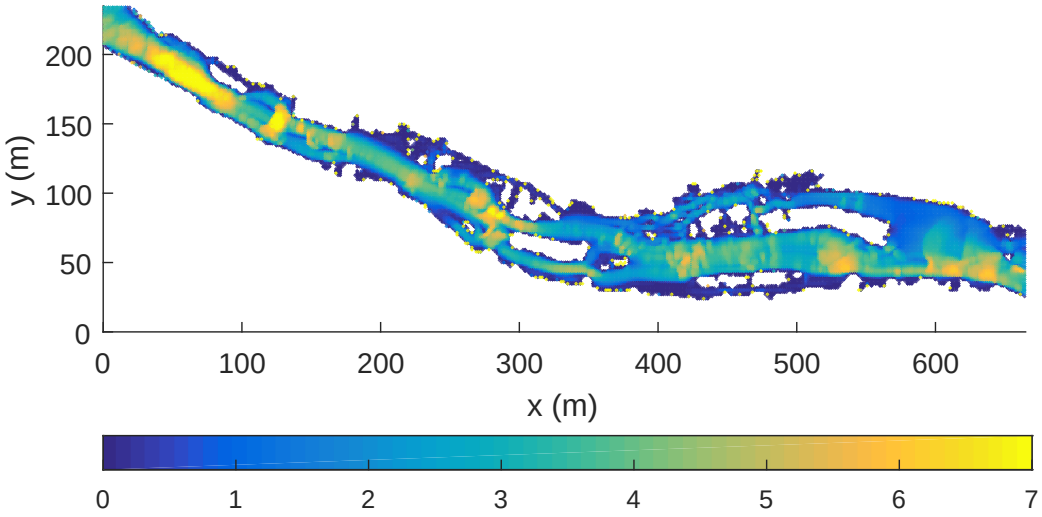

(b) Predicted velocity magnitude, $|\boldsymbol{u}|$ at flood peak (m/s)

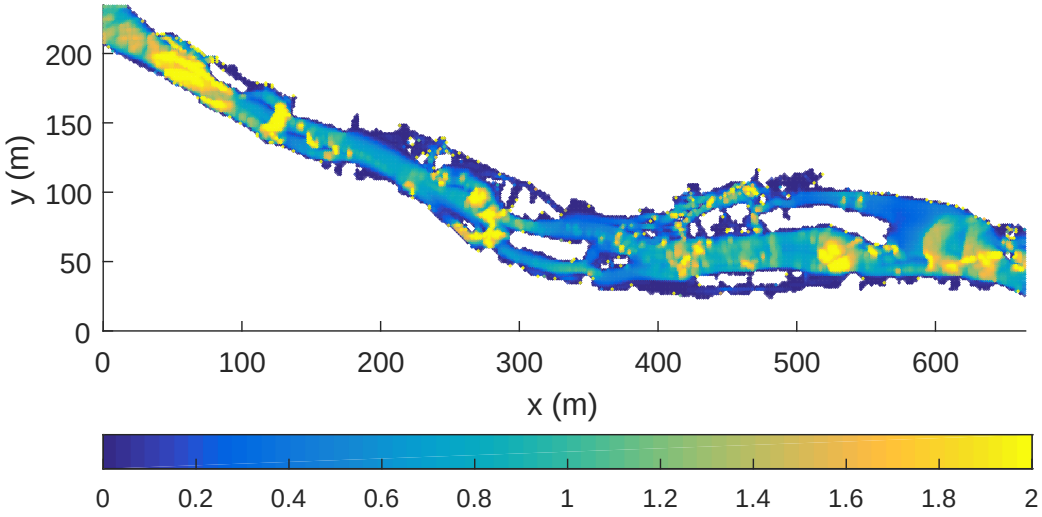

(c) Predicted Froude number, Fr at flood peak

Figure 6.9: Scenario 2 (full blockage) - numerical results

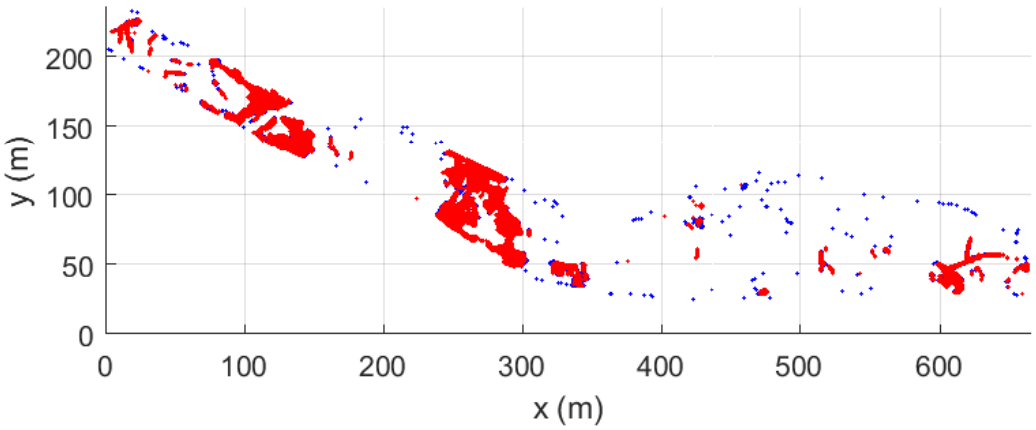

(a) Predicted change in water depth, h due to bridge blockage

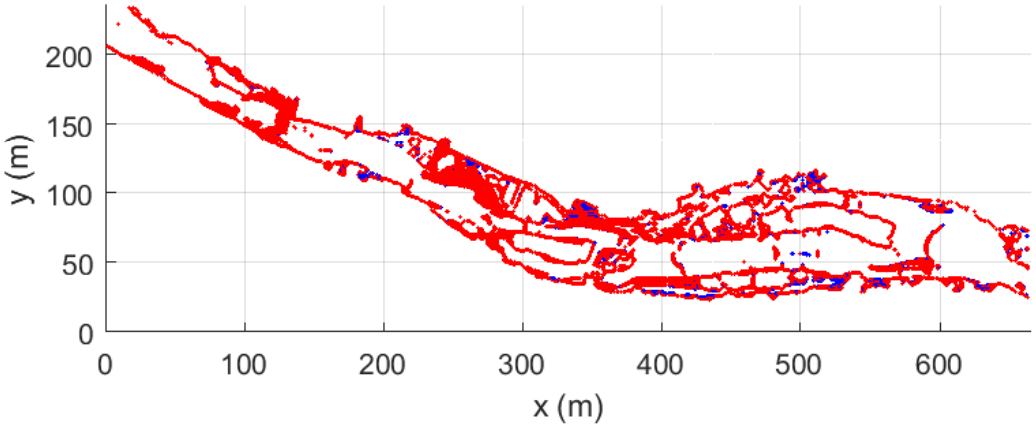

(b) Predicted change in velocity $|\boldsymbol{u}|$ due to bridge blockage

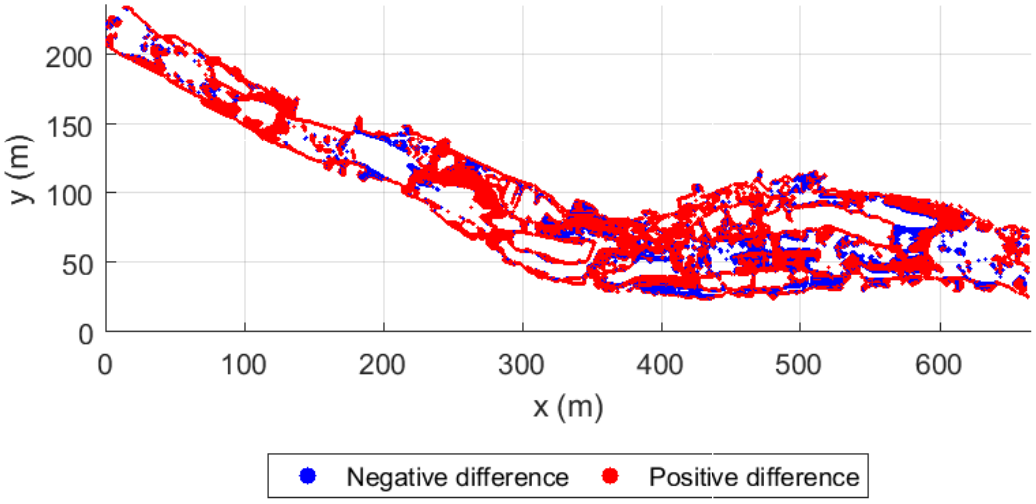

(c) Predicted change in Froude number, Fr due to bridge blockage

Figure 6.10: A comparison between results for scenario 1 and 2. A positive change indicates an increased value caused by bridge blockage. A negative change indicates a decreased value caused by bridge blockage.

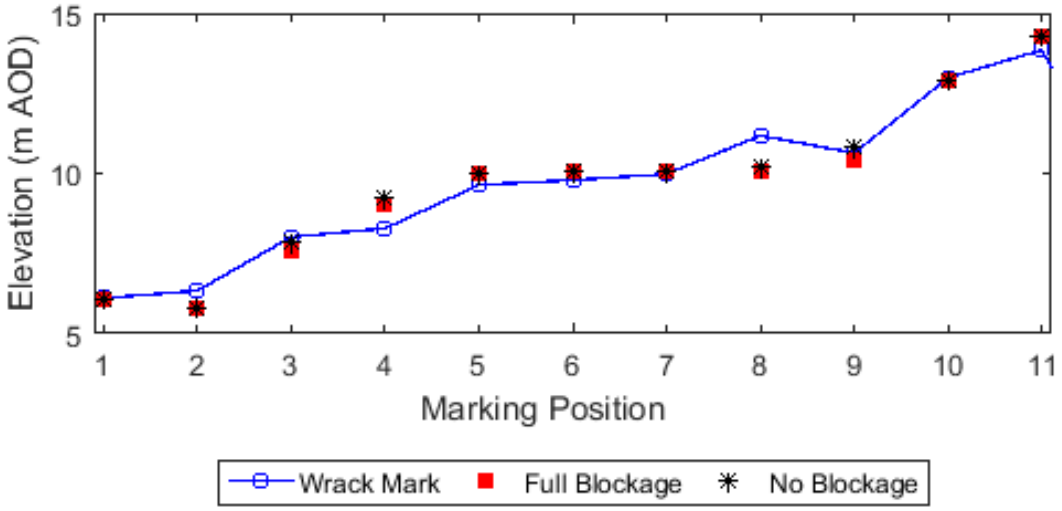

(a) North bank

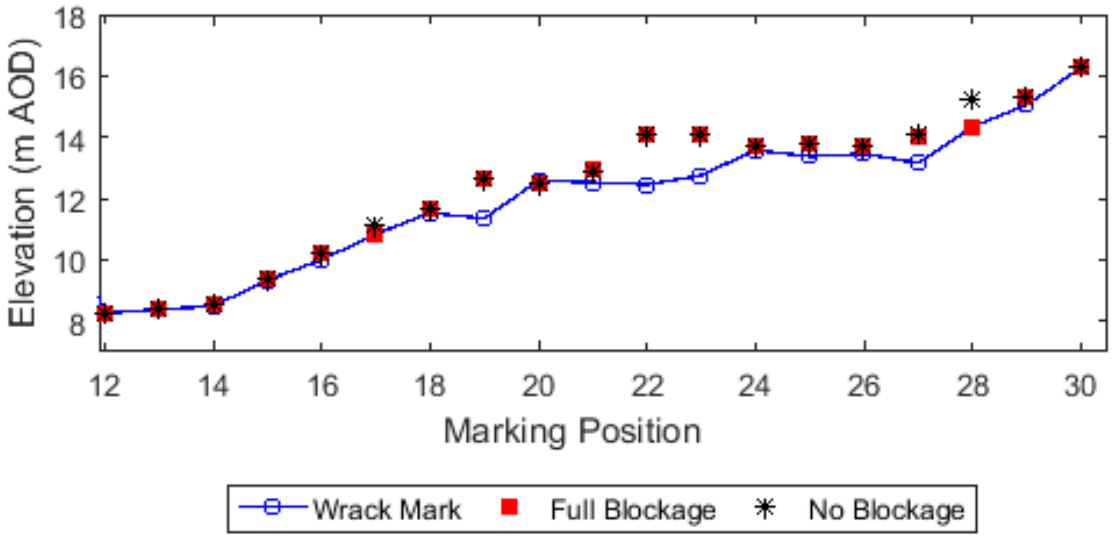

(b) South bank

Figure 6.11: 'Wrack mark' data

anthropogenic debris were transported during flooding in Boscastle including vehicles from the visitors car park. Washed away vehicles contributed substantially to bridge blockage during the event (HR Wallingford, 2005; Rowe, 2004), therefore analysing vehicle transport is considered a valuable exercise. For the well-documented Boscastle event, reasonable estimates of vehicle characteristics and initial conditions can be easily made.

Figure 6.12 shows the visitors car park in Boscastle. The car park has a capacity of 170 spaces and on 16th August 2004, was "almost full" with visitors' cars (Environment Agency, 2004). In total 116 vehicles were transported by flood waters therefore 116 vehicles are modelled for scenario 3. Prompted by the Boscastle event, Shu et al. (2011) and Xia et al. (2011) investigated the incipient transport conditions of flooded vehicles. In both studies three vehicle types were investigated; A Mini Cooper, BMW M5 and Pajero Jeep. During flooding in Boscastle, a number of vehicle types were transported, however in this study, all modelled vehicles are assumed to be the same and share the same material properties as the BMW M5. Vehicle shapes are approximated by three spheres of equal size joined along a horizontal axis. The parameters applied to model a BMW M5 are presented in Table 6.2. Physical vehicle dimensions are found from Shu et al. (2011); Xia et al. (2011). Where values are not available in literature, reasonable estimates have been made by comparing to experimental results for other vehicle types. The moment of inertia about the vertical z axis has been estimated based on measured values for a range of vehicle types presented by Heydinger et al. (1999). Normal and tangential stiffnesses are estimated based on measured values for vehicle collision (Batista, 2006; Kostek and Aleksandrowicz, 2017). Damping is applied at a ratio $\zeta = 0.3$ of critical damping.

To speed computation for the initial flood stages, the visitors car park is initialised as empty. According to the event timeline shown in Figure 6.7 (Environment Agency, 2004), vehicles began to float in the car park at 15:45 BST. This corresponds to 9900s into the simulation. Therefore at t=9900s, 116 vehicles are initialised within the riverside car park. An aerial view of the riverside car park, showing available parking spaces is shown in Figure 6.12. The positions of 116 modelled vehicles have been estimated within the existing parking spaces in Figure 6.12. The initial positions of modelled vehicles at t=9900s are shown in Figure 6.13.

6.5.2 Scenario 3 - Modelling floating vehicles

Figure 6.14 shows numerical outputs for vehicle position and water depth. At t=9900s, water in the flooded car park begins to mobilise some of the 116 modelled vehicles. Figure 6.15 shows a photograph taken during the event of vehicles in the car park beginning to float. The car park is evidently filled with vehicles ranging in size, including camper vans

Figure 6.12: A recent aerial view of the car park in Boscastle that flooded, washing away 116 vehicles. (Google Maps, 2018)

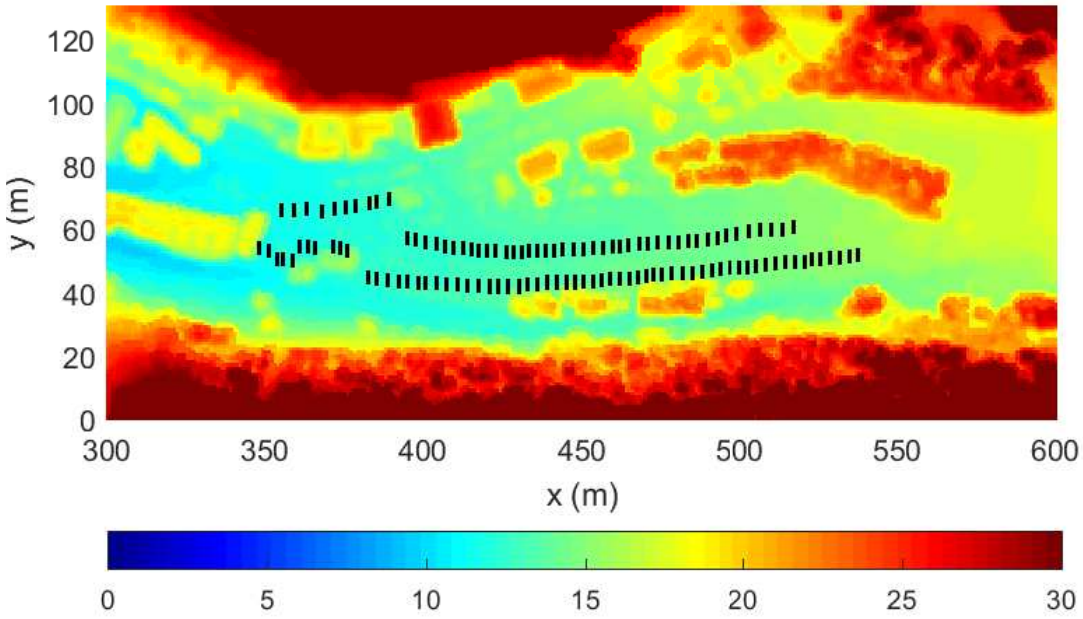

Figure 6.13: Initial positions for 116 modelled vehicles initialised over the Boscastle DTM (m AOD)

and a minibus. However, within the numerical model, all vehicles are assumed to be the same size. Figure 6.16 shows the numerical predictions of the initial moments of vehicle transport. The predictions in Figure 6.16 compare well to the photograph in Figure 6.15. The model simulates vehicles translating and rotating from their initial parking spaces, and colliding with other parked cars. Once mobilised, the model predicts that vehicles are transported downstream into the town, as shown in Figure 6.14b. According to the event timeline presented in Figure 6.7, vehicles and debris were washed either side of the Riverside Hotel. The Riverside Hotel is identifiable at approximately x=300m, y= 70m within the computational domain. The River Valency passes to the south of the hotel, however during the 2004 event, flood waters and debris passed to the north and south, isolating the building within the floodwaters. The numerical model also predicts that transported vehicles take two distinctive pathways, shown in Figure 6.14c. Vehicles parked towards the north of the car park are transported onto the B3263 and travel to the north of the Riverside Hotel. Whereas, vehicles parked towards the south of the car park are washed into the main channel of the Valency and travel on the southern side of the Riverside Hotel. The model predicts frequent collisions between floating vehicles and the surrounding buildings. In particular, the eastern face of the Riverside Hotel suffers impact from a large number of cars washed from the car park. Figure 6.17 shows the western face of the Riverside Hotel during the flood. In the background, vehicles are clearly visible floating from the riverside car park along the B3263 road. To the front of the Riverside Hotel a mass of vehicles rotate with the current. The numerical results, shown in Figure 6.18 show vehicles transported along the B3263 towards the front of the Riverside Hotel where they undergo substantial rotation.

According to the event timeline (Figure 6.7) cars began to float at 15:45 BST and at 16:10 cars started to be carried through the town by floodwater. It, therefore, took 25 minutes from initial floating before vehicles were transported away from the car park. This timeline is not captured by the numerical model, which predicts that vehicles begin to move within seconds of initial floating. During the simulated event, none of the vehicles become permanently lodged at either of the two bridges. Instead vehicles travelling along the main channel are washed straight through the opening. Figure 6.14c shows a vehicle within the main channel that is being washed towards the location of the second, lower bridge. The western most vehicle in Figure 6.14c is not simulated to become entrapped. However the model outputs are still valuable as they indicate well the pathways taken by washed away vehicles. Further model development is required to more accurately capture incipient transport processes and blockage mechanisms.

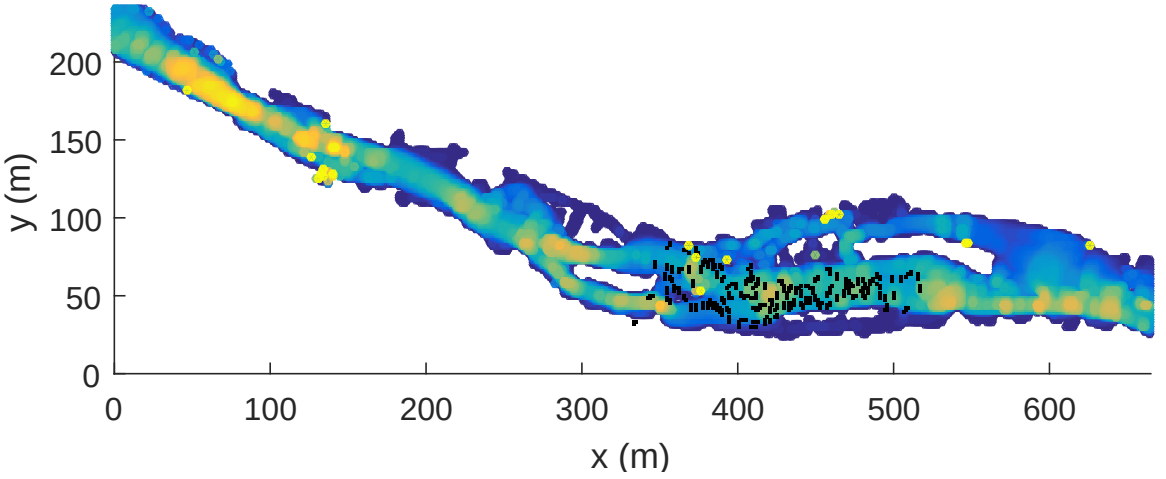

(a) t=9910s

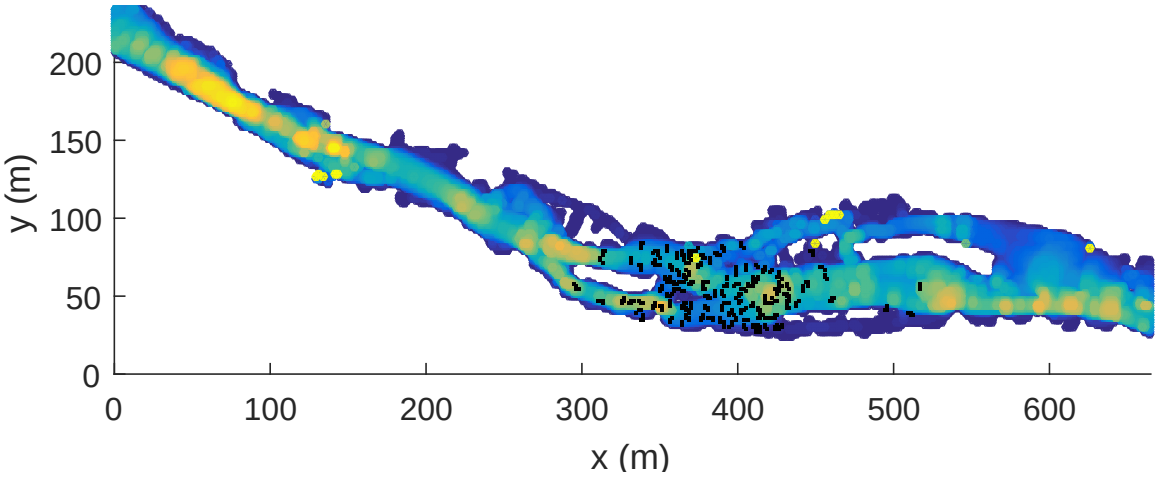

(b) t=9930s

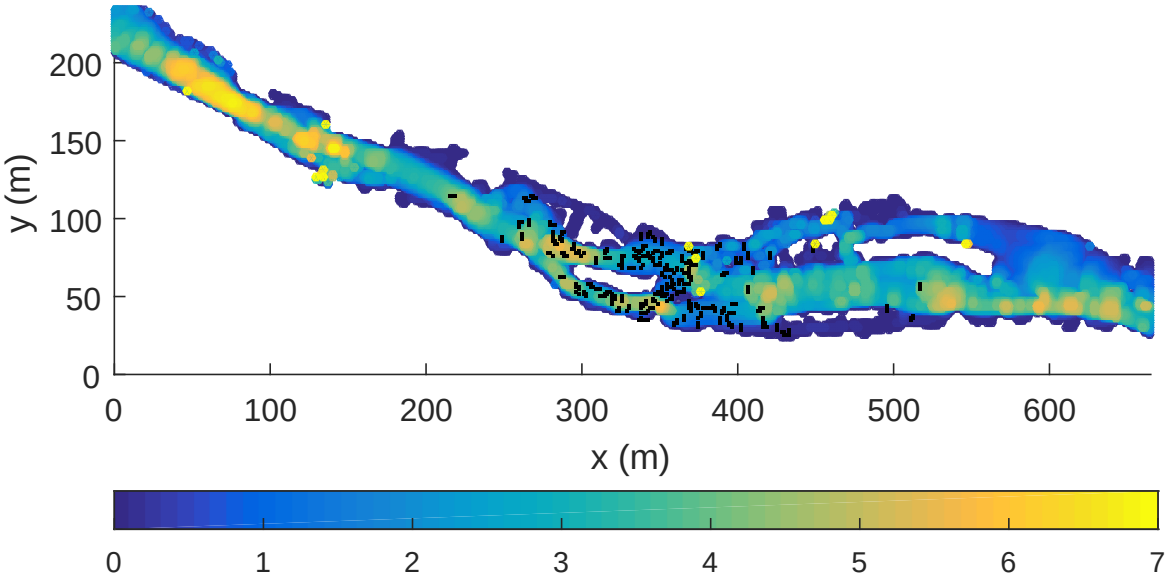

(c) t=9960s

Figure 6.14: Scenario 3 (Modelling floating vehicles) - numerical results for object position and velocity magnitude (m/s)

Figure 6.15: "Cars and camper vans float around Boscastle car park after the River Valency burst its banks." Photograph taken by Don Stollery. (Rowe, 2004)

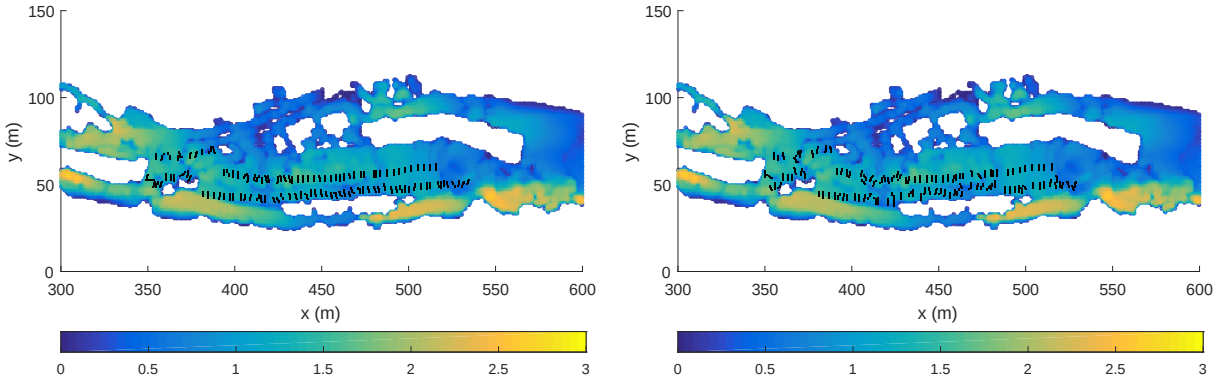

(a) t=9901s

(b) t=9902s

(c) t=9903s

(d) t=9904s

Figure 6.16: Simulated vehicles in flooded car park - numerical results for object position and water depth (m)

Figure 6.17: "As the flood waters reach a pinnacle, by the Riverside Hotel a log-jam of vehicles swirls in the torrent." Photograph taken by Don Stollery. (Rowe, 2004)

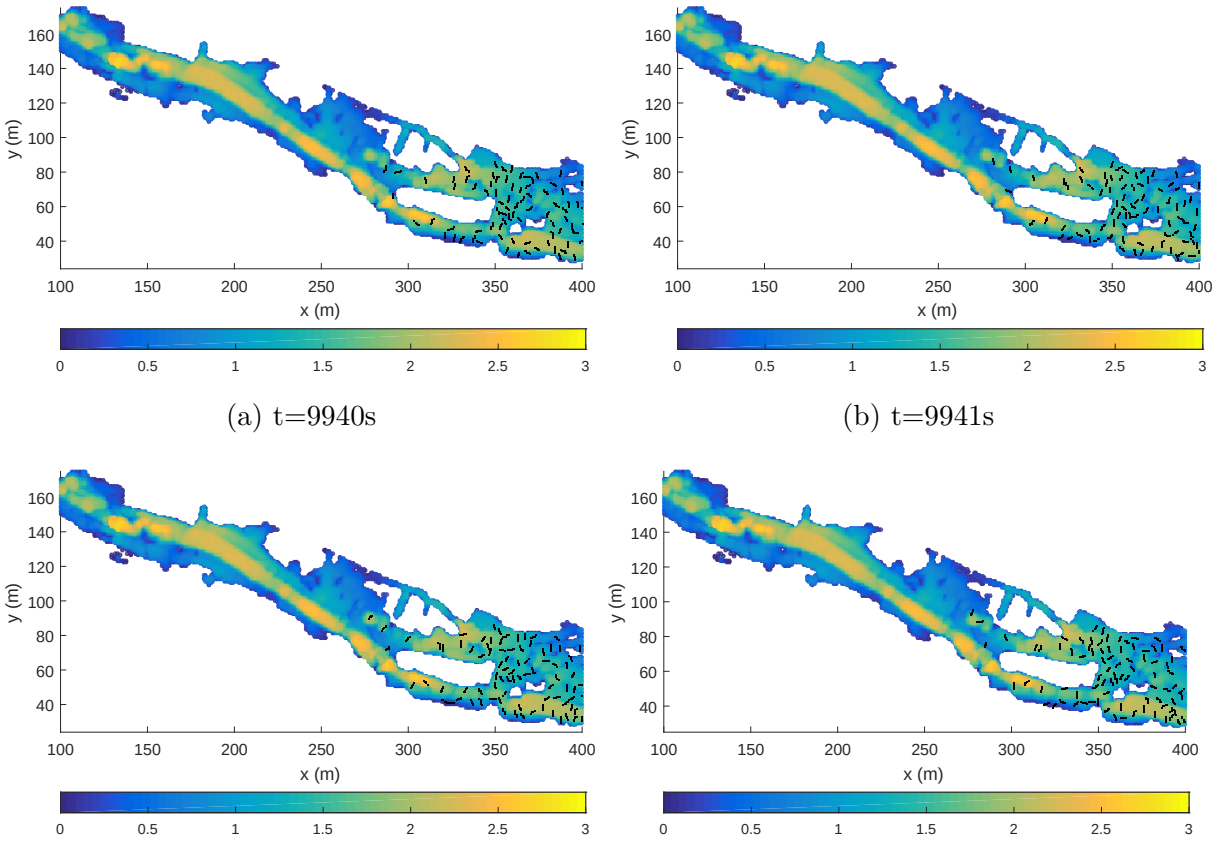

(a) t=9940s

(b) t=9941s

(c) t=9942s

(d) t=9943s

Figure 6.18: Simulated vehicles transported along the B3263 - numerical results for object position and water depth (m)

6.5.3 Discussion of results

The results for scenario 1 and 2 suggest that debris blockages at two bridges in Boscastle did not vastly alter the eventual flood extent. However there were significant local alterations to channel hydraulics upstream and downstream of the bridges. Furthermore significant regions of supercritical and transcritical flow were predicted as resulting from the blockages, particularly around the B3263 road bridge and riverside car park.

Application of the new floating debris modelling tool to scenario 3 has enabled the transport of 116 flooded vehicles to be predicted. The model results are largely consistent with photographic and observational evidence. The model captures initial flotation within the car park and vehicle transport pathways through the town. This information is valuable when assessing flood risk as it identifies areas that may be vulnerable to debris blockage or impact by debris. For example, the Riverside Hotel and surrounding buildings in Boscastle are predicted to suffer multiple impacts from floating vehicles. Model predictions for the time taken to transport vehicles downstream are significantly shorter than the observed timeline suggests. Particularly, the 25 minute lag between initial flotation and transport through Boscastle is not captured by the numerical scheme. Shu et al. (2011); Xia et al. (2010, 2011) have studied the incipient transport conditions of flooded vehicles and include friction with the channel bed as a critical factor in determining transport threshold. The numerical model presented here considers frictional contact in the horizontal direction but does not consider friction of objects against the channel bed. Unlike previous experimental applications, the vehicles transported during flooding in Boscastle were only partially submerged during incipient transport. Therefore friction with the channel bed is likely to have a significant affect on transport conditions for this application. Further development of the modelling tool to include friction between objects and the channel bed may enable the transport processes of partially submerged objects to be more accurately captured. The modelling tool is able to simulate detailed flood pathways of 116 vehicles transported through Boscastle. Model results therefore provide a greater understanding of the flood hazard in Boscastle than pure-water hydrodynamic modelling along.

During the simulation, none of the modelled vehicles become permanently entrapped at either of the two bridges. Instead vehicles transported in the main channel are washed straight through the bridge opening. Bridges are modelled in the computational domain through a digital terrain model. For zero initial blockage conditions the terrain is set as equal to the channel bottom. Therefore, where the bridge opening is assumed to be initially clear, the terrain data take no account of the bridge deck. Both bridges in the centre of Boscastle were masonry arch bridges with relatively low clearance, particularly

close to the abutments. Xia et al. (2016), performed experiments in a hydraulic flume to test vehicle entrapment at bridges. Their experimental results for vehicles at an arched bridge showed that entrapment occurs between the channel bed, bridge piers and bridge deck. Therefore in order to capture debris blockage, further model development is needed to represent the bridge deck. This could be achieved through the DEM part of the model. A multi-sphere object with equal dimensions to the bridge deck may be included within the simulation and its position fixed within the domain. This would enable realistic interactions between debris and the deck to be modelled, including blockage between the deck, abutments and the channel bed.

Due to the heavy computational cost of modelling 116 vehicles, steps have been taken to speed-up the computation. Vehicle shapes are here crudely approximated so that each modelled vehicle comprises three object-spheres. To further speed-up computation, vehicles are not included within the numerical model for the full duration of the simulated flood event. Instead vehicles have been initialised after 9900s of simulation. This adjustment is considered reasonable as eyewitness reports indicate that vehicles began to float at this time. A more physically based approach to initialising debris transport would be to consider incipient transport dynamics in more detail. Xia et al. (2011) developed an incipient transport equation for flooded vehicles that includes vehicle properties, fluid velocity and water depth as transport variables. Further development of the floating debris modelling tool to include an incipient transport equation would prevent vehicle motion until the transport threshold is reached. This method would consider more detailed forces and simulate more realistic incipient transport conditions.

Despite efforts to ease computational effort, modelling 116 flooded vehicles is computationally costly for the new floating debris modelling tool. The number of objects modelled within this application is considered to represent an upper limit for the quantity of debris that can be handled. To enable wider application of the floating debris modelling tool further development is needed to speed-up the computation. Possible approaches to speeding-up the computation are discussed briefly in Chapter 7. These are recommended for further work.

6.6 Conclusion

Flash flooding in Boscastle 2004 provides a valuable test case for investigating the effects of debris blockage and object transport during a flash flood event. The flood event was characteristically 'flashy' and complex channel hydraulics were further compounded by blockages at two bridges. The flooding of a riverside car park mobilised and transported

a total of 116 vehicles that further contributed to blockages. Excellent records of the event and a number of post event studies have afforded the necessary data for numerical modelling. The numerical results presented in this chapter have been used to investigate the role of debris blockages on channel hydraulics, and the transport dynamics of washed away vehicles during the Boscastle event. The blockage of two channel bridges is predicted to significantly alter localised channel hydraulics around the structure. Modelling flooded vehicle transport using a new floating debris modelling tool predicts the flood pathways of washed-away vehicles and their eventual locations. The results demonstrate that a new floating debris modelling tool developed in this work, is suitable for modelling flooded vehicle transport during a UK flash flood event. Limitations of the modelling tool include the higher computational time, which suffers as a result of the large quantity of vehicles modelled. To achieve a reduced computation time, further model development is required.

Wrack mark data

Wrack mark	Column identifier	Row identifier	Estimated elevation (m AOD)	Description
1	51	167	6.1	Gravel washed away and trash mark
2	67	165	6.33	Vegetation marked and flattened
3	111	141	8.01	Trash on road and flattened vegetation
4	141	129	8.28	Max level probably higher
5	183	121	9.64	Max level possibly higher
6	204	110	9.79	Levels on windows ties in with trash caught on trees
7	208	108	9.98	Max level possibly higher
8	213	100	11.18	
9	250	76	10.64	Mark possibly caused by surge
10	274	42	12.99	Trash mark
11	284	24	13.86	Mud caught on vegetation
12	84	201	8.25	Water spilled over wall
13	100	173	8.38	
14	95	192	8.48	Trash mark on road and side of road
15	148	153	9.34	Water level possibly lower
16	185	146	9.99	Trash caught on wall
17	252	129	10.84	Trash caught on wall
18	276	110	11.53	Max level may have been higher
19	296	99	11.35	Internal water level on window
20	310	80	12.58	Debris on wall
21	315	98	12.53	Damp line on wall
22	332	96	12.46	Debris caught on cable. Max level estimated
23	351	67	12.76	Trash on steps and railing
24	349	54	13.58	
25	322	81	13.38	Maximum level reached by resident
26	316	70	13.46	Maximum level reached by resident
27	371	82	13.16	Maximum level possibly higher
28	404	86	14.34	Level given by landlord as underside of window
29	456	79	15.05	Level marked by resident
30	471	99	16.27	Level indicated by friend of owner. Still water level

Table 6.1: Surveyed wrack mark data (Environment Agency, 2004; Kvočka et al., 2015)

Vehicle parameters			
Length	4.855m	No. of Spheres	3
Width	1.846m	Sphere diameter	0.75m
Height	1.512m	K_n	500 kN/m
Mass	$1830kg$	K_s	300 kN/m
Inertia	$3000kgm^2$	μ	0.295

Table 6.2: Physical and computational parameters of modelled BMW M5 vehicle estimated based on literature findings (Batista, 2006; Heydinger et al., 1999; Kostek and Aleksandrowicz, 2017; Shu et al., 2011; Xia et al., 2011)

Chapter 7

Conclusions and recommendations

This work presents a new approach to hydrodynamic flood modelling that incorporates floating debris as a dynamic flash flood process. The preceding chapters have presented the development of a new coupled floating debris modelling tool that predicts the transport dynamics of floating objects. The modelling tool applies the shock capturing capabilities of a finite volume Godunov-type hydrodynamic scheme coupled with the multi-sphere discrete element method. A balanced force coupling procedure predicts the transport dynamics of floating objects and simulates the backwater effects caused by debris blockage. This work is novel in that it is the first to apply hydrodynamic and hydrostatic force components that are derived according to the momentum principle for open channel flows. Additionally, the multi-sphere method for shape representation makes the tool extendable for theoretically any shape of debris. The new coupled debris modelling tool has been validated analytically and experimentally for 1D and 2D applications. Application of the new modelling tool to simulate a UK flash flood event demonstrates that it is computationally capable of real-world-scale application. In a wider civil engineering context, the modelling tool developed here provides valuable outputs for flood risk and flood hazard analysis; and structural and geotechnical design. Application of the new modelling tool is not limited to flood borne debris; the tool could also be applied to a range flood related natural hazards (eg. tsunami, storm surge and river ice transport). To improve modelling capability and better understand model limitations, further development and analysis is needed. Furthermore, data acquisition would enable wider model application as the new tool relies heavily on data availability.

7.1 Summary of results

The DEM modelling scheme used in this work has been developed specifically for hydraulic coupling. To validate the numerical scheme, the DEM have been verified against analytical results for three idealised test cases. The results presented in Chapter 3 demonstrate that the DEM accurately solves the governing equations for each example. Through visual validation there is little discernible difference between numerical and analytical results.

A floating debris modelling tool that predicts flow variables and debris transport in 1D has been developed in this work. The modelling tool has been validated against experimental results for scaled objects transported in a hydraulic flume. For most cases the 1D debris modelling tool makes good predictions of water depth and object position with respect to time. This has been validated visually and is also indicated by acceptable values of RMSE. However the experimental results also indicate that floating objects travelling in a uniform channel undergo significant rotation in some cases. Where significant rotation occurs, the new 1D debris modelling tool underestimates distance travelled by the object. It is also likely that approximation of the vertical fluid velocity profile contributes to a lag between predicted and observed object position.

The modelling tool has been developed and improved further in Chapter 5 to predict 2D flow and debris transport variables including object rotation. Experimental test cases, where multiple objects are transported by a dam break wave in the presence of a fixed domain obstacle, have been performed. Comparisons of numerical outputs against experimental results have enabled validation of the 2D modelling tool. In each case the model accurately predicts the arrival of a dam break wave and generally makes good predictions of water depth at gauged points. This has been validated visually and through a RMSE analysis. The position of floating objects has been validated visually against photographic evidence. The new modelling tool predicts the collective transport dynamics of a mass of wooden dowels well. It correctly predicts dowel transport as either sparsely configured, or 'clumped' together. Where objects interact with fixed obstacles the numerical model captures debris entrapment well. However, object velocity is slightly underestimated. This is probably due to hydrostatic assumptions made by the hydrodynamic scheme leading to underestimation of fluid surface velocity. The new modelling tool has also been validated against results presented by Albano et al. (2016). The tool captures object transport, entrapment and gauged water depth very well. This has been validated visually and statistically. The results presented here are comparable in accuracy with numerical results presented by Albano et al. (2016) but also achieve substantial computational gains (simulation time of < 10 minutes vs. >3 days).

The validated 2D debris modelling tool has been additionally applied to investigate

a flash flood event that occurred on 16th August 2004 in Boscastle, North Cornwall. During this event the flooding of a riverside car park transported a cargo of vehicles through the town. The Boscastle event has initially been modelled using a 2D finite volume Godunov-type hydrodynamic scheme to investigate the effect of bridge blockage on channel hydraulics. Model predictions of water depth and depth averaged velocity illustrate the backwater effects of bridge blockage. Predicted water depths at selected 'wrack mark' locations are consistent with surveyed data. Additionally the new floating debris modelling tool has been applied to investigate washed-away vehicles during the Boscastle event. The model predicts the transport of 116 flooded vehicles to a number of downstream locations. The predictions are consistent with photographic evidence. The results presented here would provide valuable information for flood hazard analysis and structural assessment of impacted bridges. These results demonstrate that the new debris modelling tool is both practical and valuable for real-world flash flood application.

7.2 Results in a civil engineering context

The focus in this work has been on developing, validating and applying a new coupled floating debris modelling tool. Where similar work is applicable to flume scale experiments, the modelling tool developed in this work has been shown to function at a river-reach scale. As a consequence the results presented in this work are valuable for understanding floating debris processes in real flash flood scenarios. Within a wider civil engineering context, results are relevant not just to flood risk analysis; but also to structural design and assessment; and to a range of other natural hazards.

7.2.1 Flood risk and hazard analysis

Hydraulic modelling provides a means of assessing flood risk under a range of input and boundary conditions. It is valuable for assessing a catchment's response to flood events and for assessing the impact of intervention features. The floating debris modelling tool presented in this work provides a means of identifying areas of a catchment that are particularly at risk from floating debris. This may be vulnerable structures at risk of blockage, or urban streets where vehicles may become mobilized. Furthermore the new modelling tool provides a means of testing the efficacy of blockage intervention features, for example 'log catchers'.

Log catchers are vertical, intermittently placed poles positioned across a river's width to entrap floating debris before they reach vulnerable downstream locations. 'Log catch-

ers' have been incorporated into wider flood alleviation schemes at Morpeth in Northumberland and Pickering in North Yorkshire where they are positioned upstream of bridges that may normally be susceptible to blockage. As these features are designed to build-up with debris, intermittent maintenance is required to clear out blockages. Despite their increased use, no studies exist into the effectiveness of such features and particularly no modelling of log catchers has been carried out. The new coupled debris modelling tool developed in this work is ideally suited to simulate the entrapment of floating debris at log catchers. Such a study could investigate how log catcher geometry affects entrapment probability, or to predict the frequency of maintenance required to maintain river conveyance.

More and more frequently, flood alleviation schemes are incorporating natural flood management (NFM) to complement hard engineering in order to attenuate flows, trap sediment and manage floating debris. Woody debris dams or leaky dams are a designed NFM feature intended to attenuate flood wave movement by reactivating the flood plain (SEPA, 2015). These features are usually constructed by anchoring a log perpendicular to flow. They then collect sediment and entrap further natural debris to create a dam across the channel. A series of these small scale dams incrementally force river flow into the flood plain and are therefore intended to increase the storage capacity of a catchment. The new coupled debris modelling tool developed in this work could be applied to investigate the effectiveness of leaky dams in trapping further floating debris and predict the hydraulic effect of their presence. Unlike other hydrodynamic modelling approaches, the dam could be modelled as a dynamic feature with changing geometry relative to time. Furthermore, with high flows there is a risk that anchored logs could be undermined and mobilised causing transport of the leaky dam downstream. The new debris modelling tool developed in this work could be applied to investigate the possible hazard posed by leaky dams in the event that they are transported downstream.

7.2.2 Structural design and assessment

In Chapter 6 the hydraulic consequences of debris blockages at two bridges in Boscastle has been demonstrated. The results show that when blocked, bridge afflux increases, resulting in upstream stage rise, and reduced downstream stage. Furthermore, results for vehicle transport include impact with bridges. Structural stability under flood and blockage conditions has been discussed briefly in Chapter 2, where it was mentioned that a load combination of debris impact and hydraulic forces can result in structural damage and even failure. The new debris modelling tool developed in this work can provide valuable information relevant to structural engineering, such as the dimensions

of debris blockages, pressure and velocity fields acting on a structure and the velocity of debris impact. Furthermore the same information would be valuable in geotechnical assessment of foundations and ground conditions after a flood event. Such information would normally be too dangerous to collect during a flood events and difficult to measure through physical experiments. Therefore the new debris modelling tool yields information that is not available through other means.

7.2.3 Natural hazards

The coupled debris modelling methodology, exhibited in this work, could also be applied to objects transported during other flood related natural hazards. The numerical methods used to predict flow variables have already been demonstrated as suitable for modelling tsunami and storm surge type flow regimes (Amouzgar et al., 2014; Qiang et al., 2016). During such events, floating objects including shipping cargo are transported inland and can cause catastrophic damage. The new floating debris modelling tool has been specifically developed to enable objects of any shape, size or material properties to be modelled through the multi-sphere method. The modelling tools developed and applied in this study therefore, could easily be used to investigate the transport of any floating object during coastal flooding and offshore applications. Likewise the coupled DEM approach is highly suited for modelling river ice transport as similar schemes have already demonstrated (Hopkins and Daly, 2003).

7.3 Recommendations for future work

7.3.1 Model development

The aim of this work has been to develop a new coupled modelling tool for predicting the transport dynamics of floating debris. Moreover, this work aimed to demonstrate the efficacy of a coupled hydrodynamic-discrete element modelling approach for use in computational hydraulics. Through the research presented in the preceding chapters, these aims have been achieved. Within the scope of this study, it was not intended to fully develop a floating debris modelling tool for widespread or commercial use. In order to progress the current research, and enable wider application of the modelling tool, further model development is required.

- Computation time

A key feature of the hydrodynamic modelling scheme is the use of parallel processing to accelerate computation for large scale flood simulations over complex bed topographies (Liang, 2010). However, the DEM developed in this work is not currently programmed for parallel processing. Therefore, within the coupled debris modelling tool, object transport algorithms act as a bottle neck and vastly reduce computational efficiency. Application of the new tool is limited by the need to achieve accurate results within reasonable computation time. A necessary further step, is therefore to develop the DEM for parallel processing across multiple GPUs. This would enable the simulation of large-scale complex domains with high quantities of floating debris without the constraints of unrealistic computation time. Further means of speeding computation have already been developed for DEM elsewhere. Within the DEM scheme, contact detection between spheres is the most computationally costly process and various procedures to accelerate this process exist. Inclusion of an accelerated contact detection algorithm within the DEM would further speed computation time and widen possible applications of the floating debris modelling tool.

- Vertical velocity profile

In a few of the validation cases presented in Chapters 4 and 5, numerical predictions slightly underestimate the translational velocity of transported debris. This has been discussed in greater detail in Chapter 4. The cause of this error is likely the 2D approximation of fluid velocity fields (explained in Chapter 3). Due to frictional effects of the channel bed, the surface velocity of open channel flow is usually higher than the depth averaged velocity. As fluid velocity influences the hydrodynamic force on a floating object, the object velocity is generally underestimated. The magnitude of this error is exaggerated for applications where water depth is large. This source of error requires further assessment. The inclusion of an additional term to account for increased surface velocity may be necessary for future application of the modelling tool.

- Complex shapes

As described in Chapter 3 the discrete element scheme developed in this work makes use of the multi-sphere method for shape representation. Theoretically this means that any object shape can be approximated to a high level of accuracy and therefore allows the model to be applied to floating objects of any shape. For the Boscastle flood application presented here, vehicles shapes have been vastly simplified so as to minimise computation

time. This has been considered a reasonable simplification considering the simulation duration, domain size and number of vehicles included. However the multi-sphere method provides a means of modelling much more realistic vehicle shapes and this could enable close-inspection investigation of vehicle transport dynamics. For example, the tool could be used to investigate incipient transport conditions of flooded vehicles or to model close-scale vehicle impact with structures. Furthermore the modelling tool could be applied to any objects shape or size to study floating debris from other urban sources.

- Sensitivity analysis

The floating debris modelling tool developed in this work has been validated for a number of experimental applications. However so far, no official parameter sensitivity analysis has been performed. There are a number of additional object dependent parameters used within the new coupled floating debris modelling tool that are not conventionally used in other hydrodynamic modelling techniques. For example contact and material variables (K_n, C_n, K_s, C_s, μ). In order to assess model robustness and identify the main sources of model sensitivity within these additional parameters, a thorough sensitivity analysis is required.

7.3.2 Data acquisition

- Debris origins

A necessary input variable for the new coupled floating debris flood modelling tool are the initial positions and material parameters for each floating object within an application. This limits possible applications of the modelling tool to flood events where sensible estimates for the origins and composition of floating debris can be easily made. The 2004 Boscastle event, presented in Chapter 6, is an example where debris composition and origins are easily obtained; objects consisting of flooded vehicles were transported from a riverside car park. More often debris origins are located high within the uplands of a catchment and enter the watercourse sporadically. Further investigation of the rate and composition of floating debris entering water courses is therefore required to enable reasonable estimation of object initial conditions. Furthermore, where objects enter a watercourse from outside of the computational domain, a means of predicting rate of entry is needed. A stochastic approach could be developed to predict the rate of debris entering a watercourse from outside of the domain.

- Image recognition

Flooding in Boscastle remains one of the best documented flash flood events in the UK. In part this is due to the prompt work of relevant agencies in collecting post event data and collating eyewitness accounts. However, collecting field evidence from flash flood events remains difficult due to the remote nature of affected catchments and short flood warning times. Post event data availability continues to hamper accurate modelling of flash flooding. Recent advances in image and shape recognition are promising, however and could improve post event data collection, particularly by automatically identifying flood extent and floating debris from photographic evidence. Researchers at Penn State University, USA (Sava et al., 2017) have demonstrated the ability of image recognition technology paired with machine learning to map flood extent from aerial imagery. The same technology could be used to identify floating debris in floodwaters and be used to automate initial debris positions within the new coupled modelling tool. Image recognition data of flood extent and debris position could also be used for model validation.

- Field observations

This study has focussed on validating the new debris modelling tools through application to experimental studies performed in a hydraulic flume. Such studies are valuable and enable tighter control of numerous variables. However flume studies are susceptible to scaling errors and do not fully recreate all of the physical processed observed during flash flooding (eg. complex bed topographies, variable roughness, and irregularities in debris shape and size). It is therefore recommended that field data be sought to enable further model validation. Field investigation would also contribute to floating debris research by improving understanding of the physics governing debris transport.

Bibliography

Abbaspour-Fard, M. (2004), 'Theoretical Validation of a Multi-sphere, Discrete Element Model Suitable for Biomaterials Handling Simulation', *Biosyst. Eng.* **88**(2), 153–161.

Abbaspour-Fard, M. H. (2000), Discrete element modelling of the dynamic behaviour of non-spherical particulate materials, PhD thesis, University of Newcaslte upon Tyne.

Abbe, T. and Montgomery, D. (1996), 'Large woody debris jams, channel hydraulics and habitat formation in large rivers', *Regul. Rivers Res. Manag.* **12**, 201–221.

Aboul Hosn, R., Sibille, L., Benahmed, N. and Chareyre, B. (2017), 'Discrete numerical modeling of loose soil with spherical particles and interparticle rolling friction', *Granul. Matter* **19**(1), 4.

Albaba, A., Lambert, S., Nicot, F. and Chareyre, B. (2015), 'Relation between microstructure and loading applied by a granular flow to a rigid wall using DEM modeling', *Granul. Matter* **17**(5), 603–616.

Albano, R., Sole, A., Mirauda, D. and Adamowski, J. (2016), 'Modelling large floating bodies in urban area flash-floods via a Smoothed Particle Hydrodynamics model', *J. Hydrol.* **541**, 344–358.

Alias, N. A., Liang, Q. and Kesserwani, G. (2011), 'A Godunov-type scheme for modelling 1D channel flow with varying width and topography', *Comput. Fluids* **46**(1), 88–93.

Amicarelli, A., Albano, R., Mirauda, D., Agate, G., Sole, A. and Guandalini, R. (2015), 'A Smoothed Particle Hydrodynamics model for 3D solid body transport in free surface flows', *Comput. Fluids* **116**, 205–228.

Amouzgar, R., Liang, Q. and Smith, L. (2014), 'A GPU-accelerated shallow flow model for tsunami simulations', *Proc. Inst. Civ. Eng. - Eng. Comput. Mech.* **167**(3), 117–125.

Archer, D. R. and Fowler, H. J. (2015), 'Characterising flash flood response to intense rainfall and impacts using historical information and gauged data in Britain', *J. Flood Risk Manag.* **11**(S1), 121–133.

Arrighi, C., Alcèrreca-Huerta, J., Oumeraci, H. and Castelli, F. (2015), 'Drag and lift contribution to the incipient motion of partly submerged flooded vehicles', *J. Fluids Struct.* **57**, 170–184.

Aureli, F., Dazzi, S., Maranzoni, A., Mignosa, P. and Vacondio, R. (2015), 'Experimental and numerical evaluation of the force due to the impact of a dam-break wave on a structure', *Adv. Water Resour.* **76**, 29–42.

Balevičius, R., Džiugys, A., Kačianauskas, R., Maknickas, A. and Vislavičius, K. (2006), 'Investigation of performance of programming approaches and languages used for numerical simulation of granular material by the discrete element method', *Comput. Phys. Commun.* **175**(6), 404–415.

Batista, M. (2006), On the Mutual Coefficient of Restitution in Two Car Collinear Collisions, Technical report.

Benn, J. (2013), 'Railway bridge failure during flooding in the UK and Ireland', *Proc. Inst. Civ. Eng. - Forensic Eng.* **166**(4), 163–170.

Benn, J. R., Mantz, P., Lamb, R., Riddell, J. and Nalluri, C. (2004), Defra/Environment Agency Flood and Coastal Defence R&D Programme - afflux at bridges and culverts: review of current knowledge and practice, Technical report.

Biran, A. B. (2003), *Ship Hydrostatics and Stability*, Oxford : Butterworth-Heinemann.

Bocchiola, D., Catalano, F., Menduni, G. and Passoni, G. (2002), 'An analytical - numerical approach to the hydraulics of floating debris in river channels', *J. Hydrol.* **269**(1-2), 65–78.

Bocchiola, D., Rulli, M. C. and Rosso, R. (2008), 'A flume experiment on the formation of wood jams in rivers', *Water Resour. Res.* **44**(2).

Bocchiola, D., Rulli, M. and Rosso, R. (2006), 'Transport of large woody debris in the presence of obstacles', *Geomorphology* **76**(1-2), 166–178.

Braudrick, C. A. and Grant, G. E. (2000), 'When do logs move in rivers?', *Water Resour. Res.* **36**(2), 571–583.

Braudrick, C. A. and Grant, G. E. (2001), 'Transport and deposition of large woody debris in streams: a flume experiment', *Geomorphology* **41**(4), 263–283.

Braudrick, C. A., Grant, G. E., Ishikawa, Y. and Ikeda, H. (1997), 'Dynamics of wood transport in streams: a flume experiment', *Earth Surf. Process. landforms* **22**(22), 669–683.

Brooks, A. P., Abbe, T., Cohen, T. J. and Rutherford, I. D. (2006), *Design Guidelines for the Reintroduction of Wood into Australian Streams*, Land and Water Australia.

Brunner, G. W. (2016), HEC-RAS River Analysis System User's Manual, Technical report, US Army Corps of Engineers.

CCC (2017), Committee on Climate Change - UK Climate Change Risk Assessment 2017 Synthesis Report - July 2016, Technical report.

Chadwick, A., Morfett, J. and Borthwick, M. (2013), *Hydraulics in Civil and Environmental Engineering*, 5th edn, Taylor and Francis Group, London.

Chang, F. F. M. and Shen, H. W. (1979), Debris problems in the river environment, Technical report, Washington :.

Chareyre, B., Cortis, A., Catalano, E. and Barthélemy, E. (2012), 'Pore-Scale Modeling of Viscous Flow and Induced Forces in Dense Sphere Packings', *Transp. Porous Media* **92**(2), 473–493.

Chen, F., Drumm, E. C. and Guiochon, G. (2007), 'Prediction/Verification of Particle Motion in One Dimension with the Discrete-Element Method', *Int. J. Geomech.* **7**(5), 344–352.

CIRIA (2017), Manual on scour at bridges and other hydraulic structures, second edition, Technical report, CIRIA.

Comiti, F., Lucía, A. and Rickenmann, D. (2016), 'Large wood recruitment and transport during large floods: A review', *Geomorphology* **269**, 23–39.

Comiti, F., Mao, L., Preciso, E., Picco, L., Marchi, L. and Borga, M. (2008), Large wood and flash floods: evidence from the 2007 event in the Davča basin (Slovenia), *in* 'Monit. Simulation, Prev. Remediat. Dense Debris Flows II', Vol. I of *WIT Transactions on Engineering Sciences*, WIT Press, Southampton, UK, pp. 173–182.

Cundall, P. A. and Strack, O. D. L. (1979), 'A discrete numerical model for granular assemblies', *Geotechnique* **29**(1), 47–65.

Daly, S. F. and Hopkins, M. A. (1998), Simulation of river ice jam formation, *in* 'Ice Surf. Waters, Proc. 14th Int. Symp. Ice', H.H. Shen, Ed., New York.

Daly, S. F. and Hopkins, M. A. (1999), Modelling River Ice using Discrete Element Particle Simulation, *in* '10th Int. Conf. Cold Reg. Eng. Am. Soc. Civ. Eng.', Lincoln, NH.

Daly, S. F. and Hopkins, M. A. (2001), Estimating Forces on an Ice Control Structure Using DEM, *in* '11th Work. Hydraul. Ice Cover. Rivers', Committee on River Ice Processes and the Environment, Canadian Geophysical Union-Hydrology Section, Ottawa.

Daniels, M. D. and Rhoads, B. L. (2004), Spatial pattern of turbulence kinetic energy and shear stress in a meander bend with large woody debris, American Geophysical Union, pp. 87–97.

De Cicco, P., Enio, P. and Solari, L. (2015), Flume experiments on bridge clogging by woody debris: the effect of shape of piers, *in* '36th IAHR World Congr.', Delft - The Hague, The Netherlands.

Diehl, T. H. (1997), Potential Drift Accumulation at Bridges, Technical report.

DMRB (1994), Volume 1 Section 3 Part 6 - BA 59/94 - The Design of highway bridges for hydraulic action, Technical report.

Dobbie, C. H. and Wolf, P. O. (1953), 'The Lynmouth flood of August 1952', *Proc. Inst. Civ. Eng.* **2**(6), 522–546.

Duriez, J. and Wan, R. (2017), 'Subtleties in discrete-element modelling of wet granular soils', *Géotechnique* **67**(4), 365–370.

Dutta, D., Herath, S. and Musiake, K. (2003), 'A mathematical model for flood loss estimation', *J. Hydrol.* **277**(1-2), 24–49.

Ebrahimi, M., Kripakaran, P., Djordjevic, S., Tabor, G., Kahraman, R., Prodanović, D. and Arthur, S. (2016), Hydrodynamic Effects of Debris Blockage and Scour on Masonry Bridges: Towards Experimental Modelling, *in* 'Scour Eros. Proc. 8th Int. Conf. Scour Eros. (Oxford, UK, 12-15 Sept. 2016)', CRC Press.

Environment Agency (2004), Living with the risk: The floods in Boscastle and North Cornwall 16 August 2004, Technical report, Environment Agency.

Environment Agency (2010), 'Fluvial Design Guide - Chapter 7'.

Faulkner, H. and Copp, G. H. (2001), 'A model for accurate drift estimation in streams', *Freshw. Biol.* **46**(6), 723–733.

Favier, L., Daudon, D. and Donzé, F.-V. (2013), 'Rigid obstacle impacted by a supercritical cohesive granular flow using a 3D discrete element model', *Cold Reg. Sci. Technol.* **85**, 232–241.

Fenn, C., Bettess, R., Golding, B., Farquharson, F. and Wood, T. (2005), The Boscastle flood of 16 August 2004: Characteristics, causes and consequences, Technical report, York.

Fleissner, F., Gaugele, T. and Eberhard, P. (2007), 'Applications of the discrete element method in mechanical engineering', *Multibody Syst. Dyn.* **18**(1), 81–94.

Gaume, E., Bain, V., Bernardara, P., Newinger, O., Barbuc, M. and Bateman, A. (2009), 'A compilation of data on European flash floods', *J. Hydrol.* **367**(1-2), 70–78.

Gifford, K. A., Horton, J. L., Wareing, T. A., Failla, G. and Mourtada, F. (2006), 'Comparison of a finite-element multigroup discrete-ordinates code with Monte Carlo for radiotherapy calculations', *Phys. Med. Biol.* **51**(9), 2253–2265.

Gippel, C. J. (1995), 'Environmental Hydraulics of Large Woody Debris in Streams and Rivers', *J. Environ. Eng.* **121**(5), 388–395.

Goseberg, N., Stolle, J., Nistor, I. and Shibayama, T. (2016), 'Experimental analysis of debris motion due to the obstruction from fixed obstacles in tsunami-like flow conditions', *Coast. Eng.* **118**, 35–49.

Gschnitzer, T., Gems, B., Mazzorana, B. and Aufleger, M. (2017), 'Towards a robust assessment of bridge clogging processes in flood risk management', *Geomorphology* **279**, 128–140.

Guan, M. and Liang, Q. (2017), 'A two-dimensional hydro-morphological model for river hydraulics and morphology with vegetation', *Environ. Model. Softw.* **88**, 10–21.

Haehnel, R. B. and Daly, S. F. (2002), Maximum Impact Force of Woody Debris on Floodplain Structures, Technical report, US Army Corps of Engineers - Cold Regions Research and Engineering Laboratory.

Hancock, B., Wassgren, C., Curtis, J., Kodam, M. and Bharadwaj, R. (2009), 'Force model considerations for glued-sphere discrete element method simulations', *Chem. Eng. Sci.* **64**(15), 3466–3475.

Harmon, M., Franklin, J., Swanson, F., Sollins, P., Gregory, S., Lattin, J., Anderson, N., Cline, S., Aumen, N., Sedell, J., Lienkaemper, G., Cromack, K. and Cummins, K. (2004), 'Ecology of Coarse Woody Debris in Temperate Ecosystems', *Adv. Ecol. Res.* **34**, 59–234.

Harthong, B., Jérier, J.-F., Richefeu, V., Chareyre, B., Dorémus, P., Imbault, D. and Donzé, F.-V. (2012), 'Contact impingement in packings of elasticplastic spheres, application to powder compaction', *Int. J. Mech. Sci.* **61**(1), 32–43.

Hartlieb, A. (2017), 'Decisive Parameters for Backwater Effects Caused by Floating Debris Jams', *Open J. Fluid Dyn.* **07**(04), 475–484.

Heydinger, G., Bixel, R., Garrott, W., Pyne, M., Howe, G. and Guenther, D. (1999), Measured vehicle inertial parameters - NHTSA's Data through November 1998, Technical report, Society of Automotive Engineers.

Hopkins, M. A. and Daly, S. F. (1999), Discrete Element Modeling of River Ice at Navigation Structures, *in* '10th Work. River Ice, Can. Comm. River Ice Process. Environ.', Winnipeg, Manitoba, CA, pp. 59–69.

Hopkins, M. A., Daly, S. F. and Lever, J. H. (1996), Three Dimensional Simulation of River Ice Jams, *in* 'Am. Soc. Civ. Eng. 8th Int. Conf. Cold Reg. Eng.', Fairbanks, AK.

Hopkins, M. A., Daly, S. F., Shearer, D. R. and Townsend, W. (2002), Simulation of river ice in a bridge design for Buckland, Alaska, *in* 'Ice Environ. Proc. 16th IAHR Int. Symp. Ice Dunedin', International Association of Hydraulic Engineering and Research, New Zealand, pp. 2–6.

Hopkins, M. A. and Tuhkuri, J. (1999), 'Compression of floating ice fields', *J. Geophys. Res. Ocean.* **104**(C7), 15815–15825.

Hopkins, M. A. and Tuthill, A. M. (2002), 'Ice Boom Simulations and Experiments', *J. Cold Reg. Eng.* **16**(3), 138–155.

Hopkins, M. and Daly, S. F. (2003), Recent Advances in Discrete Element Modeling of River Ice, *in* 'CGU HS Comm. River Ice Process. Environ. 12th Work. Hydraul. Ice Cover. Rivers'.

Horritt, M., Bates, P., Fewtrell, T., Mason, D., Wilson, M., Horritt, M. S., Bates, P. D., Fewtrell, T. J., Mason, D. C. and Wilson, M. D. (2010), 'Modelling the hydraulics of the Carlisle 2005 flood event', *Proc. Inst. Civ. Eng. Water Manag.* (WM6), 273–281.

HR Wallingford (2005), Flooding in Boscastle and North Cornwall, August 2004, Technical report.

Hulet, K. M., Smith, C. C. and Gilbert, M. (2006), 'Load-carrying capacity of flooded masonry arch bridges', *Proc. Inst. Civ. Eng. Bridg. Eng.* (BE3), 97–103.

Itasca (1998), PFC2D 2.00 Particle Flow Code in Two Dimensions, Technical report, Itasca consulting group, Minneapolis, Minnesota.

Iverson, R. M. (1997), 'The physics of debris flows', *Rev. Geophys* **35**(3), 245–296.

Jerier, J., Hathong, B., Richefeu, V., Chareyre, B., Imbault, D., Donze, F. V. and Doremus, P. (2011), 'Study of cold powder compaction by using the discrete element method', *Powder Technol.* **208**(2), 537–541.

Jian, W., Liang, D., Shao, S., Chen, R. and Yang, K. (2016), 'Smoothed Particle Hydrodynamics Simulations of Dam-Break Flows Around Movable Structures', *Int. J. Offshore Polar Eng.* **26**(1), 33–40.

Kelman, I. and Spence, R. (2004), 'An overview of flood actions on buildings', *Eng. Geol.* **73**(3-4), 297–309.

Kostek, R. and Aleksandrowicz, P. (2017), Simulation of car collision with an impact block, *in* 'IOP Conf. Ser. Mater. Sci. Eng. 252'.

Kvočka, D., Falconer, R. A. and Bray, M. (2015), 'Appropriate model use for predicting elevations and inundation extent for extreme flood events', *Nat. Hazards* **79**(3), 1791–1808.

Lhomme, J., Gutierrez-Andres, J., Weisgerber, A., Davison, M., Mulet-Marti, J., Cooper, A. and Gouldby, B. (2010), 'Testing a new two-dimensional flood modelling system: analytical tests and application to a flood event', *J. Flood Risk Manag.* **3**(1), 33–51.

Li, Q., Rudolph, V., Wang, F., Kajikawa, S.-I. and Horio, M. (2001), 'Axial porosity distribution in a packed bed of deformable particles: A numerical study based on DEM', *Handb. Powder Technol.* **10**, 127–134.

Liang et al., Q. (2016), 'Hydrodynamic modelling of flow impact on structures under extreme flow conditions', *J. Hydrodyn. Ser. B* **28**(2), 267–274.

Liang, Q. (2010), 'Flood Simulation Using a Well-Balanced Shallow Flow Model', *J. Hydraul. Eng.* **136**(9), 669–675.

Liang, Q. and Borthwick, A. G. (2009), 'Adaptive quadtree simulation of shallow flows with wetdry fronts over complex topography', *Comput. Fluids* **38**(2), 221–234.

Liang, Q., Du, G., Hall, J. W. and Borthwick, A. G. (2008), 'Flood Inundation Modeling with an Adaptive Quadtree Grid Shallow Water Equation Solver', *J. Hydraul. Eng.* **134**(11), 1603–1610.

Liang, Q. and Marche, F. (2009), 'Numerical resolution of well-balanced shallow water equations with complex source terms', *Adv. Water Resour.* **32**(6), 873–884.

Liang, Q. and Smith, L. S. (2015), 'A High-Performance Integrated Hydrodynamic Modelling System for Urban Flood Simulations', *J. Hydroinformatics* **17**(4), 518–533.

Liang, Q., Xia, X. and Hou, J. (2016), 'Catchment-scale high-resolution flash flood simulation using the GPU-based technology', *Procedia Eng.* **154**(154), 975–981.

Lin, X. and Ng, T.-T. (1997), 'A three-dimensional discrete element model using arrays of ellipsoids', *Géotechnique* **47**(2), 319–329.

Liu, M. B. and Liu, G. R. (2010), 'Smoothed Particle Hydrodynamics (SPH): an Overview and Recent Developments', *Arch. Comput. Methods Eng.* **17**(1), 25–76.

Lu, M. and McDowell, G. R. (2006), 'The importance of modelling ballast particle shape in the discrete element method', *Granul. Matter* **9**(1-2), 69–80.

Lyn, D. A., Cooper, T. J., Condon, C. A. and Gan, L. (2007), 'Factors in Debris Accumulation at Bridge Piers', *FWHA/IN/JTRP-2006/36* .

Lyn, D. A., Cooper, T., Yi, Y.-K., Sinha, R. and Rao, A. R. (2003), Debris Accumulation at Bridge Crossings: Laboratory and Field Studies, Technical report.

Ma, Z., Li, Y. and Xu, L. (2015), 'Discrete-element method simulation of agricultural particles' motion in variable-amplitude screen box', *Comput. Electron. Agric.* **118**, 92–99.

MacVicar, B., Piegay, H., Henderson, A., Comiti, F., Oberlin, C. and Pecorari, E. (2009), 'Quantifying the temporal dynamics of wood in large rivers: field trials of wood surveying, dating, tracking, and monitoring techniques', *Earth Surf. Process. Landforms* **34**(15), 2031–2046.

Malavasi, S. and Guadagnini, A. (2007), 'Interactions between a rectangular cylinder and a free-surface flow', *J. Fluids Struct.* **23**, 1137–1148.

Manners, R. B., Doyle, M. W. and Small, M. J. (2007), 'Structure and hydraulics of natural woody debris jams', *Water Resour. Res.* **43**(6).

Marchi, L., Borga, M., Preciso, E. and Gaume, E. (2010), 'Characterisation of selected extreme flash floods in Europe and implications for flood risk management', *J. Hydrol.* **394**(1-2), 118–133.

Markauskas, D., Kačianauskas, R., Džiugys, A., Navakas, ·. R. and Navakas, R. (2010), 'Investigation of adequacy of multi-sphere approximation of elliptical particles for DEM simulations', *Granul. Matter* **12**, 107–123.

Martínez-Martínez, L. H., Delgado-Hernández, D. J., De-León-Escobedo, D., Flores-Gomora, J. and Arteaga-Arcos, J. C. (2017), 'Woody debris trapping phenomena evaluation in bridge piers: A Bayesian perspective', *Reliab. Eng. Syst. Saf.* **161**, 38–52.

Maurin, R., Chauchat, J. and Frey, P. (2016), 'Dense granular flow rheology in turbulent bedload transport', *J. Fluid Mech.* **804**, 490–512.

Melville, B. W. and Dongol, D. M. (1992), 'Bridge Pier Scour with Debris Accumulation', *J. Hydraul. Eng.* **118**(9), 1306–1310.

Montgomery, D. R., Collins, B. D., Buffington, J. M. and Abbe, T. B. (2003), 'Geomorphic Effects of Wood in Rivers', *Am. Fish. Soc. Symp.* .

Murphy, M. L. and Koski, K. V. (1989), 'Input and Depletion of Woody Debris in Alaska Streams and Implications for Streamside Management', *North Am. J. Fish. Manag.* **9**(4), 427–436.

Nistor, I., Palermo, D., Cornett, A. and Al-Faesly, T. (2011), 'Experimental and numerical modeling of tsunami loading on structures', *Coast. Eng. Proc.* **1**(32), 2.

O'Sullivan, C. and Bray, J. D. (2003), 'Selecting a suitable time step for discrete element simulations that use the central difference time integration scheme', *Eng. Comput.* **21**(2/3/4), 278 – 303.

Parola, A. C., Apelt, C. J. and Jempson, M. A. (2000), Debris Forces on Highway Bridges, Technical report, National Cooperative Highway Research Program.

Perth and Kinross Council, Scottish Environment Protection Agency and Scottish Natural Heritage (2015), Joint Agency Report on the Flooding in Alyth of 17 July 2015, Technical report.

Peters, B. and Dziugys, A. (2002), 'Numerical simulation of the motion of granular material using object-oriented techniques', *Comput. Methods Appl. Mech. Engrg.* **191**, 1983 –2007.

Piche, S., Nistor, I. and Murty, T. (2014), 'Numerical modelling of debris impacts using the SPH method', *Coast. Eng. Proc.* **1**(34), 19.

Plimpton, S. (1995), 'Fast Parallel Algorithms for Short - Range Molecular Dynamics', *J. Comput. Phys.* **117**(1), 1–19.

Qiang, J., Liang, Q., Wang, G. and Zheng, J. (2016), Testing a Shock-Capturing Hydrodynamic Model for Storm Surge Simulation, *in* 'Proc. Twenty-sixth Int. Ocean Polar Eng. Conf.', Rhodes.

Ravazzolo, D., Mao, L., Picco, L. and Lenzi, M. (2015), 'Tracking log displacement during floods in the Tagliamento River using RFID and GPS tracker devices', *Geomorphology* **228**, 226–233.

Ren, B., Jin, Z., Gao, R., Wang, Y.-x. and Xu, Z.-l. (2014), 'SPH-DEM Modeling of the Hydraulic Stability of 2D Blocks on a Slope', *J. Waterw. Port, Coastal, Ocean Eng.* **140**(6), 04014022.

Rigby, E. H., Boyd, M. J., Roso, S., Silveri, P. and Davis, A. (2002), Causes and Effects of Culvert Blockage during Large Storms, *in* 'Glob. Solut. Urban Drain.', American Society of Civil Engineers, Reston, VA, pp. 1–16.

Robb, D. M., Gaskin, S. J. and Marongiu, J.-C. (2016), 'SPH-DEM model for free-surface flows containing solids applied to river ice jams', *J. Hydraul. Res.* **54**(1), 27–40.

Roca, M. and Davison, M. (2010), 'Two dimensional model analysis of flash- flood processes : application to the Boscastle event', *J. Flood Risk Manag.* **3**, 63 – 71.

Roso, S., Boyd, M., Rigby, T. and Van Drie Forbes, R. (2004), 'Prediction of increased flooding in urban catchments due to debris blockage and flow diversions'.

Rowe, D. (2004), *Boscastle 16th August 2004 - the day of the flood*, Truran, Penryn.

Ruiz-Villanueva, V. and al., E. (2014*a*), 'Large Wood in Rivers and its Influence on Flood Hazard', *Cuad. Investig. Geogr.* **40**(1), 229–246.

Ruiz-Villanueva, V. and al., E. (2014*b*), 'Two-dimensional modelling of large wood transport during flash floods', *Earth Surf. Process. Landforms* **39**(4), 438–449.

Ruiz-Villanueva, V. and al., E. (2014*c*), 'Two-dimensional numerical modeling of wood transport', *J. Hydroinformatics* **16**(5), 1077.

Samuels, P. G. (2004), Defra/Environment Agency Flood and Coastal Defence R&D Programme: Afflux at bridges and culverts, Technical report, Environment Agency.

Sava, E., Clemente-Harding, L. and Cervone, G. (2017), 'Supervised classification of civil air patrol (CAP)', *Nat. Hazards* **86**(2), 535–556.

Schmocker, L. and Hager, W. H. (2011), 'Probability of Drift Blockage at Bridge Decks', *J. Hydraul. Eng.* **137**(4), 470–479.

SEPA (2015), Natural Flood Management Handbook, Technical report.

Shu, C., Xia, J., Falconer, R. A. and Lin, B. (2011), 'Incipient velocity for partially submerged vehicles in floodwaters', *J. Hydraul. Res.* **49**(6), 709–717.

Simons, F., Busse, T., Hou, J., Özgen, I. and Hinkelmann, R. (2014), 'A model for overland flow and associated processes within the Hydroinformatics Modelling System', *J. Hydroinformatics* **16**(2), 375.

Šmilauer, V. and al., E. (2015), Yade Documentation 2nd ed., Technical report, The Yade Project.

Smith, L. S., Liang, Q. and Quinn, P. F. (2014), 'Towards a hydrodynamic modelling framework appropriate for applications in urban flood assessment and mitigation using heterogeneous computing', *Urban Water J.* **12**(1), 67–78.

Starkey, E., Parkin, G., Birkinshaw, S., Large, A., Quinn, P. and Gibson, C. (2017), 'Demonstrating the value of community-based (citizen science') observations for catchment modelling and characterisation', *J. Hydrol.* **548**, 801–817.

Stockstill, R. L., Daly, S. F. and Hopkins, M. A. (2009), 'Modeling Floating Objects at River Structures', *J. Hydraul. Eng.* **135**(5), 403–414.

Stockstill, R. L., Hite, J. E. and Park, H. E. (2005), 'Hydraulic design of upper approach walls to navigation locks', *Int. Navidation Assoc.* **118**, 17–25.

Thompson, W. T. (1966), *Vibration theory and applications*, 6th edn, Allen & Unwin, London.

Ting, J. M., Khwaja, M., Meachum, L. R. and Rowell, J. D. (1993), 'An ellipse-based discrete element model for granular materials', *Int. J. Numer. Anal. Methods Geomech.* **17**(9), 603–623.

Toro, E. F. (2001), *Shock-capturing methods for free-surface shallow flows*, John Wiley.

Toro, E. F. (2009), The HLL and HLLC Riemann Solvers, *in* 'Riemann Solvers Numer. Methods Fluid Dyn.', Springer Berlin Heidelberg, Berlin, Heidelberg, pp. 315–344.

Toro, E. F., Spruce, M. and Speares, W. (1994), 'Restoration of the contact surface in the Harten-Lax-van Leer Riemann solver', *Shock Waves* **4**, 25–34.

Tran, V., Meguid, M. and Chouinard, L. (2013), 'A finite - discrete element framework for the 3D modeling of geogrid - soil interaction under pullout loading conditions', *Geotext. Geomembranes* **37**, 1–9.

Transportation Association of Canada (2004), *Guide to bridge hydraulics.*, Thomas Telford.

Tsuji, Y., Tanaka, T. and Ishida, T. (1992), 'Lagrangian numerical simulation of plug flow of cohesionless particle in a horizontal pipe', *Powder Technol.* **71**, 239–250.

Tyne Rivers Trust (2015), Haltwhistle Burn - a comprehensive catchment approach to headwater runoff and pollution, Technical report, Tyne Rivers Trust, Corbridge.

Wallerstein, N., Arthur, S. and Blanc, J. (2013), Culvert design & operation guide supplementary technical note on understanding blockage risks, Technical report, Ciria, London.

Wang, Y., Kesserwani, G. and Hall, J. W. (2011), 'A 2D shallow flow model for practical dam-break simulations', *J. Hydraul. Res.* pp. 1814–2079.

Weller, R. and Zachmann, G. (2009), A Unified Approach for Physically-Based Simulations and Haptic Rendering, *in* 'Sandbox 2009 ACM SIGGRAPH Video Game Proc.', ACM Press, New Orleans.

Wu, J.-s., Zhang, H., Yang, R., Dalyrymple, R. and Herault, A. (2013), 'Numerical modeling of dam-break flood through intricate city layouts including underground spaces using GPU-based SPH method', *J. Hydrodyn. Ser. B* **25**(6), 818–828.

Xia, J., Falconer, R. A., Lin, B. and Wang, G. (2010), 'Numerical assessment of people and vehicle safety in flash floods', (i), 1–34.
URL: *http://orca.cf.ac.uk/38367/*

Xia, J., Teo, F., Falconer, R. A., Chen, Q. and Deng, S. (2016), 'Hydrodynamic experiments on the impacts of vehicle blockages at bridges', *J. Flood Risk Manag.* **11**(S1), 395 – 402.

Xia, J., Teo, F. Y., Teo, Y., Lin, B. and Falconer, R. A. (2011), 'Formula of incipient velocity for flooded vehicles', *Nat Hazards* **58**, 1–14.

Zhang, D. and Whiten, W. J. (1996), 'The calculation of contact forces between particles using spring and damping models', *Powder Technol.* **88**(1), 59–64.